12th Annual
Alberta Biomedical Engineering Conference
Program and Proceedings

Alberta BME

October 21st – 23rd, 2011
The Banff Centre
Banff, Alberta

University of Calgary

University of Lethbridge

University of Alberta

We gratefully acknowledge the support of our sponsors for making this conference a success

TENET
MEDICAL ENGINEERING
Advanced Adaptable Adjustable

Osteo-Metabolix Pharmaceuticals Inc.
Your Micro-CT Specialists ...
www.osteometabolix.com

NSERC CRSNG

NSERC CREATE Training Program for Biomedical Engineers for the 21st Century

John Simon & Associates Ltd.
Quality Assurance and Regulatory Affairs Consulting

BOSE

RSM Institute for Reconstructive Sciences in Medicine

SOCIÉTÉ CANADIENNE DE BIOMÉCANIQUE
CANADIAN SOCIETY FOR BIOMECHANICS

Altair

University of Alberta — Quaecumque Vera

Engineering U of A

University of Lethbridge — Fiat Lux

SCHULICH School of Engineering — University of Calgary

Schulich Student Activities Fund

University of Calgary

BME Graduate Program

SCHULICH School of Engineering — University of Calgary

CBRE

Centre for Bioengineering Research and Education


FACULTY OF
MEDICINE
UNIVERSITY OF
CALGARY


UNIVERSITY OF
CALGARY
KINESIOLOGY

12th Alberta Biomedical Engineering Conference - Banff 2011

UNIVERSITY OF ALBERTA

UNIVERSITY OF CALGARY

University of Lethbridge

October 21 – 23, 2011
The Banff Centre
Banff, AB

PROGRAM COMMITTEE

CONFERENCE ORGANIZERS

Co-Chairs	**Michael S. Kallos, University of Calgary** Nigel Shrive, University of Calgary **Samer Adeeb, University of Alberta** Marwan El-Rich, University of Alberta **Albert Cross, University of Lethbridge** Jon Doan, University of Lethbridge Larry Unsworth, Undergraduate Students Chair, University of Alberta
Student Co-Chairs	Swathi Damaraju, University of Calgary Garrett Melenka, University of Alberta

ABSTRACT REVIEWERS

Jason Carey, University of Alberta - Technical Committee Lead
Michael S. Kallos, University of Calgary - Technical Committee Lead
Kajsa Duke, University of Alberta
Marwan El-Rich, University of Alberta

Nigel Shrive, University of Calgary
Alison King, University of Calgary
Elise Fear, University of Calgary
Steve Boyd, University of Calgary
Albert Cross, University of Lethbridge
Jon Doan, University of Lethbridge

POSTER JUDGES

University of Alberta	Doug Hill	Martin Ferguson-Pell
	Kajsa Duke	Marwan El-Rich
University of Calgary	Richard Frayne	Leping Li
	Tannin Schmidt	Kristina Rinker
University of Lethbridge	Jon Doan	Sorina Truica

PODIUM JUDGES

University of Alberta	Vivian Mushahwar
University of Calgary	Jeff Dunn
Wright University	Thomas N. Hangartner

STUDENT VOLUNTEERS

University of Alberta	Garrett Melenka	Organizing Great Challenge, volunteer at conference (co-chair for podium sessions),
	Farhana Begum	Volunteer at conference (co-chair for podium sessions)
	Jonathon Schofield	Fundraising, volunteer at conference (co-chair for podium sessions)
	Kamrul Islam	Volunteer at conference (co-chair for podium sessions)
	Liping Qi	Volunteer at conference (co-chair for podium sessions)
	Jiajie Wu	Volunteer at conference (co-chair for podium sessions)
	Amin Komeili	Volunteer at conference
	Charlie Hsue	Fundraising
University of Calgary	Emily Bishop	Great Challenge, co-chair for podium sessions, coiling of programs, & general volunteer
	Quinn Thompson	Co-chair for podium sessions, coiling of programs
	Alireza Sojoudi	Putting electronic programs on USB keys

Taryn Ludwig	Co-chair for podium sessions, coiling of programs
Kiran Dwarkan	Coiling of programs
Saleem Abubacker	Co-chair for podium sessions, coiling of programs
Alyssa Randall	Co-chair for podium sessions
Swathi Damaraju	Great Challenge, co-chair for podium sessions, coiling of programs, & general volunteer
Terri Semler	Co-chair for podium sessions
Kogan Lee	Social night organizer
Krishna Panchalingam	Fundraising

SPECIAL STAR

University of Calgary	Lisa Mayer	Honorable Mention: Lorri Shaw

PROGRAMME

Podium Sessions are in the Max Bell Auditorium.
Poster Sessions are in the Max Bell 251 and 253.

FRIDAY

4:00 - 8:30 pm	**REGISTRATION and CHECK-IN – Professional Development Center Front Desk / Lounge**
7:30 pm	**Opening Reception – Kinnear Centre KC 103**
	Welcome: Dr. Michael Kallos & Dr. Samer Adeeb Kinnear Centre KC 103

SATURDAY

7:00 – 8:00 am	**BREAKFAST – Vistas Dining Room**
8:00 – 8:05 am	**Welcoming Remarks – Dr. Michael S. Kallos and Dr. Samer Adeeb**
8:05 – 8:45 am	**Guest Speaker #1: Dr. Michael Buschmann,** Ecole Polytechnique de Montréal "Polymer-based delivery systems : molecular, cellular and disease model studies" **Session Chairs:** Farhana Begum, University of Alberta & Taryn Ludwig, University of Calgary
8:45 – 9:55 am	**Student Podium Presentation Session #1** **Session Chairs:** Alisa Ahmetovic, University of Alberta & Swathi Damaraju, University of Calgary
Lewinson, Ryan 01	WEDGED FOOTWEAR INFLUENCES ON MECHANICAL RISK FACTORS FOR RUNNING INJURY
Randall, Alyssa 02	Comparing the Effect of Diabetes and Ischemic Preconditioning on Conduction Reserve
Friesenbichler, Bernd 03	Reduced Elbow Extension Torque during Vibrations
Qi, Liping 04	Pushrim kinetics and coordination patterns of shoulder muscles on wheelchair propulsion for different propulsion techniques
Matthiasdottir, Sigrun 05	Muscle and fascicle excursions in children with Cerebral Palsy
Hunt, Megan 06	Fractal Methods for Evaluating Growth of Embryonic Stem Cells in Static Culture

9:55-11:10 am **Poster Session #1 (ODD NUMBERED POSTERS)**

COFFEE/BEVERAGE BREAK
Max Bell 251 and Max Bell 253

Judges: Drs. Doug Hill, Martin Ferguson-Pell, Kajsa Duke, Marwan El-Rich (University of Alberta); Drs. Richard Frayne, Leping Li, Tannin Schmidt, Kristina Rinker (University of Calgary); Drs. Jon Doan, Sorina Truica (University of Lethbridge)

Purdy, Michael 01	Stimulation of neurons using new microelectrode array design
Khurshid, Madiha 03	Bioreactor Seeding of Decellularized Tissue with Endothelial Cells
Jimenez, Jon 05	Optical Detection of White Matter Function in Multiple Sclerosis Patients
McCreary, Jennifer Keiko 07	Detection of Manganese by MRI Relaxation Ratio Mapping
Bartoshyk, Patrick 09	BIOMECHANICAL BASES FOR AN INCLUSIVE ICE SKATING EXERCISE PROGRAM FOR PEOPLE LIVING WITH PARKINSON'S DISEASE: PRELIMINARY CONCEPTS
Bigdely-Shamloo, Kamran 11	T-type Calcium channel Causes Calcium-Induced Calcium-Release In Smooth Muscle Cells
Kazemi Miraki, Mojtaba 13	Poromechanical Finite Element Study of the Articular Cartilage in Partial Meniscectomy Knee Joints
Barton, Kristen 15	Characterization of Cartilage Boundary Lubricant Composition and Function of Ovine Synovial Fluid Following Knee Surgery
Guo, Malinda 17	Tissue Status Monitoring using Near Infra-red Spectroscopy
Melnikov, Andrey 19	Continuum Mechanical Model of the Cardiac Muscle
Lee, Kovid 21	Modeling, Control, and Performance Assessment of Blood Plasma Glucose Concentration in Type I Diabetics
Tomic, Aleksandar 23	Numerical Implementation of a Large-Strain Model of Porous Fibre-Reinforced Tissues
Lee, Poh Soo 25	Engineering stem cell derived bone and cartilage in novel biomimetic bioreactor
Burgoyne, Steven 27	An Implantable Baroreceptor Stimulating Device; Its Ability to Improve Renal Blood Flow
Mishriki, Shahir 29	Assessing Arrhythmia Risk in Diabetic and Ischemic-preconditioned Rat Hearts
Obrejanu, Alexander 31	Fluid Flow Induced Cell Signaling in Cardiovascular Tissues
Woloschuk, Chris 33	A Posture Training Tool for Adolescents with Scoliosis
Enns-Bray, William 35	Difference in Active Joint Laxity between Dominant and Contralateral Knees of Healthy Individuals
Adair, David 37	3D Real-Time Magnetic Resonance Imaging Application to Visualize Contrast Inflow
Ghazanfari, Amin 39	Computer Modeling of Arrhythmia Vulnerability in Diabetic Cardiac Tissue
Komeili, Amin 41	A Way to Seek the Bijective Mapping of Morphological Changes

Lee, Nathanael 43	STRUCTURAL AND MECHANICAL CHARACTERIZATION OF THE ATRIA
Chizewski, Michael 45	The influence of calcaneal motion and tibial torsion on leg axial rotation
Sawatsky, Andrew 47	DOES KNEE EXTENSOR MUSCLE IMBALANCE CAUSE CHANGES IN PATELLAR TRACKING?
Semler, Terri 49	Adhesive Capabilities of Commercially Available Surgical Glues for the Repair of Defects in the Annulus Fibrosus
Wang, Mindan Wang 51	Fabrication and Characterization of 3D Alginate-HA Hydrogel Scaffolds for SCI Repair
Rodriguez Ramirez, Marcela 53	Removal of Motion Artifact in Cardiac Optical Mapping for Complete Heart Preparations
Andrews, Stephen 55	Strain Rate Dependence of Bovine Medial Menisci in Circumferential Tension
Chow, Alexandra 57	A 3-D HYDROGEL CELL SCAFFOLD FOR ASSESSING THE BIOCOMPATIBILITY OF INTRASPINAL MICROSTIMULATION ELECTRODES

11:10 – 12:30 pm **Student Podium Presentation Session #2**

Session Chairs: Jonathon Schofield, University of Alberta & Terri Semler, University of Calgary

Melenka, Garrett 07	Strain Measurement of Orthodontic Brackets using Digital Image Correlation
Moo, Eng Kuan 08	In-situ Chondrocyte Mechanics at Different Loading Rates: A Finite Element Study
Nathoo, Nabeela 09	Susceptibility weighted imaging reveals lesions in a mouse model of multiple sclerosis
Killick, Anthony 10	Contribution of the upper body to a unique gait transition in cross-country skiing
Chalmers, Eric 11	A Pressure Control System for Brace Treatment of Scoliosis
Abubacker, Saleem 12	Cartilage Boundary Lubricating Ability of Aldehyde Modified PRG4
Ahmetovic, Alisa 13	Update on clinical feasibility of the Smart-e-Pants for prevention of deep tissue injury

12:30 – 1:45 pm **LUNCH – Vistas Dining Room**

1:45 – 2:30 pm **Industry Panel:**

Shannon Boucousis
ANT+ Design Engineer with Dynastream Innovations Inc.
Diana Shaw
Program Director - iRSM's Continuing Professional Development Program
Robert Little
President at Altair Engineering Canada, Ltd.

Session Chairs: Garrett Melenka, University of Alberta & Alyssa Randall, University of Calgary

2:30 – 2:35 pm **BREAK – Group Pictures**

2:35-3:50 pm **Poster Session #2 (EVEN NUMBERED POSTERS)**
COFFEE/BEVERAGE BREAK
Max Bell Fish Bowl and Max Bell 253

Judges: Drs. Doug Hill, Martin Ferguson-Pell, Kajsa Duke, Marwan El-Rich (University of Alberta); Drs. Richard Frayne, Leping Li, Tannin Schmidt, Kristina Rinker (University of Calgary); Drs. Jon Doan, Sorina Truica (University of Lethbridge)

Nasr, Saghar 02	Mechanical Factors driving Stem Cell Differentiation in Fracture Repair: A Biphasic FE Study of Collagen Scaffolds under Axial Compression and Bending Loads
Schofield, Jonathon 04	Knee-Ankle-Foot-Orthosis and Sit-to-Stand Biomechanics
Pansri, Siriporn 06	Molecular dynamic simulations for investigating protein adsorption to PEO surfaces
Mazloumfard, Farzaneh 08	The effect of tube wall stiffness on the speed of waves in tubes
Dwarkan, Sachitsing 10	Using the OpenCL (Open Computing Language) framework for medical image registration
Nobakht, Samaneh 12	A METHOD TO MEASURE RESIDUAL STRAINS IN THE MOUSE AORTA
Hoerzer, Stefan 14	A new methodology using Principal Component Analysis to quantify bilateral asymmetry of human gait
Twist, Elizabeth 16	Treatment of Deep Tissue Injury Using Intermittent Electrical Stimulation
Cheon, Jiin 18	Modeling the Hydrodynamics in Bioreactors for The Expansion of Embryonic Stem Cells
Kaur, Jaspreet 20	Sensitivity Analysis of Sinoatrial node
Buckley-Herd, Geoff 22	NORMAL AND OSTEOARTHRITIC SYNOVIAL STEM CELL-DERIVED TISSUE-ENGINEERED CONSTRUCTS RESPOND TO MECHANICAL STIMULUS FOLLOWING CHONDROGENIC DIFFERENTIATION
Koss, Kyle 24	MMP-2 Cleavable Peptide Hydrogel Delivery System Kinetics
Masala, Nemanja 26	Characterization of Recombinant Human PRG4 as an Ocular Surface Boundary Lubricant

Yamamoto, Maria 28	Rapid Serial Sarcomere Loss Caused by Electrical Stimulation in Rabbit Triceps Surae Muscles
Saevarsson, Stefan Karl 30	Kinematic Differences between Gender Specific and Traditional Femoral Implants
Steele, Robyn 32	Disturbed Flow Alters Nanoparticle Adhesion to Vascular Endothelial Cells
Thomson, Quinn 34	Toward an Automatic ASPECTS Method: Classification of Ischemic Brain Tissue on Non-contrast Computed-tomography Images with Image Texture Analysis
Lee, Estee 36	The Application of Prime Number-Sampling in Compressed Sensing Reconstruction
Begum, Farhana 38	Numerical Analysis of Augmented Locking Plate Fixation Repair for Proximal Humeral Fractures
Robertson, Jason 40	The Principle of Superposition During Lifting of an Object Exerting TwoDimensional External Torques
Wu, Jiajie 42	A Variable Resistance Wheelchair Ergometer for Propulsion Biomechanical Studies
Enders, Hendrik 44	Soft tissue vibration characteristics while treadmill running in shoes and barefoot
Little, Christopher 46	Hybrid Hydrogel/Polymer Scaffolds for Cartilage Tissue Engineering Applications
Behradfar, Elham 48	Extending Purkinje System Model Using Fractal Structures
Zheng, Huayang 50	3D Knee Joint Modeling From MRI Images
Akbari Shandiz, Mohsen 52	Effect of Pelvic Orientation on Radiographic Measurements of Acetabular Inclination
Baltich, Jennifer 54	Midsole Hardness, Gender & Age Effects on Lower Extremity Kinematics During Running
Sojoudi, Alireza 56	Spectral Clustering of Resting State fMRI Using a Group Similarity Matrix

3:50 – 5:00 pm **Student Podium Presentation Session #3**

Session Chairs: Garrett Melenka, University of Alberta & Emily Bishop, University of Calgary

Heik, Evelyn 14	Expansion of Skin-Derived Precursor (SKP) Cells to Promote Nerve Regeneration
Hamaliuk, Kenton 15	Development of a Long-Term Wheelchair Propulsion Instrumentation Device for Use in Evaluating Community Ambulation Parameters
Damaraju, Swathi 16	Investigations of Intercellular Communication in a 3-Dimensional Scaffold
Gallagher, Neal 17	Catheter Contact Geometry Affects Lesion Formation In Radio-frequency Cardiac Catheter Ablation
Yang, Run Ze 18	Assessment of acute ischemic stroke with near-infrared spectroscopy
Fortuna , Rafael 19	Effects of Electrical Stimulation on Muscles Injected with Botulinum Toxin Type A (Botox)

6:00 – 7:00 pm **DINNER – Vistas Dining Room**

7:00 pm **"THE GREAT CHALLENGE"** Max Bell Fish Bowl

7:15 pm	Joint UA, UC, UL Faculty Meeting – Kinnear Centre KC 205
8:00 pm	**Social – Elk and Oarsman** 119 Banff Avenue (2nd Floor, Above The Ski Hub)

SUNDAY

7:15 – 8:15 am	**BREAKFAST – Vistas Dining Room**
8:15 – 8:45 am	**Checkout**
8:45 – 9:25 am	**Guest Speaker #2: – Dr. Thomas Hangartner,** Wright State University "Accurate Segmentation of Bone in Computed Tomography Images" **Session Chairs:** Liping Qi, University of Alberta & Quinn Thompson, University of Calgary
9:25 – 10:20 am	**Student Podium Presentation Session #4** **Session Chairs:** Jiajie Wu, University of Alberta & Swathi Damaraju, University of Calgary
Ghazavi, Atefeh 20	A Finite Element Model for Extracellular Microelectrode Array Stimulation of Neurons
Bishop, Emily 22	Differences in Active Muscular Control Between Dominant and Contralateral Knees in Healthy Individuals
Luk, Collin 23	A Novel Planar Patch-Clamp Microchip For Interrogating Synaptic Activity In Neurons
Rajaram, Ajay 24	A Preliminary Study on Living-Cell Scaffolds for Nerve Tissue Engineering
10:20-10:40 am	**Poster Session #3 (FINALISTS ONLY)** **COFFEE/BEVERAGE BREAK** **Max Bell 251 and Max Bell 253** **Judges**: Drs. Doug Hill, Martin Ferguson-Pell, Kajsa Duke, Marwan El-Rich (University of Alberta); Drs. Richard Frayne, Leping Li, Tannin Schmidt, Kristina Rinker (University of Calgary); Drs. Jon Doan, Sorina Truica (University of Lethbridge)

10:40 – 11:25 am	**Student Podium Presentation Session #5** **Session Chairs:** Kamrul Islam, University of Alberta & Saleem Abubacker, University of Calgary
Madden, Ryan 25	Chondrocyte Deformations under Extreme Tissue Strains
Beveridge, Jillian 26	Joint Damage Correlates with Abnormal Knee Kinematics in Sheep
Schipilow, John 27	Bone properties in elite male alpine skiers
Najari, Mohamad 28	Orthodontic Mini–Implant Orientation Effect in Load Bearing: Finite Element Analysis
11:25 – 11:30 am	**Closing Remarks – Dr. Samer Adeeb**
11:30 – 12:00 pm	**Student-Led Activity**
	Podium and Poster Prize Presentations – Sponsored by the NSERC CREATE Training Program for Biomedical Engineers for the 21st Century
	NSERC CREATE Prize presentations for Most Outstanding Student Posters Best Overall Poster, Most Creative Poster, Clearest Message Poster NSERC CREATE Prize presentations for Most Outstanding Podium Presentations First Prize, Second Prize, Third Prize Canadian Society of Biomechanics/Société candienne de biomécanique Podium Presentation Prize Poster Presentation Prize
Islam, Kamrul 21	On Estimating Penetration Depth of the Patellofemoral Joint

Map and Meeting Location

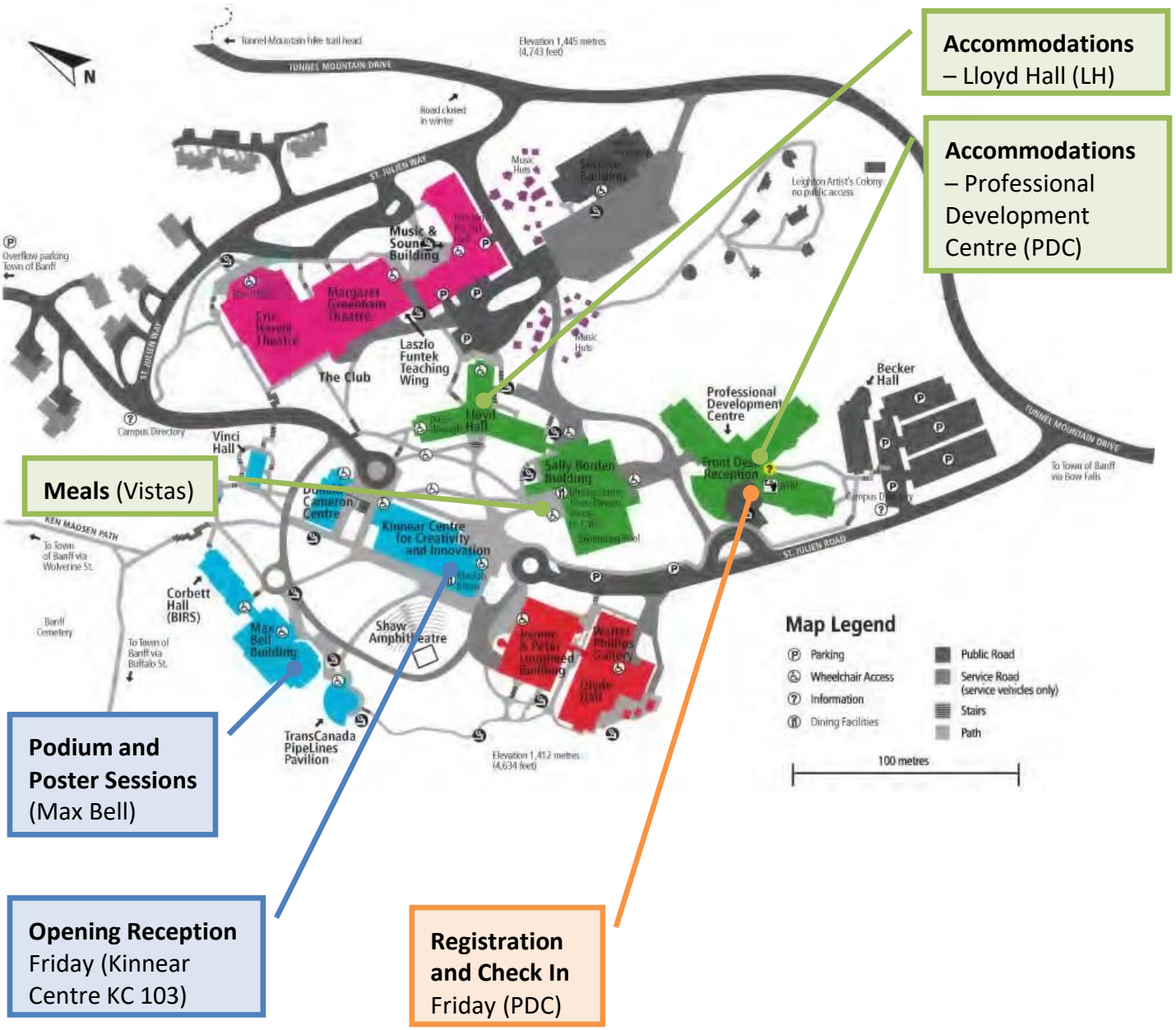

Directions to Elk and Oarsmen (Saturday Social)

119 Banff Avenue (2nd Floor, Above The Ski Hub)

Guest Speaker #1 – Dr. Michael D. Buschmann

Canada Research Chair in Cartilage Tissue Engineering; Director Biomedical Science and Technology Research Group (FRSQ); Department of Chemical Engineering; Institute of Biomedical Engineering; Ecole Polytechnique de Montréal

"Polymer-based delivery systems: molecular, cellular and disease model studies"

Abstract

We have developed polymer-based systems for cartilage repair and for delivery of nucleic acids using chitosans. Chitosans are natural polymers of glucosamine and N-acetylated glucosamine, present in different proportions, sequences and molecular weight, all of which greatly influence its physicochemical and biological properties. The

high safety profile of chitosans combined with our medical grade production and precise characterization permitted the discovery and development of a biomaterial for cartilage repair that has completed human clinical evaluation. More recent work in therapeutic delivery of nucleic acids uses nanoparticles that are electrostatic complexes of cationic chitosan with plasmid DNA (pDNA) or with small interfering RNA (siRNA). These systems have achieved high levels of transgene expression from pDNA and specific gene silencing using siRNA. A series of in vitro cell transfection studies revealed the importance of preparing specific chitosans, in terms of level of actetyl content and molecular weight, to obtain an optimal transgene expression. Live intracellular confocal imaging has provided mechanistic insight into the transfection process while physicochemical and nano-imaging have further allowed the establishment of structure/function relationships. These nanodelivery systems were then tested in vivo and shown to express the growth factors FGF-2 and PDGF-BB via subcutaneous and intramuscular administration. By further tailoring the type of chitosan used in these latter studies we were able to either stimulate or abrogate the generation of neutralizing antibodies to the transgene product, an important feature needed for effective delivery of therapeutic proteins by gene delivery. An important additional study has shown significant therapeutic potential of these systems in the delivery of glucagon-like peptide 1 in a small animal diabetes model where normalization of glucose metabolism in treated animals was achieved. Current efforts in this area are aimed at scale-up to clinical grade manufacturing and completion of proof of concept studies in distinct therapeutic areas.

Brief Bio

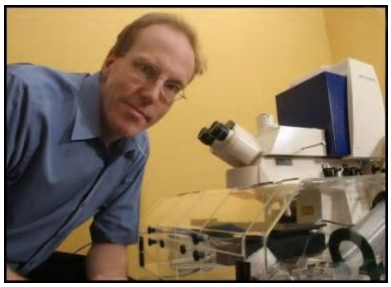

Michael Buschmann received a B. Engineering Physics from the University of Saskatchewan in 1984, and a Ph.D. in Medical Engineering and Medical Physics from the Division of Health Sciences and Technology at the Massachusetts Institute of Technology and Harvard University in 1992. His postdoctoral training in cartilage microscopy and histology was then completed at the University of Bern in Switzerland in 1994. Since 1994, Dr. Buschmann has established a multidisciplinary research program as Professor of Biomedical Engineering and Chemical Engineering at Ecole Polytechnique. The program focuses on the use of biomaterials to repair joint tissues including articular cartilage and meniscus and on the discovery and development of polymer-based gene and drug delivery systems for Diabetes, Cancer and Inflammatory diseases. (http://www.polymtl.ca/tissue/). He is one of the primary inventors of the BST-CarGel™ technology now in Pivotal clinical trial evaluation, and has been involved in founding BioSyntech (acquired by Piramal Healthcare Canada) and Biomomentum Inc, another Canadian start-up. Dr. Buschmann has published 101 articles, 219 conference proceedings and 15 patented or patent pending inventions. He is Director of the FRSQ Group in Biomedical Science and Technology and has received the Innovator Prize from the Quebec Association for Industrial Research (ADRIQ), the Melville Medal from the American Society of Mechanical Engineers (ASME), and an Award of Merit of the Canadian Arthritis Network of Centres of Excellence. He is a board member and scientific program committee member of the International Cartilage Repair Society.

Guest Speaker #2 – Dr. Thomas Hangartner

Chair, Department of Biomedical, Industrial & Human Factors Engineering; Professor, Department of Biomedical, Industrial and Human Factors Engineering, Department of Medicine and Department of Physics, Wright State University, Dayton, Ohio

"Accurate Segmentation of Bone in Computed Tomography Images"

Abstract

Computed tomography (CT) is widely used in the assessment of bone parameters in live patients and animals as well as bone samples. Quantitative analysis requires the segmentation of the bone from the surrounding tissue, and most segmentation methods rely on some type of thresholding technique. Two types of information are of interest in bone analysis from images: geometric parameters and density parameters. We know from imaging theory that blurring is an inherent byproduct of all imaging methods. Depending on the threshold used for segmentation, the object boundary moves in space due to the sloping edge. It is, thus, critical to select the threshold that creates an object boundary that reflects the actual object size. Similarly, due to blurring, the imaged density shows erroneous values at the object boundaries. Such values must not be included for an accurate representation of the object density. Using a pQCT scanner and a bone phantom with known density and geometry, we show that the thresholds for geometry and density are different. The threshold for accurate geometric segmentation is around 50% of the difference of the densities between the adjacent tissues. The threshold for accurate bone density is around 95% of the maximum density value of the bone. However, for narrow bone structures, the imaged density values are below this threshold, and alternative approaches are necessary to extract the correct density values. The specific thresholds depend on the scanner and imaging parameters, and they need to be established based on phantom measurements. We show that the mechanical behavior of bone, tested under three-point bending and torsion, correlates highly with finite-element models extracted from CT images, using the appropriate thresholding approaches.

Brief Bio

A native of Switzerland, Dr. Thomas Hangartner is the director of the Biomedical Imaging Laboratory in Wright State University, Dayton, Ohio. After obtaining his doctorate degree from the Swiss Federal Institute of Technology, Zurich, Switzerland in Physics and Biomedical Engineering, Dr. Hangartner moved to Edmonton, Canada, to become a research associate and then an associate professor in the department of biomedical Engineering, University of Alberta. In 1986, Dr. Hangartner moved to Wright State University, Dayton, Ohio to become an associate Professor in the Department of Biomedical and Human Factors Engineering. At that time, he established the BioMedical Imaging Lab with an interest in the development of new methods designed to non-invasively measure bone density. The laboratory soon started to be involved in the clinical application of newly developed methods in measuring bone density. This has been taking place through laboratory-initiated research projects and through participation in clinical trials to test new drugs for osteoporosis and related diseases. Dr. Hangartner's resume is decorated with several awards. Among them are: a distinguished professor of Biomedical Engineering Research; Outstanding Engineer and Scientist Award, Engineering and Science Foundation of Dayton; Fellow of the American Association of Physicists in Medicine; Honorary Chair, Imaging Science and Biomedical Engineering. In addition to his long track record of publications, Dr. Hangartner has different patents in the evaluation of bone strength using computer tomography.

Industry Panel

Shannon Boucousis, ANT+ Design Engineer with Dynastream Innovations Inc.

Shannon Boucousis is an ANT+ Design Engineer with Dynastream Innovations Inc., a wholly owned subsidiary of Garmin Int. and is responsible for developing ANT+ device profiles for interoperable, wireless devices in the health and fitness industry.

Shannon graduated from the University of Queensland with a First Class Honours degree in Electrical and Electronic Engineering. She also participated in an international student exchange program and an internship program, both with the University of Calgary. Through her internship position with TRLabs, Shannon was involved in cutting edge wireless technology research, leading to her Honours thesis on emerging Wifi technology, and eventually a position as an RF applications engineer for Cisco Systems in Sydney, Australia.

Shannon left Cisco Systems to pursue a personal interest in equestrian, training with Olympic level athletes in the United Kingdom, Europe and North America. She then returned to the University of Calgary to pursue an MSc at the University of Calgary, with an emphasis on electrical/biomedical engineering, specifically in the field of medical imaging. Shannon then worked as a research assistant to Dr Steven Boyd (University of Calgary) managing research on bone health in the general population, as well as various animal and patient studies.

Dynastream develops a variety of personal monitoring products, and has also developed ANT, a proprietary ultra low power wireless communications protocol. The ANT+ Alliance includes over 400 companies worldwide, such as Timex, Adidas, Garmin and many more. Shannon's role as an ANT+ design engineer involves working with these member companies and designing interoperable, wireless connectivity between their health and fitness monitoring products.

Diana Shaw - Program Director - iRSM's Continuing Professional Development Program

Industry Panel

Originally from London, UK, Dr. Shaw obtained her M.Sc. in Biotechnology at the University of Queensland, Australia, and completed her Ph.D. in Medical Genetics at the University of Calgary.

After 2 post-doctoral positions at the University of Alberta (Analytical Chemistry and Medical Microbiology and Immunology), Dr. Shaw decided to venture into the business side of science and completed a WestLink Technology Commercialization Internship, providing working experience in technology transfer, venture capital, law and high tech/spin off companies. Subsequently, Dr. Shaw was hired by Ceapro (an Edmonton-based small public healthcare company) in 2003 as Manager, Business Development then in 2006, Dr. Shaw moved to the Alberta Research Council as Director of Business Development and Marketing for Life Sciences, focusing on product development for Alberta-based biotechnology companies.

In 2007, Dr. Shaw accepted the position as Director of Business Development at the Institute for Reconstructive Sciences in Medicine (iRSM). In addition to her business development role, Dr. Shaw manages the services provided by iRSM's Medical Modeling Research Laboratory (MMRL). She coordinates the Research Services at iRSM, which has a unique translational clinical-research environment, an interdisciplinary team (including computing, engineering, industrial design, clinicians and surgeons), and access to facilities industry, healthcare and academic partners, as well as the digital design and rapid prototyping technologies in MMRL. She is the Program Director for iRSM's Continuing Professional Development Program, which encourages knowledge translation and dissemination in the applications of advanced digital technologies in reconstruction and rehabilitation.

The Institute for Reconstructive Sciences in Medicine (iRSM)

The Institute for Reconstructive Sciences in Medicine (iRSM) is an internationally recognized clinical and research institute focused on medical reconstructive sciences. It is a joint initiative of the University of Alberta, Alberta Health Services and the Covenant Health.

iRSM's decade long international reputation for innovation and advances in patient care and research has been earned by combining expertise in disciplines such as surgery, medicine, dentistry, rehabilitation medicine, engineering and computing science to create a fully integrated environment for clinical care, research, education and training in reconstructive medicine and technology. As an international referral centre, it is a leader in the complex area of osseointegration (bone) implanted devices for prosthetic replacement of skull and facial defects resulting from cancer, trauma and congenital conditions. iRSM has a reputation as a pioneer in the application of advanced technologies to support clinical and research activities. A fundamental mandate for iRSM is the development and application of new knowledge for the advancement of medical practices and quality health care. iRSM's innovative research model is comprised of multi-disciplinary teams across five faculties at the University of Alberta and extends to a number of international collaborations at leading institutions and industrial partners around the world. Research at iRSM involves both basic science and applied research. The developments taking place at iRSM are rapidly advancing Canada to a position of strength in the advancements of science and technology development for the benefits of Canadians requiring head and neck surgical care, and to develop products for the $260 billion international medical device market. iRSM actively seeks industry, institutional and independent partners. We offer access to technologies
and products with a range of clinical and prototype readiness, world-class interdisciplinary researchers, and development project opportunities.

Industry Panel

Robert B. Little – President, Altair Engineering Canada, Ltd.

Robert Little is the president of Altair Engineering Canada, Ltd. As the senior Canadian and a long-time employee at Altair, Little was asked to form Altair Canada in 2005, making it the company's fourteenth global subsidiary. The focus on Canada has allowed him to connect with Canadian universities, government organizations and manufacturing companies across a number of industries, including automotive, aerospace, rail, consumer products and heavy equipment.

Little earned a bachelor of applied science degree, followed by a master of applied science degree in mechanical engineering from Queen's University in Kingston, Ontario. He went on to earn a masters degree in business administration from the University of Michigan in Ann Arbor. Interestingly enough, it was finite element analysis research in the area of orthopaedic biomechanics for his engineering master degree that enabled him to get an early start applying the same technology for Altair's clients in the 1980's.

Little and his wife Debra have three sons and live in Windsor, Ontario. He is currently a board member of the AUTO21 Network Centre of Excellence and the SHARCNET High Performance Computing Consortium in Canada, and is Manufacturing Subcommittee Chair for the Windsor Essex Economic Development Commission.

Altair Engineering Canada, Ltd.

A leading global provider of technology that strengthens client innovation

Altair Engineering, Inc. empowers client innovation and decision-making through technology that optimizes the analysis, management and visualization of business and engineering information. Privately held, with more than 1,300 employees, Altair has offices throughout North America, South America, Europe and Asia/Pacific. With a 20-year-plus track record for product design, advanced engineering software, grid computing technologies and enterprise analytics solutions, Altair consistently delivers a competitive advantage to customers in a broad range of industries.

Altair Engineering's HyperWorks is a computer-aided engineering (CAE) simulation software platform that allows businesses to create superior, market-leading products efficiently and cost effectively. HyperWorks accomplishes this in two significant ways:

* A flexible software licensing model that replaces expensive traditional licensing plans with a pay-per-use system. Employees across organizational and geographic boundaries will be able to access simultaneously not only the HyperWorks suite, but also a broad range of complementary third-party programs and other Altair products at no extra cost.

Industry Panel

* Simulation-driven design technologies that enables achievement of performance, timing, and cost targets through rapid, low-cost, virtual exploration that accelerates informed decision making throughout the product life cycle.

Altair Engineering Canada, Ltd. is a wholly-owned subsidiary of Altair Engineering, Inc. in Troy, Michigan.

NOTES:

Podium Presentation Abstracts

WEDGED FOOTWEAR INFLUENCES ON MECHANICAL RISK FACTORS FOR RUNNING INJURY

*Ryan T. Lewinson, Jay T. Worobets & Darren J. Stefanyshyn

*Human Performance Laboratory, University of Calgary, Calgary, Alberta, *lewinson@ucalgary.ca*

Introduction

Approximately 50% of all runners will develop a running-related injury in a given year [1,4]. In an assessment of biomechanical risk factors for running injury, Stefanyshyn et al. [3] found that healthy subjects who experience increased knee abduction moments-of-force (KAMs) and increased knee external rotation moments-of-force (KXMs) during running are more likely to develop a running injury over a six month period. Therefore, one possible approach to running injury prevention is minimizing the KAM and KXM magnitudes that runners experience. Knee joint moments can be reduced during walking using wedged footwear [2]; however, their effects during running remain unknown. The purpose of this study was to determine the effects of medially and laterally wedged footwear on KAMs and KXMs during running.

Methods

Nine healthy male subjects volunteered to participate in the study (age: 25±3 years; mass: 76±5 kg; height: 178±7 cm). Three retroreflective markers were placed on each of the right shoe, shank and thigh segments of each subject. Subjects were then asked to complete 5 trials running at 4m/s with each of 3 footwear conditions: neutral shoes with (1) no insert, (2) a 9mm medial wedge insert, and (3) a 9mm lateral wedge insert. Body segment kinematics and groundreaction kinetics were recorded
simultaneously during each trial using an 8camera Motion Analysis system at 240 Hz, and a Kistler force platform at 2400 Hz, respectively.

A standard inverse dynamics approach was used to calculate the peak KAMs and KXMs for each subject and footwear condition. Footwear conditions were compared by one-way repeated-measures ANOVA (α=0.05). Paired *t*-tests with Bonferroni corrections were used for posthoc analysis.

Results

Peak KAMs (p=0.001) and peak KXMs (p=0.037) were significantly different across footwear conditions. KAMs decreased by 12% with lateral wedge use and increased by 13% with medial wedge use during running. KXMs were decreased by 16% with lateral

wedge use and increased by 16% with medial wedge use during running (Figure 1).

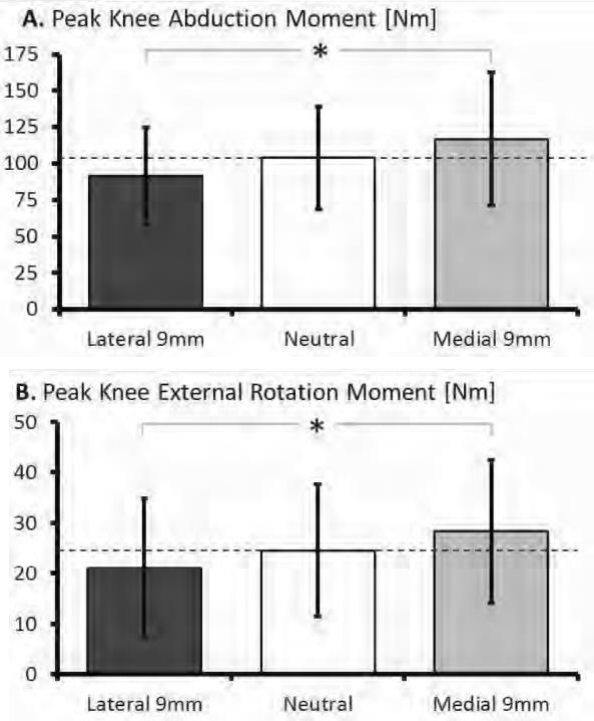

Figure 1. Mean(S.D.) knee joint moments (n=9) for each footwear condition. * indicates *p*=0.002.

Conclusions

Laterally wedged footwear can decrease peak knee abduction and external rotation moments during running, while medially wedged footwear does the opposite. It is recommended that laterally wedged footwear be tested as an intervention for healthy runners to determine if incidence of running injury can be reduced.

References

1. Matheson, G.O. et al. (1989). *American Journal of Sports Medicine.*
2. Radzimski, A.O. et al. (2011). *The Knee.* 3. Stefanyshyn, D.J. et al. (2001). *Proceedings of the 5th Symposium on Footwear Biomechanics.*
4. van Mechelen W. (1992). *Sports Medicine.*

Comparing the Effect of Diabetes and Ischemic Preconditioning on Conduction Reserve

[1]A Randall, [2,3,4]A Nygren

[1]Biomedical Engineering Graduate Program, [2]Dept. of Electrical & Computer Engineering,
[3]Centre for Bioengineering Research and Education, and [4]Libin Cardiovascular Institute, University of Calgary

Introduction

Healthy heart tissue has a large conduction reserve, i.e., many gap junctions can become non-functional without affecting the speed of electrical propagation in the tissue. Our lab has demonstrated that diabetes induced with Streptozotocin (STZ**)** causes disorganization of gap junctions, resulting in a decrease of the conduction reserve of the tissue [1].

The observation that brief episodes of ischemia can activate protective mechanisms, allowing the heart to better withstand subsequent longer-duration ischemia, is known as ischemic preconditioning (IPC). Literature results have shown that IPC causes a similar disorganization of gap junctions [2] indicating a similar mechanism may be involved in STZ and IPC. The purpose of this work is to compare conduction reserve in IPC and STZ treated tissue.

Methods

Animals were divided into 4 groups; Control, Control with STZ induced diabetes, IPC and IPC with STZ. Animals were euthanized; their hearts excised and perfused with a Kreb's buffer using the Langendorff method. After a 20 min stabilization period, IPC hearts were subjected to two episodes of stopped flow for 3 min followed by 5 min reperfusion. Control hearts were continually perfused for the same length of time. Two different trials were completed for each of the 4 groups: 1) a measure of conduction reserve was obtained by determining the effect of high extracellular K^+ on the tissue's activation time (AT) (inversely proportional to speed of conduction); and 2) the response of the AT to ischemia was measured 2 and 5 min into a third and final ischemic episode. In both experiments, ATs were normalized to the value obtained immediately prior to increasing $[K^+]$ and onset of ischemia, respectively. AT was evaluated using optical mapping techniques [1].

Results

Experiment 1: Normalized activation times (NAT) shows a significant depletion of conduction reserve in STZ however IPC has no significant effect on the conduction reserve of either Control or STZ hearts. IPC did have the trend (not statistically significant) to increase NAT in controls by 11% and decrease NAT by 8% in STZ. Experiment 2: STZ+IPC and IPC NAT in response to the IPC protocol were not statistically different. NAT is shown for 2 and 5 min ischemia in Figure 1. NAT STZ and STZ+IPC were significantly higher than control for the first 2 min ischemia however not at 5 min. Inversely IPC was not significant at 2 min ischemia but was at 5 min.

Conclusions

IPC and STZ have a similar slowing of conduction velocity in response to ischemia. IPC appears to have no significant effect on conduction reserve of the tissue (assessed with high $[K^+]$), while previous STZ treatment does. Against our hypothesis, the IPC protocol applied to STZ tissue has a trend to decrease the AT (thus increasing the conduction reserve of the tissue).

These results indicate that while similar mechanisms may be activated in STZ and IPC, their interaction is complex. A longer IPC protocol should be tested to clarify the effects of IPC.

References

[1] PMID: 21037228
[2] PMID:18519446

Figures

Figure 1: Experiment 1, NAT at 2 and 5 min isch.

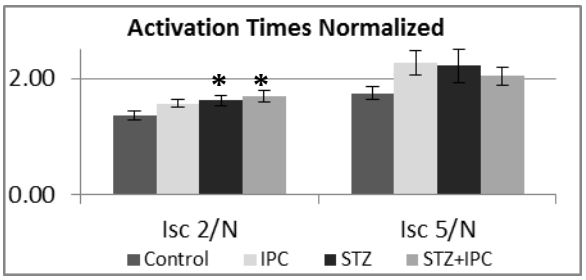

*p>0.05 with respect to Control

Reduced Elbow Extension Torque during Vibrations

Bernd Friesenbichler[1], Aurel Coza[1], Benno M. Nigg[1]

[1] Human Performance Lab, University of Calgary, 2500 University Dr NW, Calgary, AB, Canada, T2N 1N4

Introduction: Soft tissue vibrations are often the result of impacts during walking, running, skiing and other physical activities. The acute effects of vibrations on force generation have rarely been tested and are generally little understood. A systematic study of muscle force production and its dependency on superimposed vibrations could help researchers to tune vibration characteristics in order to modify contraction strength and efficiency. The current study investigates the influence of systematically changing vibration frequency on maximum elbow extension torque and muscle activity.

Methods:

A pneumatic vibrator was mounted onto the crank of a dynamometer which allowed for the superposition of longitudinal vibrations transmitted to the forearm of the subjects. Fifteen healthy female subjects were instructed to perform a series of maximal voluntary isometric contractions (MVCs) against the crank (elbow extension). The upper arm to forearm angle (elbow angle) was set at 60, 90 and 120 degrees (where 180 deg = full extension). At each angle, subjects performed one control MVC without vibrations and three MVCs with vibrations at different vibration frequencies. Extension torque was quantified by the dynamometer; vibration frequency and amplitude were quantified using an accelerometer attached to the bony part of the wrist. Muscle activity (EMG) of the triceps and biceps brachii, and extension torque in vibration and non-vibration trials were recorded and compared using a paired Student's t-test ($p < 0.05$) and Pearson correlation coefficients were used to correlate torque and muscle activity to vibration frequency.

Results:

The vibration frequency ranged between 20 and 40 Hz at an average vibration amplitude of 5.9 mm ± 2.25 mm (peak to peak) at the wrist level. During vibration exposure, maximal torque decreased significantly relative to non-vibration control by 1.8 % (± 5.7 %), 7.4 % (± 7.9 %) and 5.0 % (± 8.2 %) at 60, 90 (Fig. 1) and 120 deg, respectively. Correlation of torque to frequency changes were between r^2 = 0.014 and 0.116 and not significant. Muscle activity during vibration exposure increased significantly in both, triceps (agonist) and biceps (antagonist) by ~ 30 to 40 % (Fig. 1) at each elbow angle and the correlation to frequency was between r^2 = 0.000 and 0.09 and not significant.

Discussion and Conclusions:

One potential reason for the surprising finding may be that roughly equal increases in muscle activity produce different moments about the elbow joint since the moment arms of tri- and biceps change at each elbow angle but clearly not by the same magnitude. At 60 deg, the difference in moment arm length is small (~0.4cm), but at 90 and 120 deg, the difference increases about five-fold (~2.0cm) [1] in favor of the

biceps (antagonist) und thus may produce a larger counter-moment during vibrations. The data revealed that, depending on the elbow angle but independent of vibration frequency, maximal extension torque dropped during vibration exposure although muscle activity increased in tri- and biceps.

References:

[1] Murray W, Delp S, Buchanan T. J Biomech 28, 513-525, 1995.

Figures:

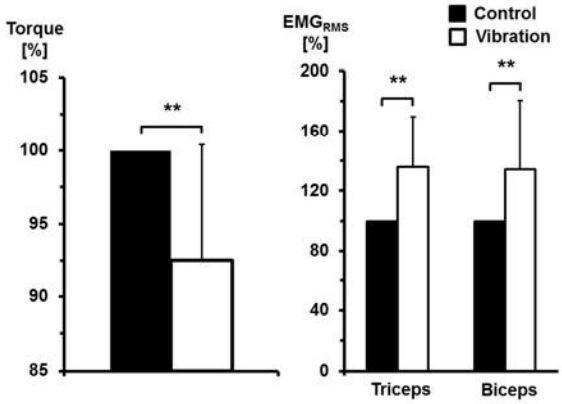

Figure 1: Maximum extension torque and muscle activity at 90 deg elbow angle ($p < .01$).

Pushrim kinetics and coordination patterns of shoulder muscles on wheelchair propulsion for different propulsion techniques

Liping Qi[1], James Wakeling[2], Simon Grange[1], Martin Ferguson-Pell[1]
Faculty of Rehabilitation Medicine, University of Alberta, Edmonton, Alberta, Canada, T6G 2G4
[2] Department of Biomedical Physiology and Kinesiology, Simon Fraser University, BC, Canada, V5A 1S6

Introduction

Individuals undergoing treatment for a spinal cord injury (SCI) learn to use a wheelchair as soon as they are stable and able to sit up without complications. However the use of a wheelchair, which is intended to restore mobility, may not be without risk. Upper limbs of wheelchair users are subjected to unnatural loading conditions and repetitions of use. Over time, shoulder joints associated with the upper limbs of manual wheelchair users inevitably deteriorate. One recommendation to patients in the clinical practical guidelines for the preservation of upper limb function following spinal cord injury is that for each propulsion stroke their hands move in a semicircular pattern and continue below the pushrim in the recovery phase [1]. For our study, a short propulsion technique instruction session was designed to examine the effects of the semicircular motion technique on wheelchair biomechanics, shoulder muscle coordination patterns in particular. Our hypothesis is that muscle recruitment for semicircular motion propulsion will elicit significant changes in muscle coordination patterns compared to those for self-selected propulsion techniques.

Methods

15 able-bodied participants (8 males, 7 females, age: 30±4 years, weight: 65±12 kg) volunteered to participate in this study. Surface electromyography (sEMG) activity of 7 upper extremity muscles was recorded using parallel-bar EMG Sensors. The SMARTWheel (Three Rivers Inc., LLC, Mesa, AZ, USA) was used for the collection of kinetic data. The wheelchair kinetics and EMG activities of 7 muscles were recorded during wheelchair propulsion on an ergometer with a self-selected propulsion technique and a semicircular technique. The kinetics variables, and the onset, cessation, duration of EMG activity from 7 muscles were compared for 2 sessions with paired ttest. Muscle coordination patterns across 7 muscles were analyzed by principal component analysis (PCA) [2, 3].

Results

The push frequency was significantly lower ($P<0.05$) in the semicircular technique than in the self-selected technique without significant increases in push forces, while the push length, push time, and push distance were significantly longer in the semicircular rather than in the self-selected stroke technique. The

semicircular technique showed more synergistic muscle coordination than the self-selected technique during wheelchair propulsion for inexperienced able-bodied subjects.

Conclusions

Our results show that the semicircular technique has a favorable effect on wheelchair kinetics and shoulder muscle recruitment patterns in inexperienced ablebodied subjects. This study thus showed an association of muscle recruitment patterns with different propulsion stroke techniques. The next step will be to explore the role of muscle coordination in injury etiology in order to determine which muscle coordination patterns are the most likely to prevent injury.

References

1. *Preservation of upper limb function following spinal cord injury: a clinical practice guideline for health-care professionals.* J Spinal Cord Med, 2005. **28**(5): p. 434-70.

2. Qi, L., et al., *Changes in surface EMG signals and kinetics associated with progression of fatigue at two speeds during wheelchair propulsion.* Journal of Rehabilitation Research and Development 2011. (In press)

3. Qi, L., et al., *Spectral properties of electromyographic and mechanomyographic signals during isometric ramp and step contractions in biceps brachii.* J Electromyogr Kinesiol, 2011. **21**(1): p. 128-35.

Muscle and fascicle excursions in children with Cerebral Palsy

[1]Sigrun Matthiasdottir, [1]Marlee Hahn, [1]Megan Yaraskavitch, [1]Walter Herzog
[1]Human Performance Lab, University of Calgary, Canada

Introduction

Cerebral Palsy (CP) is a static lesion in the brain that happens before, during or shortly after birth. It is a non-progressive disorder that leaves children with permanent motor impairments [1]. Many children with CP have spasticity. Joint contractures often form when spastic muscles become taut and inhibit the full range of motion (ROM) of the joint [2]. The detailed reasons for why muscles become taut remain unknown. It has been suggested in some studies that short fascicle lengths (FL) in spastic muscles cause tightening [3] but other studies do not confirm these findings [4]. The purpose of this study was to measure FL and muscle and fascicle excursions of the medial gastrocnemius (MG) for the full passive ROM of the ankle in children with CP and typically developing (TD) controls.

Methods

The experimental group included 9 children with CP between the ages of 8 and 16. The control group included 14 age and sexmatched TD controls. The children were seated in the chair of a Biodex™ System III dynamometer and their foot was strapped to a footplate. EMG electrodes were placed on the MG and the tibialis anterior muscles. An ultrasound probe was fixed to the lower leg to visualize the myotendinous (MT) junction first and the mid-belly of the MG muscle second. Torque, ankle angle and EMG data were collected for four passive trials covering the full ROM of the ankle joint. A common ROM was defined as the range from the lowest maximum dorsiflexion to the lowest maximum plantarflexion found between all subjects. Fascicle lengths and MT displacements were measured from the ultrasound images. In cases where fascicle lengths were not fully visible, trigonometric relationships were used to calculate fascicle lengths from the measured pennation angle (α) and muscle thickness (Tm). Nonparametric Mann-Whitney U-statistics (α=0.01) were used to test for differences between groups.

Fractal Methods for Evaluating Growth of Embryonic Stem Cells in Static Culture

Megan M. Hunt[1,2], Ian D. Gates[2], Michael S. Kallos[1,2]

[1] Pharmaceutical Production Research Facility, Schulich School of Engineering, University of Calgary, Alberta

[2] Dept. of Chemical and Petroleum Engineering, Schulich School of Engineering, University of Calgary, Alberta

Results

The common ROM was 87-126°. Fascicle lengths at all ankle angles were shorter for CP children (Figure 1), while fascicle excursions over the common ROM were not significantly different from TD control subjects. However, fascicle excursions as a percent of resting fascicle lengths were significantly greater for CP subjects. Muscletendon excursions over the common ROM were greater for control group subjects. Fascicle excursions as a percentage of muscle-tendon excursions were greater in children with CP compared to TD controls.

Conclusions

Our results confirm previous findings that FL are shorter in children with CP compared to TD children. We also show that fascicle excursions relative to fascicle lengths and muscle-tendon excursions are greater in children with CP over a universal ROM. This novel result has important implications for the impairment of function in CP children during everyday movements.

References

1. Campell SK. *Decision Making in Pediatric Neurologic Physical Therapy*. Philadelphia: Churchill Livingstone, e89-97,1999

2. Pontén E, et al. *Muscle and Nerve* **36**, 47-54, 2007.

3. Mohagheghi AA, et al. *Developmental Medicine and Child Neurology* **50**, 44-50, 2008. 4. Malaiya R, et al. *Journal of electromyography and Kinesiology* **17**, 657-663, 2007.

Figures

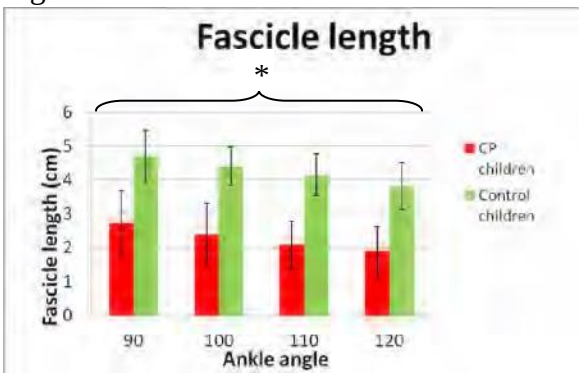

Figure 1: Fascicle lengths

Introduction

Ultimately, tissue engineering aims to repair and heal diseased tissues. The building blocks used in tissue engineering are living cells or cell aggregates. Embryonic stem cells (ESCs) are rapidly emerging as a promising cell source due to their unique characteristics – namely their ability to readily proliferate in culture as well as their potential to differentiate into all adult cell types. However, cell manufacturing and regulatory challenges must be overcome before clinical application of ESC therapies will be viable. One approach consists of predictive strategies via computer modeling methods to predict ESC culture outcomes based on various input parameters. To date, several groups have used mathematical modeling and analysis techniques to describe cell proliferation and differentiation based on uncertain cell, substrate, fluid, and fluid flow characteristics e.g. population, wettability, and concentrations, respectively. Here, we explore fractal

analysis to characterize cell growth as indicated by cell culture morphology.

Methods

Two cell lines were used for these experiments. Mouse ESCs (D3 line) were grown in static six-well plates in DMEM +10%FBS at 37°C and 5% CO_2. Brightfield images were taken at 10 minute intervals over a 4 day period. Human ESCs (CA-1T line) were grown in static six-well plates in mTeSR on Matrigel at 37°C and 5% CO_2. Brightfield photos were taken at every cell count time point. Images were processed by using ImageJ software (NIH). Brightfield images were converted to binary ones and analyzed by using the FracLac fractal analysis plugin for ImageJ. The box counting method was used to evaluate fractal dimension. Multifractal analysis was also done to further characterize cell culture morphology.

Results

The fractal dimension was determined for mouse ESCs over one passage and was found to increase at an approximately linear rate to a maximum value equal to about 1.8. As cell number and corresponding culture area increases at an exponential rate versus time, we conclude that the fractal dimension is indeed a function of cell morphological complexity.

Conclusions

Future studies will include analysis of induction of differentiation to all three germ layers. Ultimately the ability to detect small changes in cellular complexity via fractal dimension may allow for better control over directed differentiation.

Figures

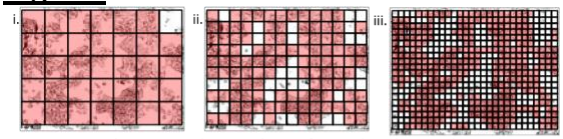

Box counting to determine fractal dimension i) N=34 ε=200μm, ii) N=108 ε=100 μm, iii) N=418 ε=50 μm.

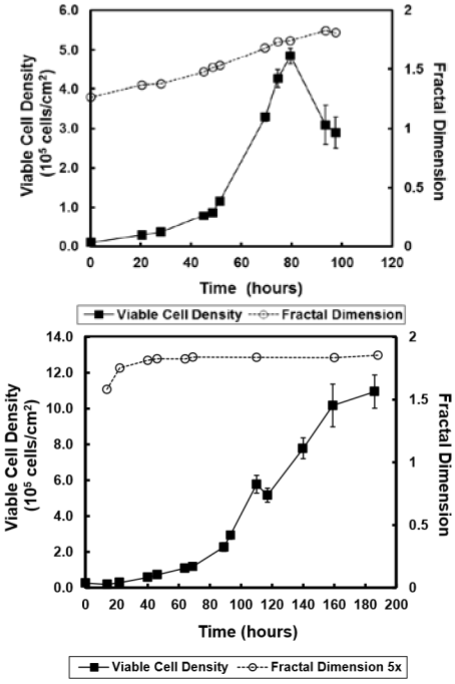

Top Plot: Comparison of fractal dimension and viable cell density over one passage of mouse ESCs. Bottom Plot: Comparison of fractal dimension and viable cell density over one passage of human ESCs.

Strain Measurement of Orthodontic Brackets using Digital Image Correlation

Garrett W. Melenka, David S. Nobes, Jason P. Carey
Department of Mechanical Engineering, University of Alberta, Edmonton AB T6G 2G8

Introduction: Braces and archwires are commonly used by orthodontists to correct tooth misalignment (malocclusions). Tooth motion, in orthodontics, is achieved by applying forces and moments to the crown of the tooth with orthodontic brackets and archwires. Understanding the deformation of the brackets is required to improve treatment efficiency and to create an accurate model of the bracket-archwire- tooth complex[1].

The objective of this work was to design a contact free measurement system to observe and measure the wire/bracket

interaction during rotation of an archwire within a bracket slot.

Methods: We developed an optical strain measurement technique to allow for contact free strain measurement of orthodontic brackets. Using the concept of digital image correlation (DIC) to calculate the strain fields from images acquired using a high resolution camera[2]. With this method we can determine the two dimensional (2D) deformation of an object, such as an orthodontic bracket[3] (Figure 1). To expand on the strain measurement of orthodontic brackets, we developed a stereo digital image correlation technique to determine three dimensional (3D) deformations between pairs of stereo images. We compared titanium and stainless steel brackets deformation versus wire angle of twist, among other tests, using the DIC method.

Results: DIC results show that the stainless steel brackets exhibited greater plastic deformation than the titanium brackets indicating that material properties affect how the brackets respond to loads applied by an archwire (Figure 2). 3D imaging tests were performed on orthodontic brackets using a stereo microscope to quantify the in plane and out of plane motion of the brackets (Figure 3).

Conclusions

The development of this contact free strain measurement system will have immediate applications in orthodontic design and procedures, as better modeling of tooth response to applied forces can be achieved. Tooth response can be used to create simulations that predict treatment outcomes and to design patient specific treatments. Beyond this specific application, 2D and 3D contact free strain- field measuring systems can be applied to engineering applications where direct strain measurement is difficult or impractical due to the geometry, complex loading conditions or scale of the components.

References

1. Archambault A., et al *Angle Orthod*, *80*(1), 201-10.
2. Pan B et al, *Meas. Sci. Technol*, *20*(6), 062001.
3. **Melenka, GW**, et al, *Eur J Orthod (Accepted 2011-09-01)*

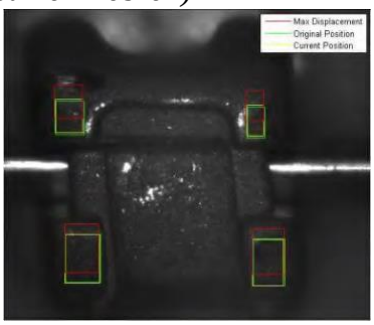

Figure 1: Deformation of an Orthodontic Bracket Caused by Archwire Rotation

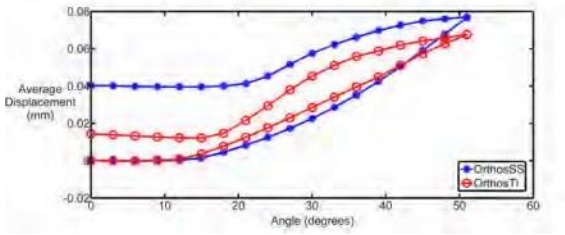

Figure 2: Comparison of Titanium and Stainless Steel Orthodontic Bracket Deformation

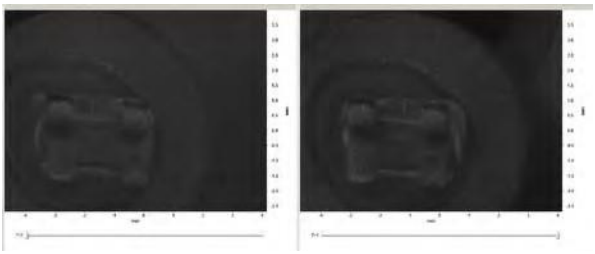

Figure 3: Stereo Images of Brackets used for Deformation Measurement

In-situ Chondrocyte Mechanics at Different Loading Rates: A Finite Element Study

E.K. Moo[1,2], W. Herzog[2], S.K. Han[3,2], N.A. Abu Osman[1], B. Pingguan-Murphy[1], S. Federico[2]

[1] University of Malaya, Malaysia; [2] The University of Calgary, Canada; [3] University of Maryland, USA

Introduction

Mechanical impact loading involving cell death is thought to cause osteoarthritis onset and progression [1]. In order to understand why in-situ cells die readily following impact loading but remain unaffected when the same load is applied at a slow rate, we used finite element modelling of articular cartilage and chondrocytes to study the *in-situ* cell mechanics (which cannot be measured experimentally due to technical limitations). The objective of this study was to investigate the effects of strain rates on *in-situ* chondrocyte mechanics. We hypothesized that differences in cell mechanics at different strain rates might point to the reason(s) for cells dying at high but not at low strain rates.

Methods

A two-scale modelling approach was used to describe the cartilage tissue (macroscale model) and the embedded cells (microscale model) [2]. The tissue model consists of a layer of cartilage "mounted" on a layer of subchondral bone. The cell model consists of a chondrocyte surrounded by its cell membrane, pericellular matrix, pericellular capsule, and the neighbouring extracellular matrix [4]. Both models are non-linear and biphasic with an isotropic hyperelastic potential and a void ratio dependent permeability [3]. The depthdependent material constants were derived from published data [5]. Finite Element analysis was performed using ABAQUS v6.10. A confined compression test at 5% nominal strain was applied onto the articular surface at different strain rates (0.167-500 %/s). The calculated time-dependent variables of interest (deformation and pore pressure) were then applied as boundary conditions for the micro level cell model.

Results

Cell deformations (fig. A) were highest at the impact strain rates, but did not reach failure levels. Tangential tensile membrane strain rates (fig. B) were highest at the highest loading rate and were observed primarily in superficial zone cells.

Discussion and Conclusion

Our results suggest that cell death in impact loading is caused by high tangential tensile strain rates in the cell membrane, causing membrane rupture and loss of cell integrity.

References

[1] Blanco et al. 1998. Arthritis Rheum, 41(2): 284-289. [2] Guilak et al. 2000. J Biomech, 33(12): 1663-1673. [3] Holmes MH and Mow VC. 1990. J Biomech, 23:11451156. [4] Wu JZ, et al. 1999. J. Biomech, 32:563-572. [5] Wang et al. 2003. J. Biomech, 36(3): 339-353.

Fig. A. Compressive cell strain as a function of strain rate

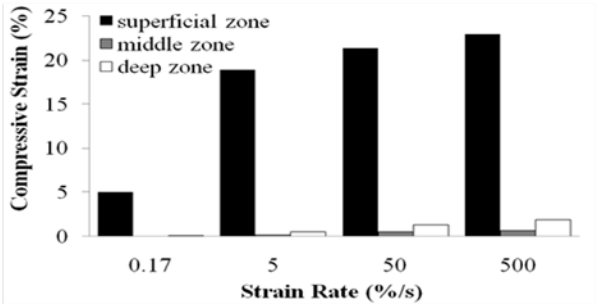

Fig. B. Tangential tensile membrane strain as a function of strain rate

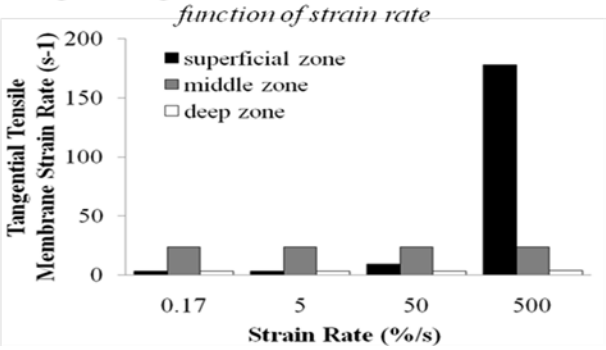

Acknowledgments: OA Team grant and ISB.

Susceptibility weighted imaging reveals lesions in a mouse model of multiple sclerosis

Nabeela Nathoo, Ying Wu, Smriti Agrawal, Sarah Haylock-Jacobs, Samuel Barnes, Andy Obenaus, Tad Foniok, Voon Wee Yong, Jeff F. Dunn
Hotchkiss Brain Institute, Faculty of Medicine, University of Calgary, Calgary, AB T2N 4N1

Introduction

Multiple sclerosis (MS) is an inflammatory, demyelinating neurological condition. In Alberta, 1 out of every 350 people is affected by MS. As there is no known cause for MS, the proposed theory of chronic cerebrospinal venous insufficiency (CCSVI) has gained considerable attention. CCSVI proposes that impaired venous drainage results in iron deposition in the brain and leads to the development of MS [1]. CCSVI is having a profound effect on the MS community, leading to a number of MS patients undergoing experimental endovascular treatment without validation of CCSVI by scientific studies. MRI methods sensitive to iron, such as susceptibility weighted imaging (SWI), have shown ironrelated lesions in human MS patients [2,3]. We investigated if SWI shows iron-related lesions in the commonly used mouse model of MS, experimental allergic encephalomyelitis (EAE).

Methods

Female C57BL/6 mice were induced with EAE using methods described previously [4]. A 9.4T MRI console was used for *in vivo* high-resolution 3D gradient echo with full flow compensation on the cerebellum and lumbar spine (n = 19) (image parameters: matrix=192x128x32, FOV=0.92x1.28x1.28cm, TE/TR=4/50, flip angle=15°).

Magnitude and phase MRI data were processed using SPIN software to create SWI images. A 32x32 Hanning filter was applied to phase images with a negative phase mask to show the susceptibility effects of iron. Phase data was multiplied into magnitude data 4 times to make SWI images.

Prussian blue staining for iron was performed for correlation with SWI MRI. We also performed a study where mice were imaged *in vivo* using the same sequence and parameters as above, perfused, and then put back in the MRI for imaging using the same sequence and parameters that were used preperfusion for *in vivo* imaging (n = 10).

Results

In the lumbar spine, SWI lesions were observed in white matter, where some corresponded to iron deposition. Lesions were also seen at the grey/white matter boundary (G/WMB) of the spinal cord. Many G/WMB SWI lesions disappeared post-perfusion.

In the cerebellum, SWI lesions were seen in white matter tracts. These lesions corresponded to perivascular cuffs, where some were iron-related (Fig. 1). Many of these lesions disappeared post-perfusion.

Conclusions

Our data show that SWI lesions exist and are regionally specific in the EAE mouse. Some SWI lesions are iron-related, but many are associated with the vasculature. These

lesions may originate from hypoxic or inflamed veins. EAE is not induced by venous occlusion, but rather is an inflammatory model with a phenotype similar to that seen in MS. The presence of SWI lesions in EAE is not specific to venous occlusion during induction of disease.

References

[1] Zamboni, P. et al. J Neurol Neurosurg Psychiatry 80, 392-399 (2009).
[2] Haacke, E.M. et al. J Magn Reson Imaging 29, 537-544 (2009).
[3] Eissa, A. et al. J Magn Reson Imaging 30, 737742 (2009).
[4] Agrawal, S. et al. J Neurosci 31, 669-677 (2011).

Figures

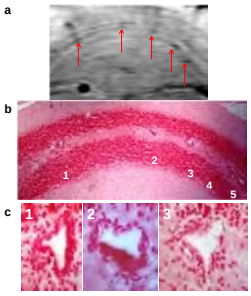

Figure 1. SWI lesions in the cerebellum correspond to

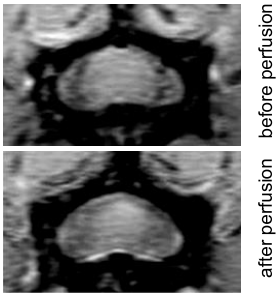

Figure 2. SWI lesions seen pre-perfusion disappear post-perfusion. perivascular cuffs.

Contribution of the upper body to a unique gait transition in cross-country skiing

Anthony Killick, Sean Crooks, Haakon Lenes, Walter Herzog
University of Calgary

Introduction

With increasing speeds of locomotion, animals change their gait pattern to minimize metabolic cost. For example, a horse will walk at low speeds, trot at intermediate speeds, and gallop at high speeds (1). Similarly, cross-country skiers use the two-skate technique at low speeds, transition to the one-skate technique at intermediate speeds, but then, contrary to everything known about gait transitions in two-legged and four-legged locomotion, skiers revert back to the two-skate technique at very high speeds. The difference between the one- and two-skate techniques is defined by the coordination of the poling cycles performed with the arms and the skating cycles performed with the legs. In the oneskate technique, poles are planted simultaneously with every skate stride, while in the two-skate technique, poles are planted with every second skate stride (2). Previous data from our group showed that the transitions from two- to one- and back to the two-skate pattern are indeed associated with trying to minimize the cost of transport, defined as the oxygen uptake required per distance traveled. The purpose of this study was to explain how the two-skate technique has a lower cost of transport than the oneskate technique at very low and very high, but not at intermediate skiing speeds.

Methods

Four trained cross-country ski racers performed two separate tests for each technique of skate skiing. First, subjects skied at 6, 15, and 30 km/h on a rollerski treadmill. These speeds were selected because the differences in oxygen cost between the two techniques were found to be greatest at these speeds in previous testing. During the entire test, oxygen uptake, forces transmitted by the skiers through the poles, blood lactate concentration, and 3-dimensional, high speed kinematics, were recorded for one technique and repeated on a separate day using the second technique.

In the second phase of testing, the metabolic cost of the poling motion was determined on a pole ergometer with subjects matching their stroke rate and poling forces using video and force feedback. These tests were performed for all speeds and both techniques tested in the first set of rollerski tests, while also measuring oxygen uptake. Leg

movements were limited by bracing of the knee and ankle.

Results

Oxygen uptake was similar for roller skiing at 6 and 15km/h. However, at 30km/h, oxygen uptake for the one-skate technique was significantly greater (4 ml/kg/min) than for the two-skate technique. The average metabolic cost associated with the upperbody work alone was 66, 63, and 60% of the total body oxygen uptake at 6, 15, and 30 km/h respectively for the one-skate technique and was 61, 56, and 57% for the two-skate technique. On average, metabolic cost of the upper body was always higher for the one-skate compared to the two-skate technique. Conclusions

Skiing at 6 and 15km/h requires the same metabolic energy in the one-skate and two skate techniques, although the arms and poles seem to contribute more to propulsion in the one-skate than the two-skate technique, based on their metabolic requirement. However, at 30km/h, the oneskate technique requires more metabolic cost than the two-skate technique. Since the skating action with the legs is similar between the one- and two-skate techniques, but the arm action occurs at a much higher frequency in the one- compared to the twoskate technique, we propose that it is primarily the arm action that limits efficient skiing at high speeds in the one-skate technique.

References

(1) Hoyt et al., Nature, 292, 240, 1981.
(2) G. Smith, in Handbook of Sports Medicine and Science: Cross Country Skiing, H. Rusko (Blackwell Publishing), 2002, p. 32-60

A Pressure Control System for Brace Treatment of Scoliosis

E Chalmers[1,2], E Lou [1,2], D Hill[2], V Zho[1], MS Wong[3]

[1] Department of Electrical & Computer Engineering, University of Alberta, Edmonton AB Canada

[2] Glenrose Rehabilitation Hospital, 10230 11 Ave, Edmonton AB Canada, T5G 0B7

[3] Department of Health Technology and Informatics, The Hong Kong Polytechnic University, Hong Kong

Introduction

Adolescent Idiopathic Scoliosis is a deformation of the spine involving abnormal curvature and vertebral rotation. It affects 3% of the population [1]. Bracing attempts to avoid corrective surgery by preventing curve progression, and is the most commonly used non-surgical treatment. Controlled studies of bracing show high success rates, but in practice two problems are encountered: wear-time is often unknown, and brace tightness can fluctuate with activity [2]. This paper reports the development and validation of a system to monitor brace wear-time and control brace tightness.

Methods

The system consisted of four monitorregulator units to be installed at key pressure points in the brace. Each unit included a microcontroller system, an inflatable air bladder, and a gauge pressure sensor. A closed control loop used feedback from the sensor and inflated/deflated the bladder to regulate the pressure applied to the patient's body. The algorithm was designed for good performance in real conditions, while avoiding too-frequent or unnecessary pressure adjustments. The unit monitored brace wear-time by sensing the patient through a breathing detection algorithm applied to pressure readings. The system was designed to be small, for low power consumption and minimal user interaction.

Four healthy subjects wore an instrumented brace for 2 hours without

pressure regulation and 2 hours with regulation. Each test began with target pressure at 5.3 kPa, and the percentage of pressure readings falling in a target range of 5.3 ± 0.67 kPa was calculated. The brace wear-time logged by the system was also compared to the actual wear-time recorded by the subjects.

Results

Enabling the system decreased the amount of time spent below the target range for all four subjects (Fig 1). On average the percentage of pressure readings in the desired range doubled (from 31% to 62%). The measured brace wear-time agreed with subject's records in all cases. Each unit could run for one month on a battery charge, and log pressure readings for one year. The units did not reduce the comfort of the brace or affect the patient's activities.

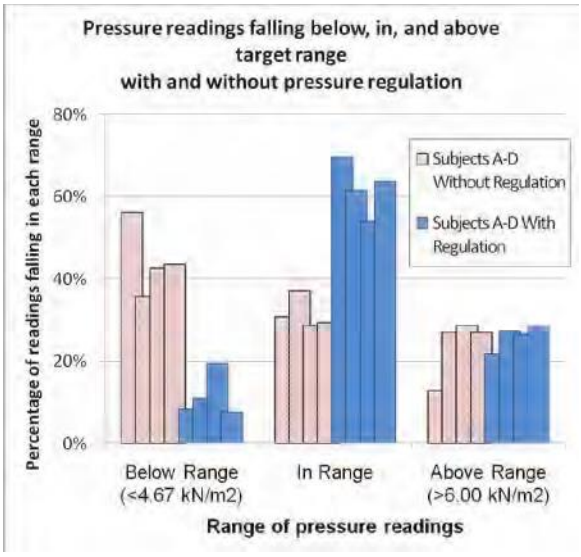

Fig 1. Test results showing the system's ability to increase time spent in a desired brace pressure range.

Conclusions

The pressure control system improves the consistency of brace pressure, and accurately monitors brace wear-time. These results indicate that the system should improve brace treatment effectiveness.

References

[1] Lonstein J, "Adolescent Idiopathic Scoliosis", lancet 1994, 344(8934): 1407

[2] Mak I, *et al.* "The effect of time on qualitative compliance in brace treatment for AIS", Prosthetics & Orthotics International 2008, 32(2):136-144.

Cartilage Boundary Lubricating Ability of Aldehyde Modified PRG4

[1] [2] [2] [1]
Abubacker, S; Ham H O; Messersmith, P B; + Schmidt, T A
+[1]University of Calgary, Calgary, AB, Canada; [2]Northwestern University, Evanston, IL, USA

Introduction Proteoglycan 4 (PRG4) is a mucinous glycoprotein present in synovial fluid and at the surface of articular cartilage where it functions as a critical boundary lubricant necessary for joint health[1]. A recent study, motivated by diminished PRG4 levels associated with early osteoarthritis (OA), demonstrated aldehyde (CHO) modification of PRG4 significantly enhanced its binding to a depleted articular surface[2]. However, it remains to be determined if CHO modification alters the friction-reducing ability of PRG4. Hence, the objective of this study was to assess the cartilage boundary lubricating ability of CHO modified PRG4 (PRG4-CHO).

Methods PRG4 was prepared by purification from media conditioned cartilage explants from bovine stifle joints, as described previously[3]. PRG4-CHO was prepared using succinimidyl 4-

formylbenzamide (CHO) at a PRG4:CHO molar ratio of 1:1000 in 100mM PO_4 buffer as previously described[2]. A treatment control (PRG4-SHAM) was exposed to modification buffers and incubations in the absence of CHO. PRG4 samples were prepared at a physiological concentration of 450 μg/mL[3] in phosphate buffered saline (PBS). PBS and bovine synovial fluid (SF) served as negative and positive controls, respectively. Each lubricant was assessed using a previously described *in vitro* cartilage-on-cartilage friction test under boundary lubricating conditions[3]. Static ($\mu_{static,Neq}$) and kinetic ($<\mu_{kinetic,Neq}>$) friction coefficients were then calculated[3].

Results All PRG4 preparations functioned as effective friction-reducing cartilage boundary lubricants. Lubricants and Tps (pre-spin durations) modulated friction. $\mu_{static,Neq}$ varied with Tps and test lubricant (both $p<0.001$), with an interaction ($p<0.01$). Values increased with Tps and were consistently highest in PBS (ranging from 0.30±0.04 to 0.57±0.06) and lowest in SF (0.032±0.003 to 0.26±0.03). Values in PRG4, PRG4-SHAM, and PRG4-CHO were intermediate and similar to each other (**Fig. 1A**). $<\mu_{kinetic,Neq}>$ values exhibited similar trends, varying with lubricant and Tps (both $p<0.001$) increasing only slightly with Tps (values at Tps=1.2s were within 19±12% of those at Tps=1200s). $<\mu_{kinetic,Neq}>$ values at Tps=1.2s were greatest in PBS (0.24±0.04) and lowest in SF (0.024 ± 0.003). Values in PRG4 (0.11±0.02), PRG4-SHAM (0.15±0.02), and PRG4-CHO (0.15±0.01) were again intermediate and significantly different than PBS and SF (both $p<0.05$), but not statistically different from each other ($p=0.55$-1.00, **Fig. 1B)**.

Conclusions This data indicates that CHO modified PRG4 maintains its ability to function as an effective friction reducing cartilage boundary lubricant. The lubrication test data suggests that CHO modification does not significantly affect the protein structure or lubricating function of PRG4, which is consistent with a previous study examining CHO modification[2]. CHO modification may be a useful approach for molecular resurfacing of tissue surfaces, specifically articular cartilage, with lubricating molecules such as PRG4, potentially providing enhanced biotherapeutic treatment of early OA, since local administration of PRG4 has been shown to be chondroprotective in OA animal models[4].

References

[1]Jay *Curr Opin Orthop* '04, [2]Chawla+ *Acta Biomat* '10, [3]Schmidt+ *A&R* '09, [4]Flannery+ *A&R* '08.

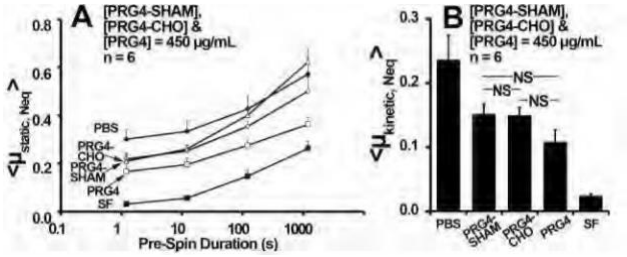

Figure 1: Static ($\mu_{static,Neq}$) (**A**) and kinetic $<\mu_{kinetic,Neq}>$ at Tps=1.2 s (**B**) friction coefficients PRG4-SHAM, PRG4CHO and PRG4 at 450 μg/mL. NS = not statistically different from each other.

Update on clinical feasibility of the Smart-e-Pants for prevention of deep tissue injury

Alisa Ahmetovic[1], Lisa Kawasaki[1], Dana Schnepf[2], Ryan Sommer[3], Vivian Mushahwar[1,4], and K. Ming Chan[1]

[1] Centre for Neuroscience, Univ Alberta, [2] Allen Gray Continiuing Care Centre, Glenrose Rehabilitation Hospital, [3] Dept. Cell Biology, Univ Alberta, Edmonton, AB, Canada [4] AHFMR Interdisciplinary Team in Smart Neural Prostheses

Introduction

Pressure ulcers around the ischial tuberosities are common in people with impaired mobility. They result from muscle ischemia and breakdown caused by prolonged loading and deformation. Our group showed in rats that intermittent electrical stimulation (IES) prevents the formation of deep tissue injury (DTI) - pressure ulcers of deep origin. In addition, we showed that IES redistributed pressure and increased oxygenation in the loaded muscles. This work led to the development of the Smart-e-Pants system for the prevention of DTI in human patients. The goal of this study is to test the feasibility of Smart-e-Pants in 2 settings: a long term care facility (LTCF) and a rehabilitation hospital (RH). We reported our preliminary 'system component testing' results at the BME 2010 conference for 3 subjects at LTCF. We have since tested the complete system in a greater number of subjects.

Methods

***Smart-e-Pants* system** (Fig. 1) is comprised of surface electrodes, a garment to secure the electrodes on the skin, and a stimulator with data logging capabilities. With the stimulating electrodes placed on the motor points of the gluteus maximus muscles, open loop stimulation at 17.5 Hz is triggered every 10 minutes for 10 seconds.

***Study protocol**:* Subjects who are cognitively competent with intact skin and body mass index <32 were recruited. The system was implemented for 5 weeks in each subject, except in cases of earlier hospital discharge. Subjects wore the system 12 hours each day, 4 days a week. Incontinent participants wore the surface electrodes directly on their skin while continent participants also trialed the garment that keeps the electrodes in place. Outcome measures included caregiver demands, participant feedback, and skin and muscle contraction monitoring. Smart-ePants improvements were made and implemented based on the subjects' and caregivers' feedback.

Figure 1: Smart-e-Pants System prototype

Results

LTCF recruitment was challenging due to population's declining cognitive abilities, advanced age, fragile skin and obesity. Over the past year, we have succeeded in recruiting 4 subjects. In contrast, we have already recruited 6 subjects over the past 6 months at the RH spinal cord injury unit. Overall, the caregivers and participants feedback have been positive. All subjects reported that the system did not interfere with their daily activities and IES was an acceptable part of their daily routine. Time required to don the system was between 1020 minutes and doff between 5-10 minutes. This is substantially shorter compared to the cumulative time needed to turn the subjects every 2 hours. With 1 exception of a small skin tear in an elderly participant, the skin had not reacted negatively to the electrodes or electrical stimulation. Contractions in the LTCF subjects were more variable particularly in the morning when the system was donned. In contrast, contractions in the

RH subjects were elicited with greater ease and were more stable and consistent throughout the day.

Conclusions

So far, clinical implementation has showed that the deployment of the Smart-e-Pants system is easier in the RH setting but is also feasible in the LTC environments. It is well accepted by end-users with minimal skin concerns. Further testing in intensive care units and home settings is planned.

Acknowledgements: AHFMR

Expansion of Skin-Derived Precursor (SKP) Cells to Promote Nerve Regeneration

Evelyn Heik[1], Holly M. Wobma[1], Jochen Fahr[1], Rajan Kumar[2], Jeff Biernaskie[2], Raj Midha[3], Michael S. Kallos[1]

[1] Pharmaceutical Production Research Facility (PPRF), University of Calgary, 2500 University Dr NW, Calgary AB

[2] Department of Comparative Biology and Experimental Medicine, 3330 Hospital Dr NW T2N 4N1

[3] Department of Clinical Neuroscience, 3330 Hospital Dr NW T2N 4N1

Introduction: The current standard for treating peripheral nerve damage is to take a piece of nerve from another region of the body and use it to suture the free nerve endings at the damaged site[1]. Because of the often low-integrity and scarcity of these donor nerves, it is desirable to come up with alternative treatment methods. One option is to regenerate the damaged nerve using stem cell-based therapies. Encouragingly, in recent years, a type of skin-derived stem cell (SKP) has been identified, which can differentiate into Schwann cells and promote nerve regeneration in animal models[2,3].

To use SKP cells in the clinic, it is important to be able to produce them in sufficient quantities. Bioreactors may be able to be used for this purpose[4]; however, they require a threshold number of cells before they can be used. To address this, we have been exploring methods to initially expand SKP cells in static culture. As with other neural precursors, SKP cells grow as spheres of cells, which must be dissociated to single cells for passaging[2]. There are several dissociation methods, including chemical and enzymatic. For this study, our aim was to identify which of the methods would lead to the highest cell growth and viability, and the best retention of the SKP cell phenotype (spherical aggregates) vs. differentiated cells (attached to the dish).

Methods: SKP cells were cultured in SKP proliferation media at 37°C and 5% CO_2 in T-25 and T-75 flasks. Enzymatic dissociation was investigated using Collagenase XI, 0.05% Trypsin-EDTA and Accutase. Chemical dissociation was performed by exposing cells to basic medium (pH 11.7) followed by neutralization with acidic medium (pH 2)[4]. Following aggregate dissociation, cell counts and viability were determined using a hemocytometer. Microscopy was then used to reveal cell morphology, an indicator for SKP cell phenotype. Dissociated cells were then cultured for 12 days and the fraction of unattached cells (i.e. SKP cells) was measured.

Results: All three enzymes successfully dissociated cell aggregates. Cells treated with Trypsin and Accutase tended to adhere to the culture flask surface and subsequently differentiate into fibroblast cells, whereas treatment with Collagenase XI led to round, free-floating aggregates, high growth rates, and, importantly, high viabilities. Figure 1 illustrates the fractions of free-floating (SKP) and adherent (differentiated) cells

following treatment. It was also found that chemical dissociation did not break up SKP cell aggregates.

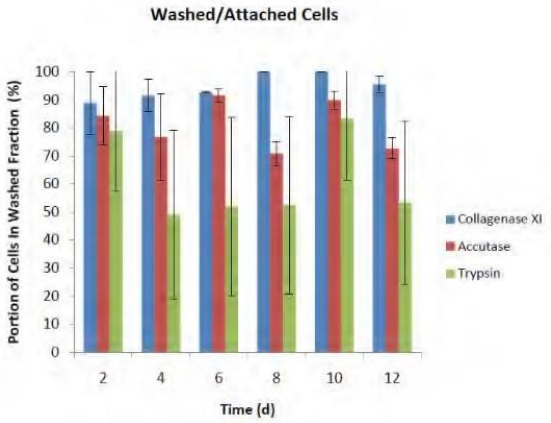

Figure 1: Portion of cells in the washed fraction compared to the attached cells over 12 days.

Conclusions: Our data show that cell dissociation using Collagenese XI best promoted cell viability and growth, while maintaining the SKP cell phenotype. This is an important first step in producing therapeutically relevant quantities of SKP cells in bioreactors for therapeutic use.

References:

1. Evans, G.R.D. *Anat. Rec.* **263**, 396-404 (2001). **2.** Biernaskie, J. *et al. J. Neurosci.* **27**, 9545-9559 (2007). **3.** Walsh SK, Biernaskie J, Kemp SWP, Midha R. *Neuroscience* **164**, 1097107 (2009). **4.** Sen, A., Kallos, M.S. & Behie, L.A. *Tissue Eng.* **10**, 904-913 (2004).

Development of a Long-Term Wheelchair Propulsion Instrumentation Device for Use in Evaluating Community Ambulation Parameters

Kenton Hamaluik, Jiajie Wu and Martin Ferguson-Pell
Faculty of Rehabilitation Medicine, University of Alberta, Edmonton, Alberta, Canada
AHFMR Bone and Joint Health Team Grant

Introduction

The reported prevalence of overuse injuries and chronic pain in the shoulders and upper extremities of long-term manual wheelchair users (MWUs) ranges from 30-60%. Failure to achieve functional goals due to exertional challenges of wheelchair use are unknown, but likely to be a cause of significant social isolation. Boninger et al (2005) and Mercer et al (2006) have demonstrated a direct correlation between extended exertion related to manual wheelchair propulsion and pain and injury. A widely adopted method for measuring the exertion levels of MWUs is the SmartWheel (SW) (Three Rivers, AZ). SWs are instrumented manual wheelchair wheels capable of directly measuring the forces and torques applied to the rim during propulsion. While SWs are an excellent tool in a clinical setting, they are not well-suited to community ambulation studies as they are intended for brief periods of measurement. In principle, by recording kinematic parameters of manual wheelchair propulsion such as velocity, acceleration, and cadence, the application of Newton's laws of motion should allow the direct calculation of propulsion forces - significantly simplifying the monitoring technology and allowing it be packaged for relatively low cost for deployment on any manual wheelchair for an extended period of time in the user's reallife environment.

Methods

A custom fabricated measurement and recording system ("Tachyon") was developed to measure key wheelchair perforamance parameters: wheel velocity, pitch, yaw and roll, heading, ambient conditions (temperature and humidity) and heart rate. The Tachyon system can also wirelessly communicate with a 6 degree of freedom inertial measurement unit (IMU) and potentially a GPS unit. The IMU measures internal movement of the wheelchair user's upper body relative to the wheelchair base, which affects stability and propulsion biomechanics. All data is collected continuously and streamed to an SD card for later retrieval and analysis

Results

The Tachyon units performed as designed and record all information accurately and successfully. By sending the Tachyon units to sleep when the wheelchair user was inactive, the Tachyon device was able to operate autonomously without being charged for approximately 5-6 days, a length of time that is acceptable for collecting community ambulation data. Estimating propulsion forces using wheelchair dynamics has proved to be more complex than anticipated. Upper body inertial effects contribute significantly to instantaneous acceleration readings, thereby confounding estimates of propulsion forces. Models are being developed using the IMU to account for these effects. In the meantime Tachyon is proving very effective in collecting "real world" data that can be used to develop 'biomechanical virtial reality scenarios' that can be 'replayed' in the laboratory where Smartwheel technology and motion capture can be deployed for accurate measurement of propulsion biomechanics.

Conclusions

Tachyon collects a rich array of data on wheelchair propulsion in community settings. It also has to the potential to study biomechanics of wheelchair propulsion for elite wheelchair athletes. Collecting data to inform the design of biomechanically realistic virtual scenarios is opening up interesting opportunities to study performance and factors influencing overuse injuries in long term wheelchair users in community ambulation settings.

References

M. Boninger, A. Joontz, S. Sisto, T. DysonHudson, M. Chang, R. Price, and R. Cooper. Rehab.Res. Devel. 43:9-19, 2005.

J. Mercer, M. Boninger, A. Joontz, D. Ren, T. Dyson-Hudson, and R. Cooper. Clin. Biomech., 21:781-789, 2006.

Investigations of Intercellular Communication in a 3-Dimensional Scaffold

Swathi Damaraju, Neil A. Duncan

McCaig Institute for Bone and Joint Health, University of Calgary

Introduction

Cells cultured in 3D scaffolds can better mimic their physiological environment[1]. It is well established that there is an interconnected relationship between connexin containing gap junctions, cadherins, and integrins in bone cell communication and the response of bone cells to mechanical stimulation[2]. Using this knowledge, *in-vitro* 3D stem cell culture models for *ex-vivo* bone tissue investigations can offer insight into the role of cell communication in the healing of bone defects[1,2]. The aim of this work was to determine the activity and presence of cadherins and connexin containing gap junctions in murine embryonic stem cells seeded in a three dimensional collagen scaffold.

Methods

Murine embryonic stem cells were maintained in T75 culture flasks, and after 3 to 4 passages, 1 million cells were spun down and re-suspended in media containing pro-osteoblastic-gamma-carboxyglutamic acid-containing protein (BGP) (260mg/ml of media). The suspension was combined with purified bovine collagen I (Advanced BioMatrix), seeded in 24-well plates, and incubated at 37°C for 5, 15, 20 and 30 days. At each time point, fluorescence recovery after photobleaching (FRAP) was performed with and without communication blockers.

Octanol was used as a general communication blocker, and 18-alphaglycyrrhetinic acid (AGA) was used as a specific and reversible gap junction blocker.

Immunofluorescence for osteoblastcadherin, connexin-32, and connexin-43 was performed. A Zeiss LSM510 confocal microscope was used for all imaging.

Results

Differences between average maximum percent recovery in early (day 5) and late (days 15, 20, and 30) differentiated murine osteoblasts was significant at $\alpha = 0.05$ (Fig. 1). Octanol and AGA treatment significantly blocked gap junction activity (Fig. 1). Immunofluorescence showed increased presence of osteoblast-cadherin, connexin32, and connexin-43 in day 15, 20, and day 30 differentiated murine osteoblasts than day 5 (Fig. 2).

Figures

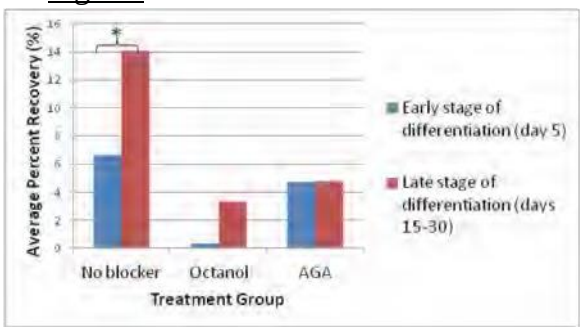

Fig. 1: FRAP recovery with and without communication blockers

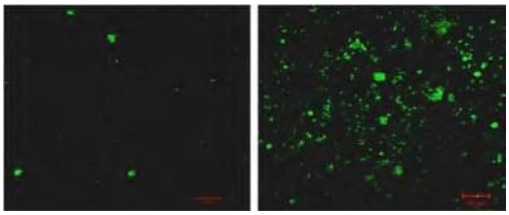

Fig. 2: Immunofluorescence (green) of osteoblast-cadherin:d5 (left) and d30 (right).

Catheter Contact Geometry Affects Lesion Formation In Radio-frequency Cardiac Catheter Ablation

Neal P. Gallagher, Elise C. Fear, Israel A. Byrd, Edward J. Vigmond
ELECTRICAL & COMPUTER ENGINEERING – 2500 UNIVERSITY DR NW – CALGARY AB T2N 1N4

Conclusions

The results from the current study demonstrate that murine embryonic stem cells guided to differentiate into osteoblasts in a collagen I construct increase gap junction activity and presence of connexins and cadherins as differentiation progresses. Future studies using these cell-gel scaffolds will provide an understanding of the importance of intercellular communication to the proliferation of embryonic stem cells in an *ex-vivo* bone fracture, and the role of mechanical stimulation in the healing process of bone tissue.

References

1. Thompson et al. In-vitro models for bone mechanobiology. ProcIMechE,224:1533–1541, 2010.
2. Grimston et al. Role of connexin-43 in osteoblast response to physical load. Ann NY Acad Sci, 1068:214–224, 2006.

Introduction

Radio-Frequency Catheter (RFC) ablation is a minimally invasive interventional technique that can be effectively used to treat many different conditions. Of particular interest is the demonstrated efficacy in treating cardiac arrhythmia, specifically the most prevalent arrhythmia in North America, atrial fibrillation (AF). Procedural success in RFC ablation is highly dependent on deep lesion formation which, in turn, is inextricably linked with catheter/endocardial surface contact; a contact that is extremely difficult to assess given the complex 3D anatomy of the left atrium. The goal of this study is to use a detailed computer model to evaluate the effect that varying catheter contact (both incident angle and penetration depth) has on lesion

formation and the maximum temperature reached.

Methods

To investigate the effect that the catheter's geometric parameters (angle and penetration depth into the tissue) have on lesion formation, a fully coupled electro-thermal model was created. A homogeneous slab of tissue was suspended in a saline solution and permittivities and conductivities chosen to mimic those of endocardial tissue and blood. The catheter's penetration depth and angle was varied and the ensuing electroquasistatic problem was solved.

Using the resulting current density distribution, the Pennes bioheat equation was solved to get a time dependent temperature map. According to current research, atrial tissue undergoes cellular necrosis at around 50˚C meaning that it is no longer electrically viable after this point. Accordingly, the 50˚C isotherm was used to demarcate the lesion boundary. The simulations were run for 60 s and the overall lesion volumes and maximum temperature values were tracked for future comparison.

Results

Results show that catheter contact angle plays a significant role in not only lesion volume and formation rate but also in the maximal temperature detected in the region. In a simulation with contact angle of 15˚ and a penetration depth of 4mm (Fig 1), the temperature reaches unsafe levels (100˚C) in just 2.07s leaving a lesion volume of only 51.75mm^3. If the catheter angle is set instead to 90˚ given the same penetration depth Fig 2), it takes 10.35s for 10˚0C to be reached. This allows more time for the heat to propagate into the tissue and the resulting lesion is much larger (117.7mm^3)!

Conclusions

Catheter contact angle (not just penetration depth as previously thought) plays an integral role in lesion formation and maximal temperature detected. Clinically, as the angle is unknown, there is significant danger of runaway temperatures causing patient safety concerns. More work must be done to provide real-time catheter contact assessment to the physician.

References

[1] *Pac. Clin. Elecphys 29.11 (2006): 1285-297.*
[2] *IEEE Trans.onBiomedEng.51.8(2004) 1478-486.*
[3] *Phys Med Biol. 1996 Nov;41(11):2271-93.*
[4] *Aerosp.Med.1971 Jan; 42(1):24-7.*

Figures

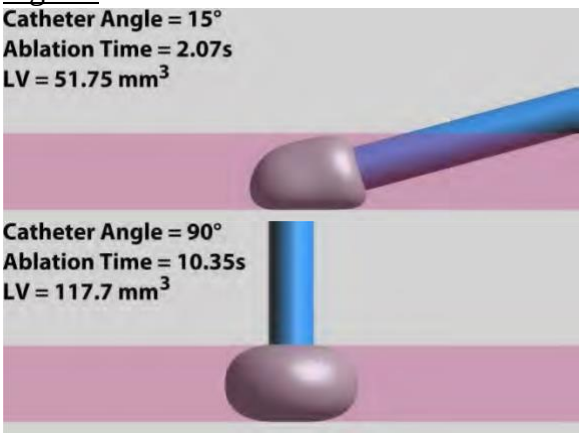

Figs. 1&2: Lesion Volume (LV) shown at instant of maximum temperature. Despite having the same penetration depth, a larger lesion is present in Fig 2.

Assessment of acute ischemic stroke with near-infrared spectroscopy

Run Ze Yang, Francois Moreau, Andrew Demchuk, Bijoy Menon, Jeff F. Dunn
Hotchkiss Brain Institute, Faculty of Medicine, University of Calgary, Calgary AB, T2N-4N1

Introduction

Stroke is the 3rd leading cause of death for Canadians (Heart and Stroke, 2011). The most widely used method of assessing stroke is CT, which has limitations. It cannot provide continuous monitoring of patients; it is time consuming; and when used alone, it cannot predict brain tissue viability. Nearinfrared spectroscopy (NIRS) is capable of measuring blood oxygenation, which may provide information about tissue viability and vessel status. The applicability of NIRS has been demonstrated in rat stroke models (Abookasis, 2009). We wanted to investigate its applicability for stroke management in acute stroke patients.

Methods

A group of cadavers (n=6) were measured to validate accuracy of our frequency domain(FD) NIRS system, called ISS. Patients with unilateral middle cerebral artery (MCA) occlusion of the M1 segment that were admitted to the hospital within 6 hours of symptom onset were immediately enrolled (n=3). We used the ISS to measure both ipsilateral as well as contralateral to the occlusion. Multiple areas supplied by the M1 segment of the MCA were measured for roughly 40 seconds. Cerebral metabolic rate for oxygen ($CMRO_2$) was calculated with additional flow data from CT perfusion; the data was also used to determine if NIRS can detect artery recanalization.

Results

The tissue oxygen saturation for cadavers is ~0% as we expected, strengthening the ISS's validity. In acute stroke patients, we observed a decline in tissue oxygen saturation (compared to the normal side) in regions that were known to be ischemic ($p<0.01$; Fig. 1a). The saturation remained low when patients did not recanalize ($p<0.01$; Fig. 1b), but increased when there was recanalization. By combining the data from CT perfusion and NIRS, we were also able to show a significant reduction in $CMRO_2$ in ischemic regions, a condition evident in most acute stroke patients

Conclusions

The FD-NIRS system ISS has the ability to provide rapid assessment of stroke patient condition. We have demonstrated that it is capable of detecting artery recanalization. Combined with CT perfusion, we are also able to accurately estimate $CMRO_2$, which is a very effective marker of tissue status and eventual tissue fate.

References

Abookasis, D. et al. J Biomed Opt. 2009; 14(2): 024033

Heart and Stroke: http://www.heartandstroke.on.ca/

Figures

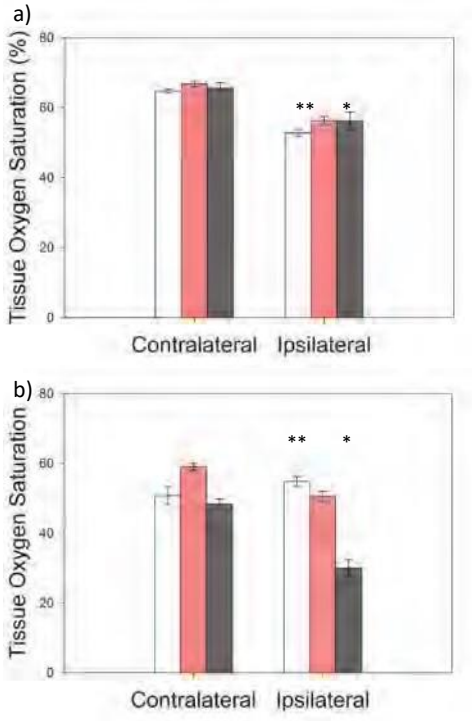

Figure 1: NIRS measurement of tissue oxygen saturation (S_tO_2) (mean ± SD) in three patients. White, pink and black bins show patient 1's frontal lobe, patient 2's Wernicke's area and patient 3's Broca's area. **a)** Both showed a decline in S_tO_2 in the putative stroke region. **b)** 3 days follow up of patients. Patient 1 recanalized and showed a relative increase in S_tO_2. Patient 2 and 3 did not recanalize, and the S_tO_2 stayed low. (*- indicates significant difference from contralateral side, $p<0.05$).

Effects of Electrical Stimulation on Muscles Injected with Botulinum Toxin Type A (Botox)

Rafael Fortuna, Monika Horisberger, Robert Van der Marel, Walter Herzog
Human Performance Laboratory, Faculty of Kinesiology, University of Calgary

Introduction

Botulinum Toxin Type A (BTX-A) injections are a common treatment modality used in neuromuscular disorders characterized by increased neuromuscular activity, such as cerebral palsy. BTX-A acts by blocking acetylcholine release at the neuromuscular junction, inducing chemical denervation and muscle paralysis. The positive effects of BTX-A injections are well established [1]. However, previous works have shown that BTX-A treatment has specific adverse effects including muscle atrophy and contractile material loss in target and non-target muscles [2, 3]. We speculated that such adverse effects might be prevented if BTX-A injected muscles could be submitted to regular exercise. However, due to the BTX-A-induced chemical ablation, voluntary exercise is precluded, but direct electrical stimulation (ES) of the target muscles is feasible and may offer an opportunity to prevent the adverse effects induced by BTX-A treatments. Therefore, the aim of the present study was to verify the effects of direct ES on muscle mass and contractile material of the quadriceps femoris muscles of New Zealand White (NZW) rabbits.

Methods

Seventeen, one year old, female NZW rabbits were divided into three groups as follows: Control (n=5), BTX-A (n=5), and BTX-A+ES groups (n=7).

Control group rabbits received saline injections. Rabbits in BTX-A groups received monthly BTX-A injections (3.5U/Kg) into the left quadriceps for six months. In addition, the BTX-A+ES group was exposed to three weekly ES training session (15mins; 0.5s on/1.5s off at 20% of maximum force).

Outcome measures included muscle mass and the percentage of contractile material. Muscle mass was assessed by weighing the muscle. The percentage of contractile material was determined histologically by calculating the area fraction of contractile material compared to the total muscle crosssectional area.

A 3 way-ANOVA with the main factors leg (injected and non-injected), groups (Control, BTX-A, BTX-A+ES), and muscles (vastus lateralis, rectus femoris and vastus medialis) was performed using a level of significance of 0.05.

Results

Muscle mass in target muscles was greater for the BTX-A+ES compared to BTX-A group. Moreover, muscle mass for the non-target muscles of BTXA+ES group reached control group values ($p<0.05$; results not shown).

The percentage of contractile material was 96% in control rabbits. Contractile material was significantly decreased for the target (43% ±9.7) and non target vastus lateralis (74% ±6.5) in BTXA group rabbits. Following direct ES, contractile material for BTX-A+ES group rabbits was significantly greater in the injected limb (72%) and the contralateral limb (96%), showing that ES partially and fully preserved the contractile material in target and non-target muscles, respectively (Figure 1; $p<0.05$).

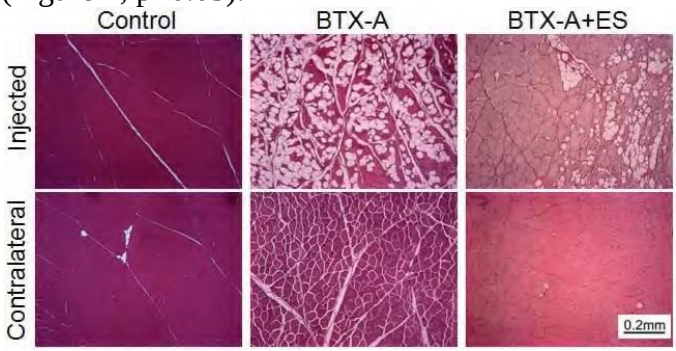

Fig 1 Muscle histology of the injected (first row) and contralateral (second row) for the Control (left), BTX-A (middle) and BTX-A+ES group rabbits (right).

Conclusion

Direct ES of BTX-A injected muscles partially and completely preserves muscle mass and contractile material in target and non-target muscles, respectively. These results suggest that direct ES may be a valuable companion to BTX-A treatments, allowing for the beneficial effects of the treatment while simultaneously limiting adverse effects.

References

1. Brin, MF. *Muscle & Nerve* **6**, 146-168, 1991.
2. Fortuna R, et al. *J Biomech* **44**, 39-44, 2011.
3. Yaraskavitch M, et al. *J Biomech* **41**, 897-902, 2008

A Finite Element Model for Extracellular Microelectrode Array Stimulation of Neurons

A. Ghazavi[1], D. Westwick[1], C. Luk[2], N. I. Syed[2], C. Dalton[1]

[2]
Department of Electrical and Computer Engineering, Department of Anatomy and Cell Biology, University of Calgary, Calgary, Alberta, Canada

Introduction

Microelectrode array (MEA) is a noninvasive method for recording brain cell activity and has been successfully applied to an array of neurons. However, using MEAs to consistently stimulate neurons over an extended period of time has been less successful and continues to be problematic. In order to optimize the neuron stimulation in a physiological manner, it is necessary to design a more effective neuron-electrode junction. Several finite element models have been used for neuronal simulation, with investigations considering: the influence of electrode size on the recorded signal amplitude [1], current and potential field distributions around a stimulating MEA [2], different cell and electrode radii and various sealing gap thicknesses [3]. However, optimized microelectrode size, shape, material, adhesion material and thickness used at the cell-electrode interface have not been investigated.

In the present research, the electric field pattern for different stimulation voltages, electrode dimensions and materials is being investigated, in order to optimize the electrode geometry to obtain the largest electric field in the cell.

Methods

A stationary and transient finite element model has been developed in twodimensions to simulate voltage stimulation of large neurons from the mollusk *Lymnaea* on a 30um diameter electrode (Figure 1) covered with a thin layer of SU8 dielectric material, which makes the electrode an inert substrate for neuron interface. This prevents electrolysis of the electrode. Three domains have been simulated: the extracellular and intracellular medium, and the electrode. The electric fields in the electrode as well as the soma have been investigated by initially stimulating the neuron with constant and ramp voltages.

Results

The electric field is largest at the edges of the electrode, decreasing towards the center by ~78%. The next largest field is at the edges of the cell, since the electric field is larger at sharp points as shown in Figure 2. For a given stimulation voltage, the ramp voltage would induce a larger electric field than the constant voltage. However, the model needs to be refined to show more specific bioelectrical activity in the cell membrane (i.e., voltage-gated channels in the cell membrane).

Conclusions

The electric field induced by the applied voltage is more effective at the edges of the electrode. Therefore, it would be better if designed electrodes were smaller than the neuron being investigated. Splitting the solid 30μm electrode into a ring or star structure would provide stronger electric fields over a larger area. The simulation also shows that using a ramp voltage for stimulation is very effective in triggering action potential. The simulation results are being compared with experimental data from the Syed lab.

References

[1] C. Moulin *et al*., IEEE Trans. Biomed. Eng., 55: 2, 2008. [2] R. Field *et al*., IEEEEMBS Special Topic Conf. on Microtechnologies in Med. and Biol., pp. 297-300, 2006. [3] J. R. Buitenweg *et al*., IEEE Trans. Biomed. Eng., 50:4, pp. 501–509, 2003.

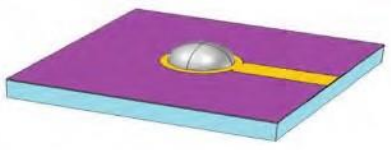

Figure 1: Three-dimensional electrode and soma structure

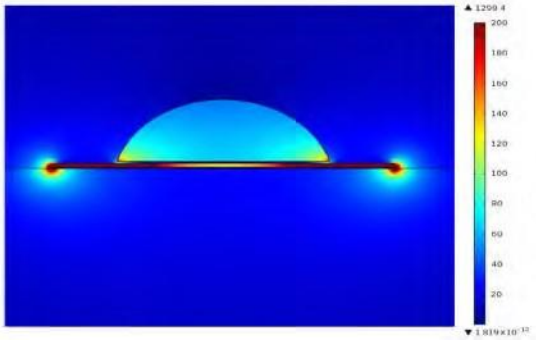

Figure 2: Normal electric field of extracellular voltage stimulation with V=1250mV

On Estimating Penetration Depth of the Patellofemoral Joint

Kamrul Islam[a], Samer M. Adeeb[a], Marwan El-Rich[a] and J.L. Ronsky[b]

[a] Department of Civil and Environmental Engineering, University of Alberta, Edmonton, AB, Canada

[b] Department of Mechanical and Manufacturing Engineering, University of Calgary, Calgary, AB, Canada

Introduction:

Patellofemoral (PF) joint is a complex weight-bearing joint of the human body which is gaining more attention in orthropaedic biomechanics due to the associated different instabilities including patellofemoral pain syndrome (PFPS) [1]. Researchers have developed finite element (FE) models to investigate the PF joint contact mechanics and to quantify the PF joint contact stress patterns [2, 3]. However, considering the complexity of joint modelling using the FE method, we are trying to develop an alternative novel computational approach using 3-D registration technique and linear mapping to investigate the PF joint contact stress using an indirect measure: the depth of penetration of the patellar cartilage surface into the femur cartilage surface. The objective of this research is to quantify the penetration depth of the PF joint in healthy and pathological (PFPS) patients.

Methods:

This study used experimental data from healthy (female, 26±4y, 167.0±7.9cm, 64.4±5.7kg) and pathological (PFPS) subjects (female, 28±8y, 167.0±4.7cm, 59.0±5.5kg). The left knees of all the subjects were scanned using 3.0 Tesla MR imaging at 15, 30, and 45° knee flexion angles. 3-D reconstructed geometry of the patella and femur at different flexion angles were created using MIMICS. Following the digitization, two data sets of 3-D geometry for the patella and femur were imported into the Geomagic Studio 12 as the input for registration. The patella at knee flexion of 15° was chosen as the reference for the registration, whereas the femur is considered as fixed in all cases. Using the registration method, the patella at 15° is linearly transformed from its original (reference) position to a weight-bearing position (30° and 45°) in order to identify the complex interaction between the patella and femur surfaces. In this study, the depth of penetration (PD) was defined as one of the following:

1) PD_1: Cubic root of intersection volume
2) PD_2: Highest thickness of the intersection
3) PD_3: Ratio of the intersection volume to the projected surface area in contact.

Results:

Table 1: PD (mm)

Knee Position	**Healthy Subject**	PD_1	PD_2	PD_3
30°	1	6.97	1.80	1.54
	2	6.08	1.75	1.10
	3	6.50	1.78	1.16
45°	1	7.50	1.95	1.24
	2	6.88	1.94	1.10
	3	7.32	1.85	1.10
Knee Position	**PFPS Subject**	PD_1	PD_2	PD_3
30°	1	5.30	1.80	0.67
	2	7.13	2.80	1.33
	3	6.93	2.60	1.52
45°	1	7.68	2.00	1.36

2	7.59	3.20	1.36
3	8.25	3.04	1.39

Table 1 shows the PD in healthy and PFPS subjects. In healthy subjects, PD_1 and PD_2 show that PD increases with knee flexion angles. PD_3 has an opposite trend. PD is greater for PFPS subjects at 30° and 45° using PD_2 and PD_3. Overall the PD for PFPS subjects is higher compared to the healthy subjects.

Conclusions: PD estimated by using highest thickness of the intersection and the ratio of the intersection volume to the projected surface area in contact is greater in PFPS subjects which may generate higher contact stresses. Future work will focus on correlating PD with the contact area and the difference between the medial and lateral compartments.

References:

1. DeHaven,K.E. *et al.*(1986). *American J. Sports Medicine*, **14**, 218-224.
2. Han, S.K. *et al.* (2005). *J Biomechanics*, **38**, 179-184.
3. Farrokhi, S. *et al.* (2011). *Osteoarthritis and Cartilage*, **19**, 287-294.

Differences in Active Muscular Control Between Dominant and Contralateral Knees in Healthy Individuals

Bishop, E L[1]; Kukulski, D[1]; Mathison, C[1]; Enns-Bray, W[1]; Ronsky, J L
University of Calgary, Calgary, AB

Introduction

The risk of developing osteoarthritis is increased after anterior cruciate ligament (ACL) injury[1]. Altered kinematics and muscle activity patterns have been observed in patients following ACL injury, and may compensate for the unstable knee[2]. Use of the finite helical axis (FHA) method to describe the movement of the knee, combined with characterization of lower limb muscle patterns allows for quantification of *dynamic* knee joint stability[3].

The current study focuses on the muscle patterns in the dominant and contralateral legs of healthy subjects, and relates these patterns to the corresponding FHA outcomes. It was hypothesized that there would be no statistically significant differences in muscle energy between dominant and contralateral legs.

Methods

Six healthy females with intact ACLs were recruited and tested. Subjects performed 2 functional tasks with both legs: a seated leg swing and a single leg squat and rise. Three-dimensional (3D) data for FHA determination was collected from reflective skin markers placed on each lower extremity segment (3 markers /segment) using a calibrated 8-camera (120 Hz) video motion capture system. A 16-channel EMG system recorded muscle activation patterns from the major muscles of the leg. Data was tracked, filtered (10 Hz) and analyzed using in house programs written in Matlab 7.1. Muscle activity patterns were quantified using wavelet analysis, which allows the muscle patterns to be analyzed in terms of intensity and timing[4]. The intensity of each signal was summed across all frequency bands and averaged across each cycle repetition, and again across successful trials. The total energy for each muscle was computed as the area under the intensity curve for each muscle.

A Kolmogorov-Smirnov test (SPSS Statistics 19) was used to confirm normally distributed data. A paired t-test was used to detect differences in muscle energy between dominant and contralateral legs ($p = 0.05$).

Results

Significant differences between dominant and contralateral legs were found for the vastus medialis (VM)

muscle during the squat task (p=0.048); for all other muscles no significant differences were detected (Figure 1).

FHA results indicated a significant difference for the orientation angle during the extension phase of the squat. Therefore, the VM muscle may be responsible for causing a difference in orientation angle between legs during the squat.

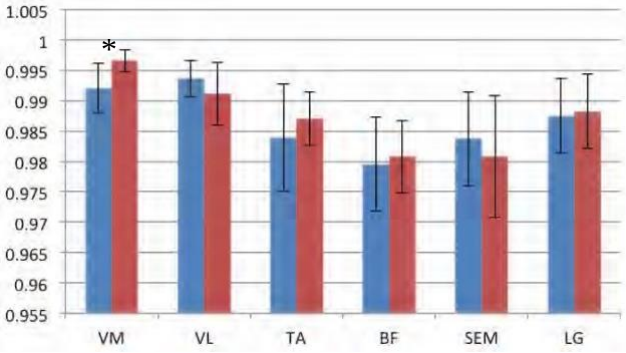

Figure 1: Total muscle energy during a squat task for dominant (blue) and contralateral (red) legs

Conclusions

The study hypothesis was generally supported, detecting no significant differences in muscle energy between limbs, with the exception of the VM during the squat task. Further analysis may reveal correlations between VM energy and FHA orientation angle.

References

1.Andriacchi, T. P. 1990. J Biomech 23 Suppl 1:99105. 2.Snyder-Mackler, L et al. Am. J. Sports. Med. 25 (2), 191–195. 3. Fjeld, et al., 6th Comb. ORS, (2007). 4. von Tscharner V, et al. J Biomech 36 (8) August:1169-1176, 2003.

A Novel Planar Patch-Clamp Microchip For Interrogating Synaptic Activity In Neurons

Collin Luk[1], Christophe Py[3], Marzia Martina[2], Geoff Mealing[2], Naweed Syed[1]

Hotchkiss Brain Institute[1], University of Calgary, Calgary, AB

Institute for Biological Sciences[2], Institute for Microstructural Sciences[3], National Research Council of Canada, Ottawa, ON

Introduction

The patch-clamp technique allows for the interrogation of cellular activity at the ion channel level, a necessity to understanding basic physiology and pathophysiology of all excitable cells—especially brain cells. Conventionally used patch-clamp techniques are technically challenging and are both labor and time intensive. The current development of planar patch-clamp chip technology has allowed for the automation of patch clamp recordings and assaying ion channel activity in excitatory cells. This approach, however, allows the interrogation of suspended cells only, and not the physiologically relevant model achieved through cultured neurons. Thus, our ability to test neurons that are connected in networks—a key model for understanding neurological disorders and subsequent pharmaceutical screening of potential drugs—remains limited. We have now developed a novel form of planar patch clamp technology that allows, for the first time, a low-noise, high-resolution interrogation of cultured *Lymnaea* neurons [1] and the measurement of synaptic activity [2].

Methods

Using a silicon nitride film on a silicon wafer, a 3 to 4 μm aperture mimicking a conventional patch pipette was etched through the film. A larger opening was made on the bottom side of the silicon nitride film and aligned with the top aperture. The silicone wafer was then etched in a 30% KOH solution to produce a truncated pyramid leading to the small aperture generated on the top film. The wafers were subsequently fitted to machined Plexiglass packages with microfluidic channels. When

filled with pipette solution, these subterranean channels allowed for electrical access from an external port to the aperture and subsequently the attached cell membrane (**Fig. 1**). Individual *Lymnaea* neurons were cultured onto the aperture and surrounding area following a previously described protocol [3].

References

1) Py *et al.* 2010. Biotechnol Bioeng, 107, 593-600.

2) Martina *et al.* 2011. J Neural Eng, 8, 034002. 3) Syed *et al.* 1999. Modern techniques in neuroscience research. 361-377.

Figures

A B

Results

A Preliminary Study on Living-Cell Scaffolds for Nerve Tissue Engineering

Ajay Rajaram[1], Mindan Wang[1], David J. Schreyer[1, 2], Daniel X.B. Chen[1, 3]

[2] [3]

Division of Biomedical Engineering, Dept. of Anatomy and Cell Biology, Dept. of Mechanical Engineering

University of Saskatchewan, Saskatoon, SK, S7N 5A2.

We demonstrate that both whole-cell currents and action potentials can be recorded on a planar patch clamp surface over an extended period of time. These neurons form tight seals with the chips as demonstrated by our ability to perfuse a fluorescent dye into the individual neuron through the subterranean channel. Further, our study shows the first ever recordings of synaptic currents as well as synaptic plasticity related changes (**Fig. 2**) in neurons cultured in a network configuration as detected on a planar patch-clamp chip.

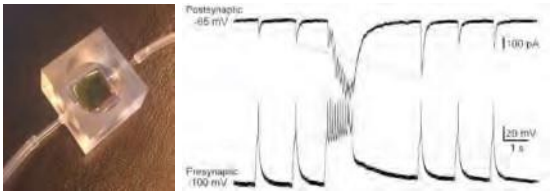

A-Planar patch-clamp chip. B-Synaptic currents in postsynaptic neuron measured by the neurochip while presynaptic neuron is stimulated by a sharp electrode.

Conclusions

The ability to interrogate ion channel activity on a planar patch chip opens up a whole new realm of biomedical research. On the medical science front, the ability to interrogate ion channel activity over an extended period of time has great implications for studying synaptic development and neuronal changes, a keystone of neuroscience that is relatively untouched. On the pharmaceutical development front, this technique will now allow for medium throughput drug screening for ion channel diseases, which had previously been a very slow process.

Introduction

Schwann cells are the principle glial or supportive cells of the peripheral nervous system. Schwann cells incorporated in bioengineered tissue scaffolds are potential tools for improving regenerative repair of damaged peripheral nerves. To promote cellular attachment, alginate may be modified by covalent attachment of peptide sequences [1]. We present a preliminary study on the fabrication of living-cell scaffolds. Our aim was to study the viability and morphology of Schwann cells cultured in a 3D alginate environment modified with the peptide sequences GGGGRGDS and CDPGYIGSR.

Methods

Alginate was modified using carbodiimide chemistry to covalently bind two peptide sequences (RGD and YIGSR) derived from the adhesion protein laminin [2]. A suspension of RSC96 cells (Schwann cell

line) was suspended in unmodified alginate (2.5% w/v), alginate modified with the peptides (2 mg/g of alginate), or alginate mixed with laminin (25 μg/ml). A rapidprototyping dispenser was used to dispense the alginate formulations onto glass cover slips in two layered patterns (see figure). These were immediately cross-linked in 100 mM $CaCl_2$ and maintained in DMEM culture medium containing 3 mM added $CaCl_2$. On the third day, morphological analysis of the cells was performed to assess their circularity and Feret's diameter. Cells in unmodified alginate were stained with DAPI and counted every three days, until day 10, to assess viability.

Results

The circularity of RSC96 cells was highest within unmodified alginate. Cells in both peptide modified alginate formulations had significantly lower mean circularity, due to a large decrease in circularity of a subpopulation. However the peptides did not induce formation of elongated processes. Mean Feret's diameter, a measure of cell size, was also lower in peptide-modified alginate compared to unmodified alginate. The mean cell count in alginate patterns (unmodified) was 100/50 μm^2, assessed after dispensing. The cell count almost doubled by day 3 but then stayed essentially constant until day 10.

Conclusions

Schwann cell can survive during the scaffold fabrication and in alginate for prolonged periods. Although the cellular morphology varied significantly, in the presence of two laminin peptides, the absence of induced Schwann cell processes, suggests an absence of strong adhesion to the matrix necessary for cell migration, and limits the utility of including the peptides. Cell adhesion to scaffolds modified with peptides depends on the presence of specific receptors [3], and it may be necessary to test additional peptide sequences to achieve stronger interaction of Schwann cells with alginate hydrogels. Such living-cell scaffolds are being examined for the repair of damaged peripheral nerves.

References

1. Augst et al., Macromolecular Bioscience, 6(8): 623, 2006.
2. Rowley and Mooney, J Biomed Mater Res, 60: 217, 2002.
3. Yu and Shoichet, Biomaterials, 26: 1507, 2005.

Figures

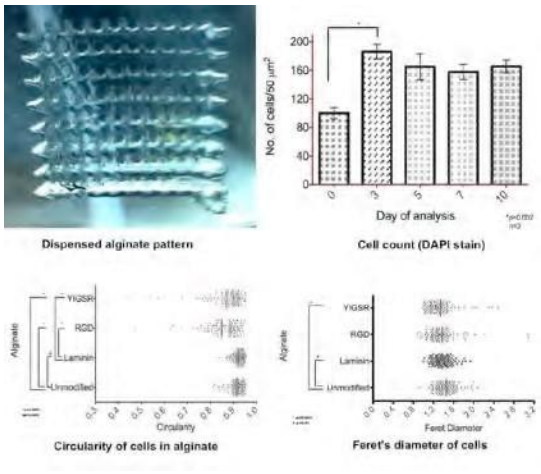

Chondrocyte Deformations under Extreme Tissue Strains

Ryan Madden, Walter Herzog
University of Calgary, Calgary, AB, Canada

Introduction Articular cartilage is essential for proper joint health and function, providing joint surface lubrication and load

transmission across joint surfaces. The cells within articular cartilage – called chondrocytes – are responsible for maintaining the health and integrity of the tissue extracellular matrix (ECM) by synthesizing structural macromolecules. Chondrocyte activity under mechanical loading has been linked to the adaptive/degenerative processes in the joint which lead to osteoarthritis (OA) [1]. The purpose of this study was to investigate the deformation behavior of chondrocytes in their native environment using a novel *in situ* experimental approach [2]. It was hypothesized that chondrocyte deformation would increase with increasing tissue strain up to a threshold value (approximately 25% nominal compressive strain), but then, for increasing tissue strains, cells would not deform further because of limits imposed by the extra- and peri-cellular matrices (PCM).

Methods *Sample preparation*: Intact patellae were extracted from 6 month old New Zealand White rabbits immediately after sacrifice. Fluorescein conjugated dextran (Alexa, excitation: 488 nm) was suspended in DMEM (Dulbecco's Modified Eagle's Medium, Gibco, OR, USA) at a concentration of 3.3 mg/mL (1.1 mM). The tissue samples were incubated in the dextran solution for 4 – 6 hours at 4°C prior to mechanical testing and confocal imaging.

Mechanical Testing: A series of static compressive loads were applied to the tissue samples in the following order: 10%, 20%, 30%, 40%, 60%, and 80%, using a customdesigned indentation system at an average rate of 1%/s. The tissue was given 15 minutes to equilibrate after each compressive load was reached. Confocal image sections were recorded before loading and at each load after the tissue had reached equilibrium. Nominal tissue strain, local ECM strain, and cell deformations were analysed to quantify the overall mechanical response of the cartilage. For cell reconstruction, height was defined as the dimension aligned with the axis of the applied load and width and depth were defined as the two other principle axes in the transverse plane.

Results Local compressive ECM strains increased with increasing applied nominal tissue deformation, from 20.4% to 58.6% at 10% and 80% applied tissue strain, respectively. Chondrocyte volume increased slightly under a 10% nominal tissue strain, then decreased at a 20% strain, followed by a further decrease at 30%, before remaining essentially constant up to 80% applied tissue strain. Cell height compressive strain increased in a similar fashion to the ECM strain. Cell strains in the transverse directions (width and depth) appeared to remain approximately constant for nominal tissue strains ranging from 10% to 60%, however at 80% nominal tissue strain, the transverse cell dimensions increased greatly. At 80% strain, it became difficult to reconstruct the chondrocytes due to a low signal-to-noise ratio and having many cells in close proximity, which may have affected the results.

Conclusions These results provide new insight into the deformation behavior of chondrocytes in their native environment under physiological and extreme nominal tissue strains. The relative stability of cell volumes and the transverse dimensions of the cells under increasing tissue loads is consistent with the hypothesis that the ECM and PCM protect cells from excessive strains in situations of extreme cartilage deformation [3,4].

References

[1] Wong et al., *J Orthop. Res.*, **15**: 189-196, 1997.

[2] Han et al., *Med. Eng. Phys.*, **31**: 1038-1042, 2009.
[3] Guilak et al., *Ann. N.Y. Acad. Sci.*, **1068**: 498-512,
2006.
[4] Han et al., *J. R. Soc. Interface*, **7**: 895-909, 2010.

Joint Damage Correlates with Abnormal Knee Kinematics in Sheep

Jillian E. Beveridge, Bryan J. Heard, Kyla D. Huebner, Nigel G. Shrive, and Cy B. Frank
McCaig Institute for Bone & Joint Health, University of Calgary, 3330 Hospital Drive, NW, Calgary, AB

Introduction

Mechanisms of post-traumatic osteoarthritis remain unknown, although growing evidence suggests that alteration to knee joint motion may be an important factor. We hypothesized that the magnitude of joint damage following various degrees of surgically induced joint instability is correlated with the degree to which knee kinematics are altered in sheep.

Methods

23 sheep were used to test our hypothesis: 11 with combined anterior cruciate and medial collateral ligament transection (ACL/MCLx), 5 with simulated ACL reconstruction (ACL-R), and 7 sham controls (Sham). 3D in vivo kinematics of the right hind knee were recorded prior to injury (Intact) and at 20 weeks post-injury (20w) using a video-based system (accuracy=0.4±0.4mm). For each sheep, kinematics were based on the average stride and were expressed as the change from Intact in 6 degrees of freedom (DOF). The difference from Intact was squared at each point within the gait cycle, summed across the DOFs, and weighted using principal component analysis coefficients calculated previously.

After sacrifice, gross cartilage damage and osteophyte formation were graded at standardized locations spanning the knee. Grades from all locations and both scoring schemes were summed to yield an overall "Composite" score, which was further expressed as the difference from the contralateral knee after assuring that surgery had no effect on the unoperated joint (Kruskal-Wallis test, p=0.57).

Regression analysis was performed to determine the proportion of inter-subject variation in joint change explained by altered kinematics, while the extent to which joint changes and altered kinematics were correlated was assessed using a nonparametric Spearman's test.

Results

Changes in stifle kinematics were subject-specific with ACL/MCLx sheep showing the greatest amount of inter-animal variation, ACL-R sheep showing mild joint and kinematic changes, and Sham knees were relatively unaffected by surgery.

Change in kinematics, expressed as the sum of weighted residuals in Figure 1, was non-linear and correlated with the magnitude of joint damage (Spearman's rho=0.7, p=0.0001). The adjusted non-linear R^2 value of 0.5 suggests that approximately 50% of the variation in joint composite scores were explained by the magnitude of kinematic change. The results further suggest that a threshold exists beyond which other mechanisms, or mechanical mechanisms not captured by the 6 DOF kinematics, may be driving degenerative joint changes in these sheep.

Conclusions

The results support our hypothesis that, within a certain threshold, the degree to which joint kinematics are altered correlates with the amount of joint damage sheep develop. This threshold may provide a target within which joint kinematics must be

restored in order to minimize long-term joint damage.

Figures

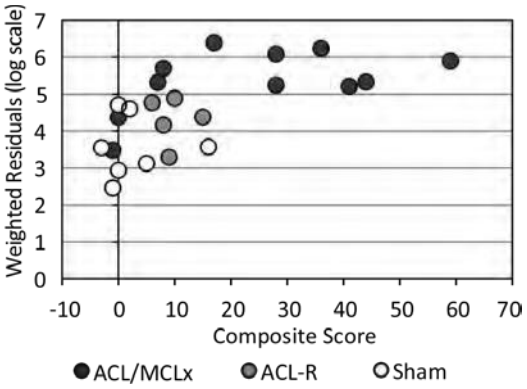

Figure 1. The magnitude of joint damage was nonlinear and strongly correlated with the degree to which kinematics were abnormal (n=23).

Bone properties in elite male alpine skiers

John D. Schipilow[1,2], Anna-Maria Liphardt[1,2], Anja Zieger[1,2,4], Heather M. Macdonald[3], Steven K. Boyd[1,2]

1 Schulich School of Engineering, University of Calgary, Calgary, Alberta, Canada. 2 Roger Jackson Centre for Health and Wellness Research, University of Calgary, Calgary, Alberta, Canada. 3 University of British Columbia, Vancouver, British Columbia, Canada. 4 University of Konstanz, Konstanz, Germany.

Introduction: Athletes participating in sports characterized by specific loading modalities have been shown to present different levels of augmentation to their bone properties[1]. Alpine skiers, who are subjected to extreme loading conditions, have previously displayed enhanced bone structure when compared to controls[2]; however, it remains uncertain to what extent this sporting environment affects bone micro-architecture and estimated bone strength, and if muscle mass can affect these outcomes as well. The purpose of this study was to investigate the relationship between bone microarchitecture, bone strength, and muscle mass, in elite male alpine skiers.

Methods: Subjects included 12 male skiers from the Canadian National Alpine Ski Team along with 10 recreationally active male controls. Bone properties at the dominant distal tibia were measured using high-resolution peripheral quantitative computed tomography (HR-pQCT, Sanco Medical, Brüttisellen, Switzerland). Outcomes included total area (Tt.Ar, mm^2), cortical area (Ct.Ar, mm^2), total bone mineral density (BMD, mg HA/cm^3), bone volume ratio (BV/TV), trabecular thickness (Tb.Th, mm), number (Tb.N, mm^{-1}), separation (Tb.Sp, mm), cortical thickness (Ct.Th, mm), and cortical porosity (Ct.Po, %). Subjects were also scanned using dual energy X-ray absorptiometry (DXA, Discovery A, Hologic) to measure lean mass (g), fat mass (g), and percent body fat. Finite element analysis (FEA) was applied to the HR-pQCT scans to estimate bone strength. Unadjusted data is presented as means ± standard deviations. Means were compared using t-tests, and analysis of covariance (ANCOVA) was used to compare bone outcomes between the two groups adjusting for body mass and height. Adjusted means and 95% confidence intervals (95% CI) are reported. Pearson correlations were used to identify any significant relationships between lean mass and bone outcomes.

Results: Athletes showed a clear difference in the macro-structure of bone, exhibiting a Ct.Ar of 164.1±22.3 mm^2 compared to 137.1±19.6 mm^2 ($p<0.01$). Differences in micro-architecture were also observed, with the average BV/TV for athletes being 0.191±0.021 compared to 0.168±0.023 for controls ($p<0.01$). Consequently, athletes showed higher failure load (9534±1066N versus 7717±1273N, $p<0.01$); however, the

observed difference in ultimate stress was not significant at the $\propto = 0.05$ level.
Subsequent to the application of ANCOVA, Ct.Ar was higher in athletes (162.5 mm^2, 95% CI 148.6 mm^2 - 176.3 mm^2 versus 138.3 mm^2, 95% CI 126.6 mm^2 - 150.1 mm^2, $p<0.05$). Differences in micro-architecture slightly altered, with athletes exhibiting higher BV/TV (0.195, 95% CI 0.181 - 0.210 versus 0.165, 95% CI 0.153 - 0.177, $p<0.01$) and higher Tt.BMD (352.0 mgHA/cm^3, 95% CI 278.0 mgHA/cm^3 - 330.2 mgHA/cm^3 versus 304.2 mgHA/cm^3, 95% CI 321.2 mgHA/cm^3 - 382.9 mgHA/cm^3, $p<0.05$).
Failure load remained higher in the athletes (9208 N, 95% CI 8457 N – 9960 N versus 7963 N, 95% CI 7327 N – 8598 N, $p<0.05$). Strong correlations existed between lean mass and Tt.Ar ($r=.740$, $p<0.01$), Ct.Ar ($r=.544$, $p<0.01$), Ct.Po ($r=.646$, $p<0.01$), and failure load ($r=0.633$, $p<0.01$).

Conclusions: Bone macro- and microarchitecture is augmented in elite male alpine skiers when compared to recreationally active controls. The extreme loading conditions present in competitive alpine skiing are likely to influence bone properties. Additionally, the correlations detected between lean mass and numerous bone outcomes suggest that muscle mass, and perhaps muscle strength, may play a role in the enhancement of bone properties.

References

1. Nikander et al., (2006) Bone 39:886-94
2. Nikander et al., (2008) SJMSS18:145-153

Orthodontic Mini–Implant Orientation Effect in Load Bearing: Finite Element Analysis

M. Najari[a], M. El-Rich[a], S. Adeeb[a], A. Virk[a], B. Taha[b]
[a] Department of Civil and Environmental Engineering, University of Alberta, Edmonton, AB
[b] Orthodontic Dentist, Paris, France

Introduction:

A key aspect of orthodontic treatment is the consideration of anchorage, which is vital to the treatment's success. The term anchorage describes the resistance with which a tooth, a tooth group and/or anatomical unit oppose a movement when they are used to apply a force to move other teeth [1]. The anchorage's effectiveness, i.e., the relationship between the degree of the therapeutic movement desired and the resulting opposing movement, is processdependent on many biological factors, as well as on the orthodontic appliance used. Orthodontic mini-implants have been proven to facilitate temporary stationary anchorage [2]. This study aims to investigate the miniimplant orientation and position effects on the load transferring using Finite Element Analysis (FEA). The stress distribution through the device, bones and periodontal ligament is analyzed.

Methods:

Half of the lower jaw was modeled in this study. The FE model contains the cortical and cancellous bones, the teeth (enamel and root are separated), the periodontal ligament as well as the mini-implant. The mandible geometry was created using Ct-Scans of one adult patient. The mini-implant geometry was provided by IDI System (Manufacturer of orthodontic devices, France). These geometries were then meshed using 3-node shell elements for the cortical bone (2mm of thickness) and 4-node solid element for the cancellous bone, teeth, periodontal ligament and mini-implant. Linear elastic material properties were used in this model (Table 1). The model was completely fixed at the mandibular head and condyle regions and the implant was bounded to the bone between the first and second molar teeth roots perpendicularly

to the roots or at 30° counterclockwise with respect to the horizontal axis. Fifty grams compression combined with 25Nmm clockwise torque was applied on the mini-implant head. Von Mises stress distribution in the mini-implant as well as the jaw was analyzed.

Table 1: FE Model Material Properties

Material	E (MPa)	ν
Cortical [3]	14000	0.3
Cancellous [3]	300	0.3
Ligament [3]	69	0.45
Mini implant [3]	110000	0.35
Enamel [4]	84100	0.3
Root [4]	18600	0.31

Results:

Maximum von Mises Stress in the mini implant was 447 and 283MPa for perpendicular and at 30° position respectively. Inclining the mini implant by 30° decreased von Mises stress from 1.43 to 0.7MPa in cancellous bone and from 17.7 to 9.0MPa in cortical bone. It decreased stress in the teeth roots and enamels from 0.025 to 0.14MPa as well.

Conclusion:

The preliminary results demonstrated the benefit effect of inclining the mini implant at 30° from biomechanical (stress analysis) point of view. It decreases stress in the jaw structures and the mini implant as well. Additional study cases with different mini implant sizes (length, diameter, thread…) under several loading scenarios will be investigated.

References

[1] Eva Stahl1 et al. (2009), Numerical Analyses of Biomechanical Behavior of Various Orthodontic Anchorage Implants. J Orofac Orthop., 2:115-126 [2] Cope JB. Temporary anchorage devices in orthodontics: A paradigm shift (2005) Semin Orthod ;11:3–9.

[3] Motoyoshi M et al. Bone stress for a mini-implant close to the roots of adjacent teeth--3D finite element analysis. Int J Oral Maxillofac Surg 2009 Apr; 38(4):363-368.

[4] Benazzi S, et al. Using occlusal wear information and finite element analysis to investigate stress distributions in human molars. J Anat 2011 Sep; 219(3):259-272.

Poster Presentation Abstracts

Stimulation of neurons using new microelectrode array design

M. Purdy[1], C. Luk[2], A. Lee[2], N. I. Syed[2], C. Dalton[1]

[1] Department of Electrical and Computer Engineering, [2] Department of Anatomy and Cell Biology, University of Calgary, Calgary, Alberta, Canada

Introduction

The brain is a very dynamic, ever-changing network of excitable neurons. A crucial step in understanding synaptogenesis would be to record signals from neurons during synapse formation, and in turn induce similar signals to naïve neurons to decipher the role of activity in synapse formation.

Many conventional stimulation and recording techniques are invasive to the neuron, and may result in cell death following extended stimulation. Microelectrode arrays (MEAs) have been used as a noninvasive means of either stimulating or recording cultured neurons over a long period of time. However, no MEA design exists that allows for both recording and stimulating between the electrode and the cell. Stimulating cells with direct electrode contact results in electroporation to the cell membrane, quickly resulting in cell death [1]. In contrast, testing has shown that direct electrode recordings result in clearer signals [2]. It has been found that the best way to avoid detrimental Faradayic currents present when stimulating with common metal electrodes is to stimulate the cells using capacitive electrodes [3]. The present goal is to optimize a design that can accomplish both stimulation and recording.

Methods

A custom MEA was designed to allow for simultaneous stimulation and recording. Electrodes consist of an inner and outer ring, whose purpose is for recording and stimulation respectively (Figure 1a). Sixteen Cr/Au electrodes were patterned onto a glass slide and then coated with an SU-8 dielectric layer. Through holes in the SU-8 to the inner ring facilitated direct recording while maintaining the ability to induce capacitive stimulation around the outer ring. Stimulation and recording was performed using a Multi-Channel Systems STG4004 stimulus generator. Cell culturing, plating, and creation of conditioned media are described in detail in [2].

Results

Comparisons between the custom MEA design and a commercially available MEA from Multi-Channel Systems has shown that the custom design can facilitate higher frequency of induced action potentials (APs) more closely resembling the frequency of signals sent between neurons *in vivo*. Induced stimulation frequencies have been recorded with sharp electrodes as high as 10Hz (Figure 1b). These recordings are affected by stimulation artifacts which result in rebound APs. However, different stimuli have also been used to stimulate cells, with frequencies as high as 5Hz, with no rebound.

Conclusions

The new MEA design is made using a relatively simple and cheap manufacturing process and allows for both stimulation and recording from neurons. High frequency stimulations were possible using ramp stimulations. Recordings were made using intracellular electrodes to ensure the most accurate recordings were taken. MEA recording electrodes are usable, but need to be refined to achieve better resolution.

References

[1]M. Wang et al. 2010. *AnalBioanal Chem,* 397(8): 3235-3248. [2]J. Samuelson et al. 2011. Thesis, (B.Sc). University of Calgary. [3]P. Fromherz et al. 2007.. *Biophysical Journal*, 92:1096-1111.

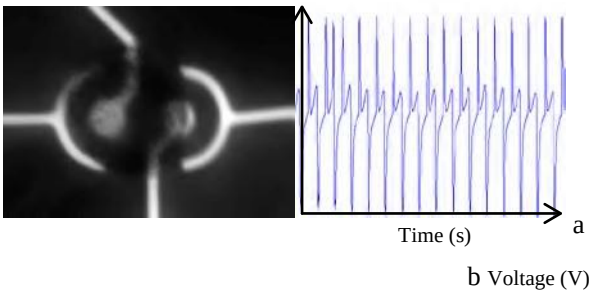

Fig. 1a – Two adjacent stimulating/recording electrodes . Each has an inner direct recording electrode and an outer capacitive stimulating electrode. A cell rests on top of the electrode.

Fig. 1b – 10Hz stimulation using the custom MEA design. Recordings were done with intracellular electrodes.

Mechanical Factors driving Stem Cell Differentiation in Fracture Repair: A Biphasic FE Study of Collagen Scaffolds under Axial Compression and Bending Loads

Saghar Nasr, Neil A. Duncan
Department of Mechanical and Manufacturing Engineering and McCaig Institute for Bone and Joint Health, University of Calgary, Alberta, Canada

Introduction

Physical factors can alter the differentiation of stem cells and the rate of bone fracture healing but the mechanisms remain unknown. Mechanobiology theories have been proposed to explain differentiation of mesenchymal stem cells (MSCs) into mature bone and the role of applied loads, however, the role of mechanical versus biological factors remains elusive. The objective of this study was to predict bone tissue formation in a soft collagenous scaffold seeded with MSCs under different loading regimes. Our long-term objective is to merge the developed finite element (FE) with experimental studies to understand mineralization and gene expression patterns within the scaffolds.

Methods

A biphasic algorithm based on octahedral shear strain and relative fluid velocity was used to predict the tissue differentiation (Lacroix et *al.*, 2000). Based on this theory, MSCs can differentiate into fibrous tissue, cartilage, or bone. The mechanical stimuli were computed using ABAQUS FE software. A user-defined sub-routine was developed to update the material properties per iteration. In each element, gradual change of material properties illustrates the tissue differentiation**.**

Bone tissue formation within a collagen scaffold was simulated for 2 cases (loads were applied over 11 iterations: 2s per iteration): Case 1- Cylindrical collagen scaffold was subjected to confined compression (0.01 MPa). An axisymmetric FE model was created. Case 2- The collagen scaffold was implanted in a fractured tibia model and subjected to axial compression and bending loads (10, 55, 110, 200, 300 N).

Results

Case 1- The fluid flow velocity and strain were reduced over time. This reduction occurred more rapidly in the areas close to the loading region. This indicated that bone formation was promoted in the zones closer to the loading. Case 2- Bone formation was successfully simulated over time with the prediction of fibrous, cartilage and mature bone tissue as well as cell apoptosis (Fig. 2). Cell apoptosis occurred in the mature bone tissue (regions under > 0.15% strain). Bone under both compression and bending loads had higher rates of tissue formation, however, cell apoptosis occurred at a much faster pace and was seen in a larger region.

Conclusions

In both cases, the tissue formation occurred gradually and the scaffold properties became stiffer over time. The predicted strain and fluid velocity were smaller in the stiffer regions. Moreover, it was observed that inappropriate magnitudes or type of loading can cause formation of a heterogeneous tissue or cell apoptosis. Future research will focus on further development of stem cell differentiation algorithms and their validation with gene expression studies and mineralization patterns with micro-CT.

Figures

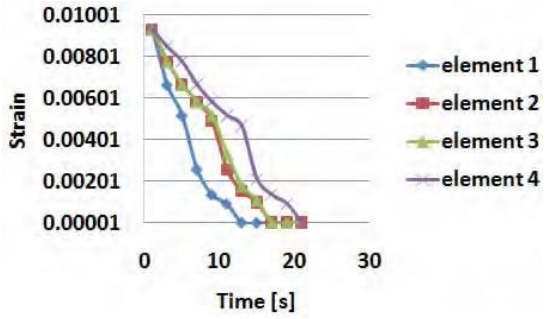

Fig 1. Predicted strain over time for confined compression in 4 sample elements. Element 1 is located at the bottom (close to load), elements 2 and 3: in the middle and element 4 on the top (where fluid exudates). Case-1.

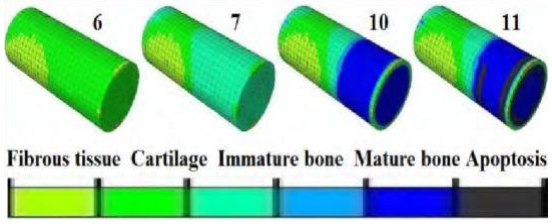

Fig 2. Predicted tissue differentiation under 55 N axial compression in iterations 6, 7, 10 and 11 illustrating bone formation. Case-2.

Bioreactor Seeding of Decellularized Tissue with Endothelial Cells

Khurshid M[1], Turnbull J[2], Narine K[2], Fedak PWM[2], Sen A[1]

1 Pharmaceutical Production Research Facility (PPRF), Schulich School of Engineering, University of Calgary, University Drive NW, Calgary, Alberta, Canada, T2N 1N4

2 Campbell Cardiac Translational Laboratory, Libin Cardiac Institute of Alberta, University of Calgary, Hospital Drive NW, Calgary, Alberta, Canada, T2N 1N4

Introduction

Valvular heart disease can be a lifethreatening condition [1]. Current heart valve replacements have short life spans or necessitate the use of anti-coagulant drugs [2]. Thus, there is a need for biocompatible, durable, mechanically effective heart valve replacements. There is some evidence that Tissue Engineered Heart Valves (TEHVs) can meet this need [3, 4].

Decellularized tissue can be shaped into a heart valve and used as a scaffold to construct a TEHV. Coating decellularized tissue with endothelial cells is important, since an autologous endothelial cell layer would shelter the TEHV from the immune system [5]. Human Umbilical Vein Endothelial Cells (HUVECs) have been shown to be well suited for this purpose, since they can be used in an autologous manner cells in people whose umbilical cells have been stored [6].

This project used confocal microscopy to evaluate the seeding of HUVECs on decellularized animal-derived tissue using a stirred suspension bioreactor. The seeding of decellularized tissue in suspension bioreactors was compared to the static seeding protocol. The cells were grown in Endothelial Cell Growth Medium-2 (EGM2) and stained with DiI dye in order to visualize them on the scaffold.

Methods

Seeding of decellularized porcine tissue was examined in suspension bioreactors and compared to static conditions with respect to the rate of endothelialization. The bioreactor agitation rate and duration of the culture period were examined for their effect on cell seeding. Confocal microscopy was used to evaluate cell density, morphology, penetration and organization on the decellularized tissue. Cell counts were taken to evaluate the viability of the cells in suspension using a haemocytometer and the trypan blue live-dead assay. In addition, a live-dead assay was used to determine the viability of the cells on the scaffold.

Results

Decellularized tissue that was seeded using bioreactor seeding had more cell deposition on the scaffold as compared to static seeding. The surface of the bioreactorseeded decellularized tissue that faced the cells was covered with DiI-stained cells as can be seen in Figure 1.

Conclusions

A spinner flask bioreactor can be used to deposit an endothelial cell layer on the surface of decellularized tissue. Dynamic seeding of decellularized tissue resulted in greater rate of cell deposition on the scaffold than static seeding.

References

[1] Taylor, *et al.*, Springer: New York. 2005. [2] Berry, *et al.*, Annals of biomedical engineering. 2010. [3] Neuenschwander, *et al.*, Transplant immunology. 2004. [4] Filova, *et al.*, Physiological Research. 2009. [5] Sacks, *et al.*, Annual review of biomedical engineering. 2009. [6] Breymann, *et al.*, Stem cell reviews. 2006.

Figures

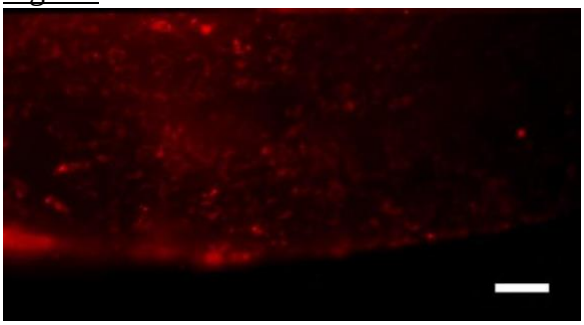

Figure 1: DiI-stained HUVECs (shown with arrows) seeded on decellularized tissue using bioreactor seeding visualized using fluorescent microscopy after 2 days in culture. Scale bar represents 100 µm.

Knee-Ankle-Foot-Orthosis and Sit-to-Stand Biomechanics

Jonathon Schofield, Dr. Samer Adeeb, Dr. Eric Parent: University of Alberta, jsschofi@ualberta.ca

Introduction

Knee-Ankle-Foot-Orthoses (KAFO) brace are designed to assist in standing for patients with limited lower extremity function. The brace holds the knee extended and the ankle in a neutral position, thereby controlling balance and joint alignment. KAFOs have a variety of applications from skeletal complications to muscular weakness and paralysis (1).

Standing is an important physiological function for those using a wheelchair (2). Since a KAFO limits knee and ankle motion, rising from a chair becomes a significant challenge as it requires substantial upper body strength to hoist oneself from seated position. Consequently, many KAFO users are unable to achieve sit-to-stand (STS) independently. Therefore, an assistive STS KAFO mechanism was designed to help compensate for lower extremity weakness by mechanically generating a knee extension moment in the KAFO. The device thereby eliminates the need for a rigidly extended knee during STS and should help reduce the upper extremity moment required to rise from a chair. This study aimed to measure the biomechanical forces in healthy STS movements using motion capture analysis. The analysis of these results guided the design of the prototype.

Methods

The kinematics and kinetic of 10 healthy male STS movements was quantified at the Glenrose's Syncrude Center. Subjects rose 10 times at a comfortable pace from a backless, armless, 19" tall chair with their arms folded across the chest. The 3 dimensional forces associated with STS as well as the discrepancies between the left and right sides were quantified. Motion markers defined 8 segments on each participant. Position was captured through the use of 8 Eagle Digital cameras. With two force plates, dynamic joint moments were calculated over the STS cycle at the ankle, knee and hip. The KAFO design will aim to provide minimally 70% of the healthy knee extensor moment determined from these trials.

Through collaboration with physical therapists and orthotists, four conceptual designs to generate sufficient knee moments were purposed. Eleven pertinent design criteria were identified and weighted according to importance by engineers, and clinicians. The weighted criteria were summed to determine the most successful design; a pulley and cable tensioning system, aimed to mimic quadricep force vectors.

Results

Results in the healthy subjects suggest noticeable asymmetrical force-moment development at each leg joint over the STS cycle. The values of the knee extensor moment provided the necessary peak torque required by the prototype at the knee. The

first-prototype was machined and utilizes a gas compression spring for the tensioning system and series of water-cut brackets. The prototype can be remote triggered by the user to drive knee extension. Kinetic calculations indicate the device can provide peak torque at the knee equivalent to that required by a 90 kg patient during STS.

Conclusions

From the results of both the STS trials and manufacturing of the first assistive STS prototype, it would appear that the design has the potential to be successful in assisting STS in subject prescribed KAFOs. Custom-fit prototypes will be tested on able-bodied and disabled subjects. The timing of torque development in the prototype will be compared to that of healthy STS cycle. Once STS is achieved with the prototype minimizing size and weight will become a priority for future STS KAFO prototypes.

References

1. *KAFO (Knee Ankle Foot Orthosis).* **Sheck and Siress.** s.l. : Sheck & Siress Prosthetics Orthotics Pedorthotic , 2011.
2. *AAOS atlas of orthoses and assistive devices* **Hsu, J., Michael, J. and Fisk, J.** 4, s.l : American Academy

Optical Detection of White Matter Function in Multiple Sclerosis Patients

Jon Jozef Jimenez, Vishal Varshney, Natalia Liapounova, Dr. Brad Goodyear, Dr. Jeff F. Dunn
Hotchkiss Brain Institute, Faculty of Medicine, University of Calgary, Calgary AB T2N-4N1

Introduction

Multiple sclerosis (MS) is a neurodegenerative disease with a high prevalence in Canada[1]. However, there are no quantitative methods which reliably link brain and motor function in MS. We used coherence analysis coupled with nearinfrared (NIR) imaging to determine which areas of the brain are functionally connected and to indirectly assess white matter function, specifically in the corpus callosum. Since the corpus callosum is dominated by white matter, and white matter degeneration is a large component of MS and has roles in temporal coupling[2], we hypothesized that optical detection of coherent frequencies in the cortices would provide a quantitative index of white matter degeneration.

Methods

To observe motor cortex activation, MS patients (n=9) and age-matched controls (n=9) were asked to tap unilaterally for 300 seconds. A NIR system called the Continuous Wave 5 (CW5) was used to detect brain activation. The CW5 uses a set of source-detector pairs to detect light attenuation at 690nm and 830nm which corresponds to deoxy- and oxygenated hemoglobin respectively. The optical data obtained was then processed to derive tomographic maps. Coherence analysis was performed using in-house software to quantify the difference between the MS patients and controls.

Results

Tomographic maps were obtained from the optical data. These maps correspond to differences in light attenuation and showcase brain activation due to blood oxygenation. They can qualitatively distinguish between disease-burdened and control groups (Fig. 1a). They also allow for determination of the area of highest activation (the seed) which can be used to qualitatively and quantitatively assess interhemispheric coherence.

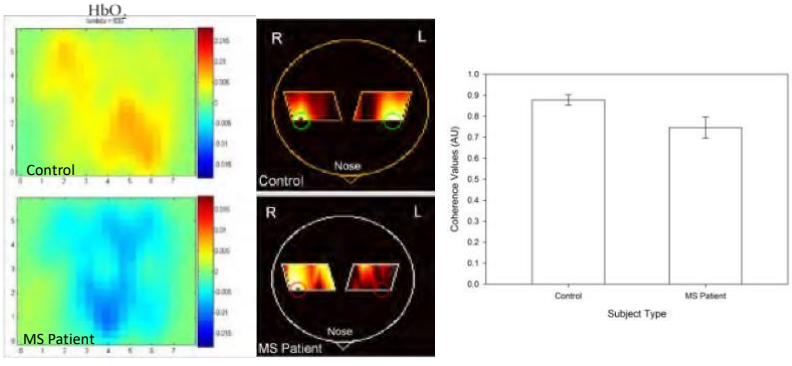

Coherence analysis was performed using the tomographic data. Analysis provides two things: coherence maps and coherence values. Coherence maps qualitatively

showcase functionally connected areas of the brain. Our study found that there are visual differences between the MS group and the control group (Fig. 1b). Coherence analysis also quantifies the degree of interhemispheric interactions due to changes in blood oxygenation. Using coherence values, we were able to quantitatively determine a difference between the MS patients and controls (Fig. 1c).

Conclusions

Coherence analysis coupled with NIR technology is capable of differentiating between control and MS populations. Using our methods, we saw a statistically significant difference between MS patients and controls. The ability to visualize and quantitatively evaluate a patient population can provide physicians a means to select and assess treatment regimes and their patients.

References

1) Ludwin, SK. J Neuropath Exp Neur 2006; 65:305-318

2) Kennerley SW et al. Nat Neurosci 2002; 5:376 – 381

Figures

(a) (b) (c)

Figure 1 – a) Tomographic maps showing brain activation during tapping. Activation indicated by red colors, deactivation by blue. The MS patient shows deactivation when compared to the control. b) Coherence maps showing connected areas of the brain. Paired white regions indicate high interhemispheric coherence. The MS patient does not exhibit this. c) There is a statistically significant difference in coherence between the controls and MS group.

Molecular dynamic simulations for investigating protein adsorption to PEO surfaces

Siriporn Pansri,[1,2] Nick Blinov,[2,*] Larry D Unsworth[1,2,*] [1] Department of Chemical and Materials Engineering, University of Alberta, 9107-116 st, Edmonton, AB, T6G 2M7

[2] National Institute for Nanotechnology, NRC, 11421 Saskatchewan Dr NW, Edmonton, AB, T6G 2M9

Introduction: Protein adsorption at the tissue-material surface is a crucial problem, leading to the failure of devices. To solve this problem, these devices are usually prepared with inert materials such as gold (Au) and then modified with polymers able to resist protein adsorption; a common one being polyethylene (PEO). Recently, it was reported that amount of absorbed proteins on PEO surface could be correlated to its chain density and end-group [1]. However, kinetics and mechanics of protein adsorption, relative to these parameters, are still not well understood because of limitation of experimental devices, ie. not being able to reach atomic level resolution. Therefore, the major objective of this research is to explain adsorption processes of hard protein (lysozyme or LSZ) and soft protein (alpha-lactalbumin or α-LAC) on PEO surfaces (molecular weight of 591 kg/kmol) with different chain densities and with different end-groups (-OH and -OCH_3), using molecular dynamic (MD) simulations.

Method: Firstly, models of 1) LSZ+PEO-OH 2) LSZ+PEO-OCH_3 3) α-LAC+PEO-OH 4) α-LAC+PEO-OCH_3 were constructed. A model of water was used for all systems was SPC/E with cut off value of 20 A^o. According to reference [2] reported that their systems were not able to feel Au under dense pack of different SAM surfaces, hence PEO-thiol surfaces were created with

density of 2 chains/nm^2 without Au surface. However, after finding proper force field for a system consisting of Au, PEO-thiol and a protein, PEO-thiol surfaces will be recreated on a plane (111) of Au. Initial structure of LSZ and α-LAC with ID of 1REX and 1Bo9, respectively from Protein Data Bank were chosen and modified to support AMBER 11. After that, all systems were relaxed by running minimization with steepest decent and conjugate gradient method, followed by setting all systems at temperature of 310.15K, pressure of 1 atm and density of 1 g/cm^3. During simulations, ff03.r1 and GAFF force fields have been used to calculate potential for all atoms in each system. A protein in each system has been then pulled, with an harmonic potential of spring constant 4.32 kcal/molA^2 and pulling velocity of 12 A/ps. Umbrella sampling method will be used to calculate free energy to construct potential of mean force (PMF) for each system.

Results: Table 1 shows energy of each system reduced considerably after minimization runs. Figure 1 shows LSZ pulled down to PEO-OH surface by distance of around 9 A^o from its initial position after running steered MD (SMD) for 0.65ps.

Table 1 Energy of each system.

Models	Energy(kcal/ ol) Before	After
LSZ+PEO-OH	2.3359E10	-4.3813E5
LSZ+PEO-OCH_3	2.3359E10	-4.3786E5
α -LAC+PEO-OH	2.3359E10	-4.4576E5
α -LAC+PEO-OCH_3	2.3359E10	-4.4572E5

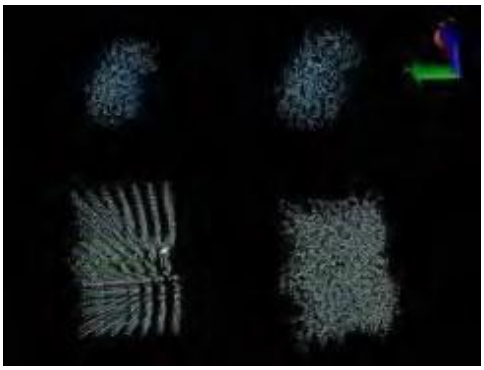

Figure 1 . Initial structure (left) and structure of system 2) at t = 0.65 ps (right) after applying harmonic potential

Conclusions: All systems have to be set to equilibrium firstly before applying harmonic potential for forcing a protein towards the PEO surface. Free energy will be calculated from trajectories obtained using SMD by umbrella sampling method to create PMF for each system. After this stage, thermodynamic properties such as adsorption rate and free energy of adsorption will be calculated. Simulations of systems with lower chain densities of PEO will be run later.

References: [1] L.D. Unsworth et al., Biomaterials 2005;26: 5927-33. [2] R. Godawat et al., PNAS 2009; 36: 15119-24.

Detection of Manganese by MRI Relaxation Ratio Mapping

J. K. McCreary, L. S. Truica and A.R. Cross
Department of Neuroscience, University of Lethbridge

Introduction

Manganese enhanced magnetic resonance imaging (MEMRI) has become a promising technique for functional brain imaging in live animals. By administering a solution of manganese chloride ($MnCl_2$)[1] the contrast obtained is independent of the hemodynamics of the system. Predicting the changes expected in the relaxation parameters allow for image optimization[2]. Most studies using manganese contrast investigate longitudinal relaxation (T_1) changes. However, the relaxation properties of manganese in solution are known to be unique[3] with an unusually large ratio of T_1 to T_2 This paper investigates the addition

of T_2 mapping to the detection of low-level changes of manganese and demonstrates how T_1/T_2 ratio mapping may be used to reveal contrast specific to manganese.

Materials and Methods

Imaging data was acquired using a Magnex (Abingdon, UK) 3T 800 mm bore magnet with a MR6000 console (Surrey UK). The samples were composed of solutions of manganese chloride (0.1, 0.2, 0.05 and 0.045 mM) or copper sulphate (11, 10, 2.2 and 1 mM) The image slice thickness was 2 mm, FOV 128mm (128x128). T_1 data was taken with a saturation transfer spin-echo pulse sequence (10 saturation delays: 50, 200, 400, 500, 700, 900, 1500, 2000, 3000 and 4000 ms) in a random order. T_2 data was taken with a 32 echo spin-echo pulse sequence with a TE of 20 ms. All 8 samples were imaged together in a home built coil (80 mm diameter and 100 mm length). T_1 fitting produced a uniform tip angle map indicating that B_1 field variation was minimized.

Results and Discussion

The study included simulations to assess the sensitivity to small activity changes as well as phantom measurements. The simulations showed that the expected T_1 contrast increases with increased dose; T_2 decrease with increasing dose. Although both displayed changes, simulations are indicating that T_2 is more sensitive then T_1. The ratio (T_1/T_2) maps contain more information and are expected to be more specific to manganese. The phantom study shows that T_1 and T_2 maps do not uniquely distinguish the manganese tubes from the copper tubes. Conversely the ratio map (Figure 1, c) clearly shows 4 brighter tubes, which indeed are the 4 manganese tubes imaged. The samples were specifically selected to have 2 samples (Mn and Cu) with the same T_1 and 2 other with the same T_2. The other 4 samples tested the ability to detect a change in concentration.

The Mn relaxivity is higher for T_2 than T_1 and has more sensitivity to small changes in concentration. The results (see Figure 1) obtained on the phantom tube array relate to literature data[4,5] which indicates that these relaxivities translate to tissue. In manganese imaging of an animal, toxicity as well as the uptake and washout of the contrast agent are issues. Since the washout is slow, in manganese imaging there is time to map the relaxation constants of the tissue of interest.

Conclusions

The results show that T_2 contrast map should as well be considered; also fit parameter and T_1/T_2 ratio maps can become a useful tool in identifying differences in tissues and may be used to reveal contrast specific to manganese.

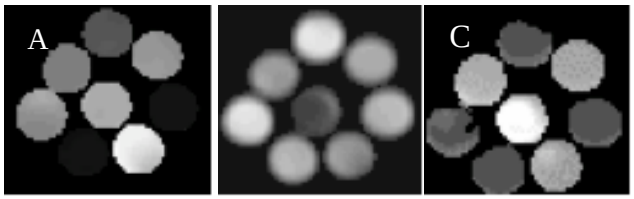

Figure 1. Pixel by pixel of a) T1 map, b) T_2 map and c) Ratio T_1/T_2 map of the 8 sample tubes imaged.

References 1. Y-J. Lin and A.P. Koretsky, Mag. Res. Med. 38, 378-388, (1997). 2. A.C. Silva, J.H. Lee, I. Aoki and A.P. Koretsky, NMR in Biomed, 17, 532-543, (2004). 3. N.J. Bloembergen, J. Chem. Phys, 27, 572, (1957). 4. S. Huang et al. NeuroImage, 46, 589 (2009). 5. C.H. Liu, H.E. D'Arceuil and A.J. de Crespigny, MRM, 51, 978 (2004).

The effect of tube wall stiffness on the speed of waves in tubes

Nygel Shrive, John V. Tyberg, Farzaneh Mazloumfard
Health Research Innovation Centre
Hospital Drive NW HRIC GB37 Lab
Calgary, AB Canada, T2N 4Z6

Introduction

The heart creates pulsatile flow in the arterial and pulmonary circulations. The vessels that make up these systems are distensible, so part of each pulse of blood fills the increasing volume of these vessels, while the remaining blood continues to flow down the vessel. Once the pulse has passed, and the valves from the heart are closed, the vessels contract under their own elasticity, pushing the "stored" blood further down the system. Thus the flow at the beginning of the aorta varies differently over time to flow further down that vessel. Different vessels in each circulatory system appear to have different wall thicknesses and stiffnesses. Further, some organs like the kidney and the brain would appear to function better under continuous blood flow rather than pulsatile flow. Thus we are interested in how wall stiffness of the vessels affects how much blood is "stored" from each pulse and then pushed on down the system, and how the velocity of the wave is affected by wall stiffness. We wish to understand how the body does supply more uniform flow to some organs than to other parts of the circulation.

Methods

The distensibility of seven tubes with different wall stiffness and thickness was measured. Meter lengths of the three tubes most sensitive to pressure change were attached to a pump that delivered a pulsatile waveform resembling aortic flow. The flowrate and pressure changes were measured in the proximal and distal part of each tube. Finally the distensibility of each tube was calculated again.

Results

Comparing distensiblity calculated statically and dynamically in each tube results in a very small difference. This difference can be caused by the non-steady state situation in the first experiment. Also the slope of the graph of wall stiffness versus wave speed shows that the blood speed in the vessels has increased with wall stiffness.

Conclusion

As expected, the more stiff the tube the less the volume that can be stored. In addition the more stiff the tube results in higher wave speed. Of interest are the rate of reduction in storage with wall stiffness, and the rate of change in wave speed. To be more accurate more tubes with a bigger range of wall stiff nesses will be used in the future.

Figures

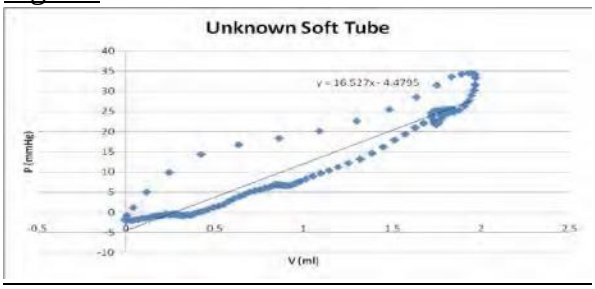

Fig. 1: Pressure versus volume stored in one of tubes

BIOMECHANICAL BASES FOR AN INCLUSIVE ICE SKATING EXERCISE PROGRAM FOR PEOPLE LIVING WITH PARKINSON'S DISEASE: PRELIMINARY CONCEPTS

Patrick Bartoshyk[2], Michael Amatto[2], David Sessford[1], Natalie de Bruin[1], Lesley Brown[1], Jon Doan[2]
[1] [2] Balance Research Laboratory, Engineering and Human Performance Laboratory, University of Lethbridge

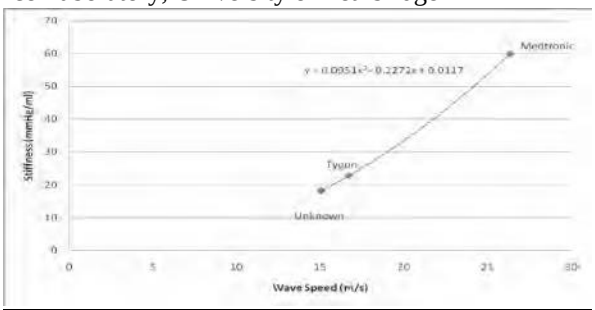

Fig 2: wall stiffness versus wave speed for three different tubes

Introduction

Exercise-based neurorehabilitation for Parkinson's disease (PD) patients has shown promise. One limitation to current exercise therapies is the exclusion of both early and advanced PD patients. Ice skating may provide an alternative - skating exercise can confer physiological benefits, and it provides direct skills transfer to gait and balance. More importantly, ice skating shows a remarkable perseveration amongst some PD patients, and it could be modified to effectively challenge a wide range of PD patients. The purpose of this study was to examine biomechanical responses to real ice skating and ice skating visual imagery amongst PD patients.

Methods

Experiment 1. Five medicated PD patients (51.2 ± 12 years old) had surface electromyography (sEMG) sensors attached superior to *tibialis anterior* (TA), *gastrocnemius* (G), *quadricep* (Q) and *hamstring* (H) of their dominant leg. Each patient completed 10 trials (each 12 m in length) of ice skating and regular terrain gait, with sEMG data collected during the central 8 meters of each trial. Data were sampled at 1000 Hz. Peak Mean Absolute Value (PMAV) was determined for each sEMG channel in each trial, then averaged across like trials for each subject. The dependent variable was the ratio of activation in each muscle during skating, relative to walking ($PMAV_{SKATE}/PMAV_{WALK}$). Sagittal video was also captured and analysed.

Case study 1. One PD patient from Exp. 1 (38 y.o.) and one age- and gender-matched control completed four repetitions of the Sensory Organization Test (SOT) on a customized dynamic posturography unit. SOTs were modified so that visual information for the participant was either static, 1st person walking, 1st person skating, or 1st person skating fast. Visual conditions were randomly presented to participants, with each participant completing two trials of each 'eyes open' SOT type (4 of 6 SOTs) under each visual information condition.

Results

Experiment 1. Zero of 5 patients fell during skating sessions. Peak muscular activity was significantly greater during skating than regular terrain gait. Stride length and arm swing were also increased during skating. *Case study 1.* Ice skating visual imagery influenced balance of the PD participant in static and dynamic postural tests. Of note, 1st person skating visual information provided the greatest postural control (smallest centre of pressure excursion area), and sway area was equal between participants in this visual condition [Fig. 1].

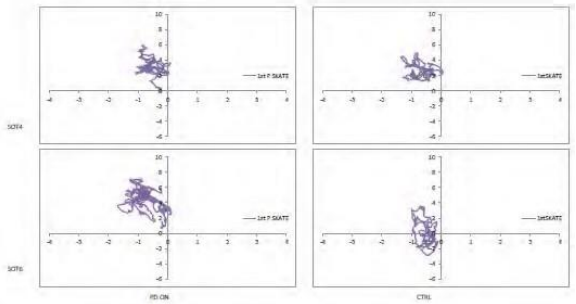

Figure 1. Average CoP sway patterns for dynamic postural tests with 1st person ice skating visual imagery. PD patient trials in left column, CTRL participant trials in right column.

Conclusions

Early, mild, and moderate Parkinson's disease patients were capable of safe and effective ice skating. This activity challenged the neuromuscular system, and that challenge, along with physiological loading and skill transfer, makes ice skating a feasible exercise therapy for PD patients. For more affected PD patients, visual information from 1st person ice skating may contain appropriate visuomotor cues to activate increased neuromuscular

response. Real ice skating and ice skating visual imagery could be useful components in exercise therapy amongst PD patients.

Using the OpenCL (Open Computing Language) framework for medical image registration

Author: Sachitsing Dwarkan || Supervisors: Dr. Ross Mitchell, Dr. Steven Boyd
Address: HMRB372 – 3330 Hospital Drive NW, Calgary, AB, T2N 4N1

Introduction

Medical image registration, a widely acknowledged computationally expensive method, is used to combine multiple sets of patient image data. It has been previously demonstrated that acceleration of image registration can be achieved by parallelization of computations on graphics processing units (GPUs) using OpenGL (Open Graphics Library). My project demonstrates the possibility of using OpenCL for image registration. OpenCL is a generalized computation framework that is supported by various types of recent lowcost processors.

Methods

The software codebase initially developed by S. Chan[1] and D. Adler[2] was used as a starting point for this project. The modules suitable for implementation in OpenCL were identified – transformation, resampling and similarity verification.

Due to memory management on the GPU being one of the major limiting factors to fast registration, the identified modules were initially implemented using 3 different data access methods. The method resulting in the shortest registration time was then chosen for the implementation of other types of similarity metric calculation.

The normalized mutual information metric was used to register RIRE (Retrospective Image Registration Evaluation) image datasets for comparison to other published methods. The Apple Mac operating system was used for development and testing.

Results

The fastest data access method used 3D image read-write functions on the GPU. RIRE 3D image datasets are used to determine accuracy of registration of CT or PET images to MR images. In the case of CT image registration, a mean error of approximately 2mm was achieved. This is equivalent to approximately 1.5 pixels error in the planar image slice orientation and approximately 0.5 pixels error in depth of the 3D volumetric image. For PET images, the approximate mean error was 6mm (4 pixels error in a planar slice orientation, 1.5 pixels error in depth of the volume). In more than 90% of the cases, full image registration, including time to setup GPU memory and display images, was less than 10 secs. The combined time spent performing computations within the transformation, resampling and similarity metric calculation modules was less than 7 secs.

Conclusions

In medical practice, since most medical images are analyzed visually, mean realignment errors of 1-2 pixels are negligible for patient diagnosis. Combined with the short computation time of less than 10secs, such GPU-accelerated image analysis methods could allow for huge volumes of patient data to be processed in near real-time at relatively low-cost with the use of general consumer-level graphics processors.

References

[1] S. Chan, “Three-Dimensional Medical Image Registration on Modern Graphics Processors”, M.S. Thesis, University of Calgary, Calgary, AB, Canada, 2007.

[2] D. Adler, "Accelerated Medical Image Registration using the Graphics Processing Unit", M.S. Thesis, University of Calgary, Calgary, AB, Canada, 2011.

Figures

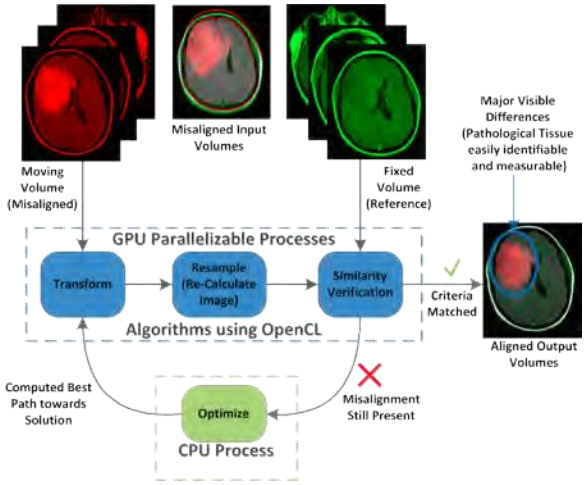

T-type Calcium channel Causes Calcium-Induced Calcium-Release In Smooth Muscle Cells

Kamran Bigdely-Shamloo, Edward J. Vigmond and Donald G.Welsh
Department of Electrical & Computer Engineering and Department of Physiology & Pharmacology
– 2500 UNIVERSITY DR NW – CALGARY AB T2N 1N4

Introduction

The cytosolic concentration of free Ca in smooth muscle ([Ca]i) is a key determinant of vascular tone and local blood flow. Local and global changes in [Ca]i are usually perceived as Ca sparks and Ca waves respectively. The mechanisms of emergence and propagation of these sparks and waves play important roles in understanding the constriction of smooth muscle cells (SMCs). We hypothesize that T-type Ca channels (TCC) exist in SMCs and are localized to cause calcium induced calcium release (CICR), and are required for initiating Ca sparks.

Methods

In this work, we have made a mathematical model of SMC Ca handling which included a detailed subspace, Ca uptake and release from the sarcoplasmic reticulum, cytosolic balance of Ca, and sarcolemma electrophysiology. TCCs were localized in the caveolae in order to be in apposition with ryanodin receptors. The model was stimulated by a depolarizing voltage step to investigate the $[Ca]_i$ both in relaxation and constriction states. Model parameters were fit using a parallel genetic algorithm for multi-objective optimization.

Results

Introducing T-type Ca channels induced not only CICR beginning around -60mV but also sustained [Ca]i oscillations [Figure 1]. Moreover, depolarizing cell to higher potential did not have significant increase in frequency of oscillations suggesting that TCCs act as a two-state switch which can turn on or off the oscillations. Finally depolarization above -18 mV resulted in a single spike.

Conclusions

T-type Ca currents have a significant effect on smooth muscle cell behavior which warrants further investigation. In this study we showed that TCC works as a switch for turning of and on the oscillations. Thus, including their behavior will allow us to more closely simulate experimentally observed phenomena. Moreover, the model can be used as a basis for building multicellular biophysical models that will explore microcirculatory function in health and disease.

References

[1] Kuo IY et al., J Cereb Blood Flow Metab (vol 30, 1226-1239, June 2010)
[2] Nikolaos M. Tsoukias et al., J of Theo. Bio.(vol 253, issue 2, July 2008, 238-260)
[3] Oleg V. Aslanidi et al., Bio. J (volume 98 issue 11 pp.2420 - 2431)

Figures

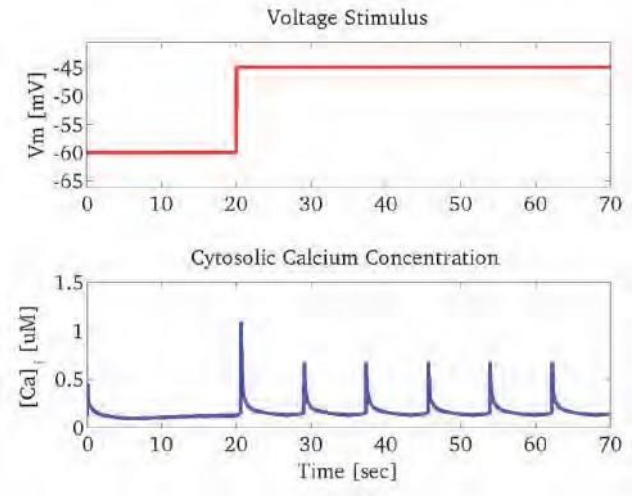

Figure 1. Voltage stimulation and [Ca]i

A METHOD TO MEASURE RESIDUAL STRAINS IN THE MOUSE AORTA

Simone Rivolo, Samaneh Nobakht, Chiara Bellini, Elena S. Di Martino
Department of Civil Engineering and Centre for Bioengineering Research and Education
University of Calgary - 2500 University Drive NW, Calgary, Alberta

Introduction

Mechanical stimuli may create imbalances in the tight structure/function relationship characteristic of blood vessels and promote a growth and remodeling cascade intended to maintain preferred form and function. This process is particularly complex for the aortic wall, which is a collection of independently growing elements (Cardamone, *Biomech Model Mechanobiol*, 2009). Material continuity requires all constituent-level deformations associated with remodeling to be compatible with the configuration assumed by the whole artery. This kinematic constraint imposes the presence of residual strains, which are traditionally computed from the opening angle (OA) assumed by an aortic ring after a radial cut (Chuong and Fung, *J Biomech Engg*, 1986). Goal of this work was to develop a semi-automatic procedure to measure the OA from large stacks of microscopy images of mouse aortic rings. The corresponding residual strains will be used to correlate the macroscopic manifestations of growth and remodeling with their microscopic origin.

Methods

The aorta was excised from n=2 wild-type (WT) mice and n=2 mgR/mgR mice (KO, animal model of Marfan syndrome expressing fibrillin-1 at 15 to 25% of normal levels). Rings with an approximate height of 0.5mm were obtained from the vessels. Each ring was radially cut to release residual strains. Images of the rings before and after the radial cut were taken with a dissection microscope at 40x. The Image Processing Toolbox offered in MATLAB (r2010a) was used to improve the general image quality and remove perivascular tissue and fat from the pictures. A custom routine was written to detect the boundaries of each ring in both the close and open configurations. Each image was first converted to binary (black and white) and the central pixel selected as a reference point (pivot). The intensity associated with pixels located at increasing distance from the pivot was then checked.

Whenever a change in the intensity with respect to the pivot point was detected, the corresponding pixel was assigned to the internal boundary. All points belonging to the internal boundary were obtained by moving the search line clockwise. Once detected, the internal boundary was removed from the image, so that the same technique could be utilized to find the external boundary. A nonlinear least-square regression was used to fit the point clouds expressing the boundaries to circumferences. Estimates of internal and external radii and a measure the OA were obtained from the procedure.

Results

An average R^2 of 0.96 resulted from the nonlinear regressions, supporting the assumption of circularity for the aortic cross-section. Average OAs (in degrees) in the WT mouse were found to be 54.15 for the ascending aortic arch, 66.06 for the descending aortic arch, 63.03 for the thoracic aorta and 113.35 for the abdominal aorta. Under-expression of the protein fibrillin-1 induced a decrease in the OA for both the thoracic and the abdominal aorta, with average OAs (in degrees) of 52.33 and 39.65, respectively.

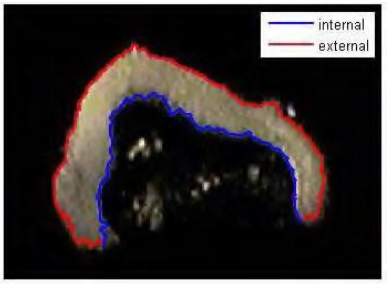

Figure 1: Internal and external boundaries detected by the custom routine

Conclusions

The MATLAB routine described herein proved to be a fast and reliable tool for the semi-automatic processing of microscopy images addressed to the measurement of the OA. Application of the code to stacks of images from OA experiments on WT and KO mice revealed a decrease in the OA in an animal model of Marfan syndrome that is worth further investigation.

Poromechanical Finite Element Study of the Articular Cartilage in Partial Meniscectomy Knee Joints

Kazemi, M; Li, LP

Department of Mechanical and Manufacturing Engineering, University of Calgary, Alberta, Canada

Introduction

Fluid pressurization in cartilage and menisci has been ignored in published threedimensional (3D) finite element (FE) studies of the meniscectomy knees. Consequently, these models can only predict the instantaneous or equilibrium response of the knee tissues. The time-dependent response of the knee resulted from fluid pressurization cannot be captured using these models. The objective of this study was to investigate the time-dependent response of the cartilage following partial meniscectomy using a 3D fibril-reinforced FE model of the knee joint. In particular, changes in fluid pressurization in femoral cartilage after meniscectomy were studied.

Methods

The knee geometry was obtained using magnetic resonance imaging (MRI) of a male's right leg. The model included femur, tibia, fibula, cartilages, menisci and four major ligaments: ACL, PCL, LCL and MCL. To consider the role of collagen fibres, fibril-reinforced modeling was used for the solid matrix of cartilages, menisci and ligaments. A user-defined FORTRAN subroutine was used for the fibres material properties.

The stress relaxation protocol with displacement of 0.2 mm was considered for this study. Six contact pairs were considered with 3 on the medial side and 3 on the lateral side: femoral cartilage-menisci, femoral cartilage-tibial cartilages, and menisci-tibial cartilages. To simulate the partial meniscectomies, six different cases were considered: posterior medial (PM), central medial (CM), extended medial (EM), anterior lateral (AL), central lateral (CL) and extended lateral (EL) meniscectomies.

Results

For the case of the intact knee, a high fluid pressure center was observed in each condyle with slightly higher pressure in the medial condyle (Fig. 1a, t = 10s). The fluid pressure decreased monotonically with relaxation. The maximum pressure decreased by 18% and 93% at 10 and 4000s, respectively, as compared to that at 1s. In all cases of meniscectomy, the fluid pressure level increased as compared to the intact knee. For instance, in the case of extended lateral meniscectomy (EL), the maximum fluid pressure was approximately 49% and 184% higher than that in the intact joint at t= 10s and 4000s, respectively. In contrast to the intact knee, significantly higher pressure was observed in the lateral condyle, corresponding to the site of meniscus resection (Fig. 1b, EL case).

Conclusions

The key findings of this study about the changes in fluid pressurization in cartilage after meniscectomy were: 1) significant increase in the fluid pressure, 2) substantial alterations in fluid pressure distribution within a condyle and between the lateral and medial condyles, and 3) direct correlation between the increase in meniscus resection and the increase in the pressure level. In all meniscectomy cases, the maximum fluid pressure occurred in the condyle that was in contact with the site of meniscus resection. As a result, lateral meniscectomies shifted the maximum pressure from the medial to the lateral condyle, considering the maximum

pressure occurred in the medial condyle for the intact knee.

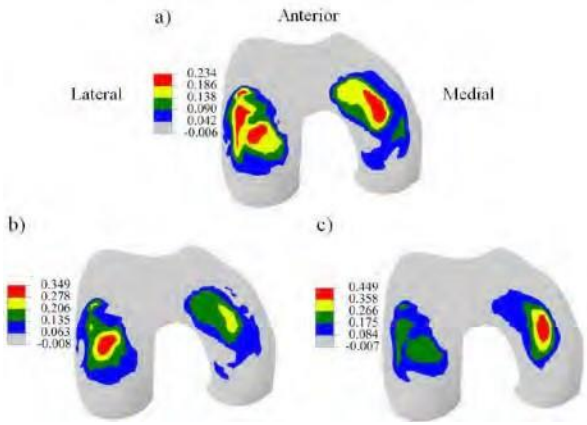

Fig. 1 Fluid pressure (MPa) in femoral cartilage at *t*=10s. a) Intact knee, b) Extended Lateral meniscectomy, c) Extended Medial meniscectomy.

A new methodology using Principal Component Analysis to quantify bilateral asymmetry of human gait

Stefan Hoerzer[a], Christian Maurer[a], Peter Federolf[a, b], Vincent von Tscharner[a], Benno M. Nigg[a]

[a] Human Performance Lab, University of Calgary, 2500 University Dr NW, Calgary, AB, Canada, T2N 1N4

[b] Norwegian School of Sport Sciences, P.O. Box 4014 Ulleval Stadion, 0806 Oslo, Norway

Introduction:

Asymmetry of human gait has been investigated for many years using methods that analyze discrete variables [1, 2]. The discrete variable approach may miss important information due to (a) the preselection of discrete variables, and (b) the lack of consideration of the functional dependency of these variables. Currently, new methods are available that include all measured data in the data analysis. It is speculated that this new method provides superior results than the conventional discrete variable approach. The aim of this study was to introduce a new holistic methodology based on the principal component analysis (PCA) in order (a) to define an index for gait asymmetry which considers the functional dependency of the measured variables, and (b) to compare the influence of different conditions (barefoot and shod) on this asymmetry.

Methods:

Sixteen able-bodied subjects (25.5 ± 4.2 years) were instructed to perform 5 barefoot and 5 shod running trials (4 ± 0.6 ms^{-1}) over a force platform for the right and the left leg. Kinematic and kinetic variables for the hip, knee and ankle were recorded and computed over the stance phase. The mean curve of each leg for each condition and subject was vectorized and subsequently analyzed using PCA. The vector of each subject was then projected onto the first 10 (i = 1…10) principal components (PCs). Equation 1 provides the difference vector (D) between the left and the right leg in a 10-dimensional subspace:

$$_i = \int \langle \ 1( ) \quad r( ) \mid _i \rangle \qquad (1)$$

where $xl_s(t)$ represents the left leg and $xr_s(t)$ the right leg of the subjects (s). The length of this difference vector was defined as the asymmetry index ASI (Equation 2).

$$= \sqrt{\sum_{i=1}^{10} (\ _i)^2} \qquad (2)$$

The average ASI of the two conditions was calculated and the significance was tested using a paired sample t-test (p=.05).

Results:

The able-bodied subjects showed an average ASI of 7.0 (± 1.6) for the barefoot condition. While running with shoes, the ASI was reduced by about 30 % to 4.8 (± 1.3). An individual comparison revealed that 14 out of the 16 subjects showed a lower ASI while running with shoes. The ASI between barefoot and shoes showed a significant difference with p≤.001 (Figure 1).

Conclusions:

The new PCA-based ASI represents a tool to quantify significant differences between

barefoot and shod running. Future studies analyzing the loadings of the PCs can investigate the importance and the influence of different kinematic and kinetic variables on the asymmetry of human gait.

References:

[1] Herzog W, Nigg BM, Read LJ and Olsson E. (1989). Asymmetries in ground reaction force patterns in normal human gait. Med Sci Sports Exerc. 21(1):110-4.

[2] Zifchock RA, Davis I, Higginson J and Royer T. (2008). The symmetry angle: A novel, robust method of quantifying asymmetry. Gait Posture. 27(4):622-7.

Figures:

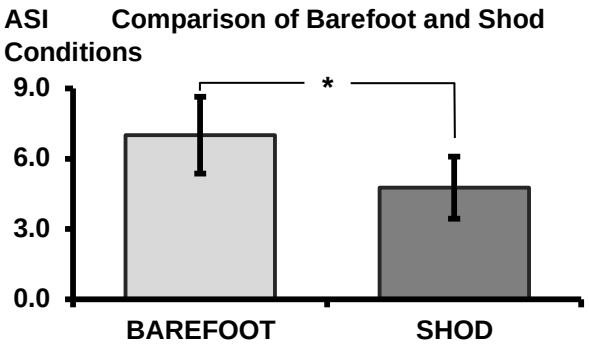

Figure 1: Comparison of barefoot and shod conditions based on the asymmetry index (ASI).

Characterization of Cartilage Boundary Lubricant Composition and Function of Ovine Synovial Fluid Following Knee Surgery

[1] [1] [1] [1] [1] [1]
Barton, K I; Ludwig, T E; Achari, Y; Shrive, N G; Frank, C B; Schmidt, T A
[1] University of Calgary, Calgary, AB, Canada

Introduction: Proteoglycan 4 (PRG4) is a glycoprotein present in synovial fluid (SF) that contributes to the boundary lubrication of cartilage[1] and maintenance of the joint[2]. PRG4 also acts synergistically with hyaluronan (HA) acting as cartilage boundary lubricants[3]. Acute injury to the anterior cruciate ligament (ACL) shows a decrease in PRG4[4] and HA[5] concentration in human SF and ovine SF (oSF), respectively, and a decrease in cartilage lubricating ability in human SF[6]. Alterations in SF lubricant composition and function have been shown to return to normal within a year[4]. Altered gait mechanics and degradation of the cartilage has been observed 20 weeks post surgery[7]; however, potential alterations in SF lubricant composition and function remain to be determined in an post-knee injury ovine model.

Methods: In previous studies[7&8], 15 mature 3year-old female Suffolk-cross sheep were subject to one of three surgical procedures: surgical sham (SHAM), ACL/medial collateral ligament (ACL/MCL) transection, or lateral meniscectomy (MEN), with the contralateral left joint serving as the non-operative control (CTRL). PRG4 and HA concentration in oSF and CTRL SF were measured by sandwich enzyme linked immunosorbent assay (ELISA)[9]. HA molecular weight (MW) distribution was determined by agarose gel electrophoresis[10]. A previously described *in vitro* cartilage-cartilage friction test using bovine cartilage under boundary lubricating conditions[3] was used to assess oSF. The following sequential test sequence was used (n=4 for each oSF surgical group): phosphate buffered saline (PBS), operated oSF, CTRL oSF, bovine SF (bSF). Static, μstatic,Neq, and kinetic, <μkinetic,Neq>, friction coefficients were calculated.

Results: PRG4 concentration in operated oSF was not different than respective CTRL SF (SHAM p=0.10, ACL/MCL p=0.20, MEN p=0.27) (**Table 1**), with values ranging from 404-566 μg/mL. HA concentration in operated oSF was not different than respective CTRL SF (SHAM p=0.86, ACL/MCL p=0.69, MEN p=0.90) (**Table 1**), with values ranging from

Treatment of Deep Tissue Injury Using Intermittent Electrical Stimulation

Elizabeth Twist, Su Ling Chong, Yahya Kinyogo, Vivian K. Mushahwar
Department of Cell Biology and Center for Neuroscience, Faculty of Medicine & Dentistry, University of Alberta
AHFMR Interdisciplinary Team in Smart Neural Prostheses

0.82-1.02 mg/mL. HA MW distribution within operated oSF was also similar to respective CTRL SF in all experimental groups, with the majority of the HA being >1.1MDa. Lubricants and pre-spin duration (Tps) modulated friction. $\mu_{static,Neq}$ increased with increasing Tps for all lubricants, with an interaction (all $p<0.001$). Values of $\mu_{static,Neq}$ were greatest in PBS, while operated oSF, respective CTRL oSF, and bSF were all similar and lower than PBS.
$<\mu_{kinetic,Neq}>$ also varied with lubricant, only slightly with Tps, with an interaction (all $p<0.001$). $<\mu_{kinetic,Neq}>$ at Tps=1.2s in PBS was significantly higher than all experimental groups, both operated and CTRL oSF, and bSF in all cases (all $p<0.05$) (**Fig. 1**). $<\mu_{kinetic,Neq}>$ at Tps=1.2s in operated oSF were similar to CTRL oSF and bSF in all experimental groups. In all cases, CTRL oSF was also not different than bSF ($p=0.85$-1.0).

Conclusions: Normal HA and PRG4 composition and cartilage boundary lubricating function are present in oSF 20 weeks post meniscectomy and ACL/MCL transection.
These data are consistent with previous studies demonstrating that while SF lubricant composition can be significantly altered immediately after an acute injury[4&5], levels can return to normal at later stages[4], though still potentially at a 'semi-acute' stage. The specific time course of such alterations, if any, remains to be fully elucidated in these models.

References: [1]Schmidt+ *BBA* '09, [2]Coles+ *A&R* '10, [3]Schmidt+ *A&R* '07, [4]Elsaid+ *A&R* '08, [5]Pitsillides+ *Rheum* '99, [6]Jay+ *JR* '04, [7]Beveridge+ *JOR* '11, [8]Tapper+ *JOR* '08, [9]Hill+ *Trans ORS* '10, [10]Lee+ *Anal Biochem* '94.

oSF	SHAM		ACL/MCL		MEN	
	Operated	CTRL	Operated	CTRL	Operated	CTRL
[HA] (mg/mL)	0.82±0.11	0.86±0.18	0.83±0.29	0.95±0.05	1.02±0.08	0.97±0.09
[PRG4] (μg/mL)	409±67	566±50	452±19	527±49	404±75	530±67

Table 1: HA and PRG4 concentration in SHAM, ACL/MCL transection, and MEN oSF, and respective non-operated (CTRL) oSF.

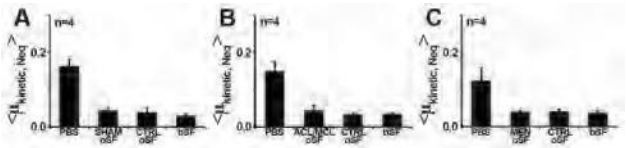

Figure 1: Kinetic $<\mu_{kinetic,Neq}>$ at Tps=1.2s friction coefficients in SHAM (**A**), ACL/MCL transection (**B**), and MEN (**C**) oSF, respective nonoperated (CTRL) oSF, and bSF.

Introduction

Suspected Deep Tissue Injury (DTI) is a pressure ulcer that originates at deep bone-muscle interfaces and progresses undetected towards the skin. Sustained pressure is the primary factor leading to the formation of DTI. Groups at high risk of developing DTI are people with reduced mobility including people with spinal cord injury, elderly, and patients in intensive care or in long- term homes. The annual costs of treating pressure ulcers are approximately 11 billion in the USA and ~60,000 lives are lost to pressure ulcer complications. We found that Intermittent Electrical Stimulation (IES) could be used as an effective method for the prevention of DTI. IES produces periodical contractions in muscles compressed by bony prominences, allowing the re-distribution of pressure and increases in muscle oxygenation. Electrical stimulation has been used to treat many wounds including pressure ulcers that have already reached the skin. The goal of this study was to determine if IES could be effective in reversing DTIs prior to their development into open wounds. We hypothesized that IES will decrease the extent and intensity of edema associated with DTI, increase oxygenation and increase the rate of healing.

Methods

Experiments were conducted in adult rats that had a severe DTI induced in the triceps surae muscles 24 hours earlier. IES was applied

through a cuff electrode placed around the tibial nerve. IES treatment was applied every 10 minutes for 10 seconds and was administered for either 2 or 4 hours. The control rats were under anesthetic for the equivalent amount of time but received no IES. The rats then recovered in their cages. The following day, magnetic resonance imaging (MRI) was conducted in order to assess the extent of remaining edema. The animals were subsequently euthanized and tissue samples were collected.

Results and Discussion

The 2 hour IES treatment showed a strong trend towards decreasing the extent of edema, suggesting decreased muscle damage. Unexpectedly, the 4 hours of IES caused an increased the extent of edema. This increase could on the one hand be caused by the increased surgery time and increased stress response. On the other hand, it may not signify increased injury; rather, it may be the result of dispersal of the DTIinduced edema within the muscle which would lead to faster healing. Nonetheless, histology is needed to better explain this observation. Interestingly, there appeared to be a difference in the extent of the edema between the control animals (not receiving IES) in the 2 and 4 hour groups, and that needs to be further investigated. This preliminary study demonstrated many important trends in the effect of IES treatment on DTI. There appears to be an optimal time range for the application of treatment as the 2 hour period seemed to decrease edema while the 4 hour period increased it. The effect of IES treatment may not be as pronounced as in a spinal cord injury model as the rats in this experiment were able to move voluntarily and contract their own muscles, which on its own may be adequate to assist in the healing process. The findings suggest that IES may be an effective method for the reversal of DTIs prior to their progression towards the skin and development into open wounds.

Tissue Status Monitoring using Near Infra-red Spectroscopy

Martin Ferguson-Pell and Malinda Guo
Faculty of Rehabilitation Medicine, University of Alberta, Edmonton, Alberta, Canada, T6G2C6
AHFMR Smart Neural Prosthesis Team Grant

Acknowledgements:

The work was funded by AHFMR. Mr. Peter Seres acquired all MR scans. Analysis code was provided by Mr. Leandro Solis.

Introduction

Early detection of deep tissue injury, such as that associated with the onset of pressure ulcers, has been an elusive goal. Although fMRI offers interesting opportunities to detect subtle changes in tissue physiology associated with deep tissue injury (Solis et al, 2007), fMRI is not practical for routine clinical screening of tissue status. In this study a hand-held tissue status monitor (TSM) has been developed employing principles that have been used for brain imaging, particularly for infants. Near infrared light (NIR) is selectively absorbed at specific wavelengths by blood and other tissue constituents. This enables measurement of the relative concentration of oxygenated and de-oxygenated blood and products of cell metabolism such as cytochrome oxidase and water. Most physiological measurements using NIR spectroscopy are performed with transmitted light. Due to the anatomy of measurement sites, for deep tissue injury detection it is necessary to use backscattered light, which has a much lower intensity. **Methods**

A custom built probe was developed incorporating a cylindrically screened central photodetector and 16 LED dies placed on orthogonal radii. Each radius incorporates LEDs with the same wavelength, separated by 5mm. The LED wavelengths were 770, 810, 870, 905nm corresponding to the chromophores of physiological interest. Using an algorithm developed by Cope and

Delpy (1988) the system produced indices for the concentration of haemoglobin, de-oxy hymoglobin and cytochrome oxidase (HB, HBOx and CtOx). The photodetector was connected to an on-sensor pre-amplifier and to the A/D converter of a TT8 microcontroller (Onset Computers, MA). The LEDs were controlled by FET drivers. Their light output was controlled individually. Software was developed so that each LED was illuminated in turn and the level of backscattered light measured. This system was operated with a sampling throughput of 30Hz that was adequate to detect pulsatile blood flow in the tissue, as well as slowly changing levels in the physiological parameters of interest. The microcontroller performed the necessary calculations in real time for HB, HBOx and CtOx and using an FFT determined the presence of pulsatile flow and the pulse rate.

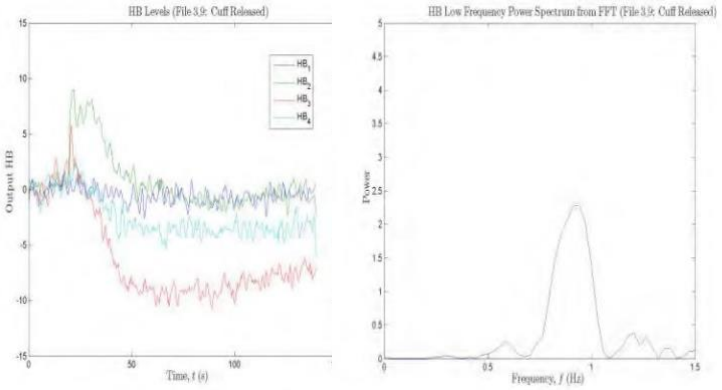

Solis LR, Hallihan DP, Uwiera RR,

Thompson RB, Pehowich ED, Mushahwar VK. Appl Physiol. 2007 May;102(5) 1992-2001

Cope M Delpy DT, Med. & Biol. Eng.& Comp. 1988, 26,3, 289-294

Results

The TSM readily detects changes in HB, HBOx and CtOx both in the amplitude and frequency domains (Figure 1a,b). However two of the LED die locations provide very low signal levels. Location 1 (5mm from centre) is blocked by a cylindrical light guide that prevents crosstalk through the body of the sensor. The position 4 LED (20mm) receives light from about 15mm into the tissue, and these results suggest this is the measurement limit of the TSM.

Conclusion

Although this is a promising approach for the identification of tissue injury in surface tissues, the depth of measurement is not adequate for early detection of tissue changes close to bony prominences, where deep tissue injury is known to occur in the earliest stages of pressure ulceration. **References**

Modeling the Hydrodynamics in Bioreactors for The Expansion of Embryonic Stem Cells

Jiin Cheon, Ian D. Gates, Michael S. Kallos
Department of Chemical and Petroleum Engineering, University of Calgary

Figures

Introduction

Embryonic stem cells (ESCs) can potentially help patients with common diseases such as Parkinson's and diabetes through tissue engineering and regenerative medicine strategies. These methods require large numbers of cells – this can be done by suspension bioreactor[1,2] ESC expansion technology.

Our laboratory has been developing high-throughput microbioreactor (~1 mL) technology. Here, on the path to robust microbioreactor design, we examined the hydrodynamics in a 100mL suspension bioreactor to better understand the fluid flow environment. Improvements were made on a model developed in our laboratory.

Methods

Finite element-based fluid flow modeling software (COMSOL Multiphysics) was used to analyze velocity, shear stress, streamline, vorticity, and pressure

distributions within the 100mL bioreactor versus agitation rate of the impeller, the volume of water, the shape of the impeller, and the location of the impeller. One variable was changed from the base model (100mL of water, paddle impeller, and 100rpm of agitation rate) in each case.

Results

The geometry and a typical resulting velocity profile for the four-bladed rotating impeller are displayed in Figures 1 and 2. The bottom of the bioreactor has a central "bump". ESCs are sensitive to shear stress – if it is too high, they can be torn apart. The model revealed that the highest shear stress was located at the bottom surface of the bioreactor. This was not expected: prior design had been focused on the tip of the impeller as having the maximum shear stress within the fluid environment. The results of the sensitivity study showed that the values of the shear stress, velocity, vorticity, and pressure increased with rising agitation rate. All of the output variables (with one exception of velocity) decreased with increasing distance between the impeller and the bottom surface of the bioreactor. The results demonstrate that the shear stress and velocity distributions can be controlled by impeller speed, impeller design, impeller spacing above the base of the bioreactor, and the overall geometry of the bioreactor.

Conclusions

A robust finite element fluid flow model has been constructed to evaluate the design of bioreactor for ESC expansion. The effects of varying parameters on the hydrodynamic environment of the 100mL bioreactor were closely observed. With the results of this analysis, the next step is to design a microbioreactor with the most suitable configuration that will match the cell expansion seen in the larger 100mL bioreactor.

References

1. Cormier et al., *Tissue Eng.* 2006 Nov;12(11):3233-45. **2**. Alfred et al., Biotechnology Progress, 2011 May-Jun;27(3):811-23.

Figures

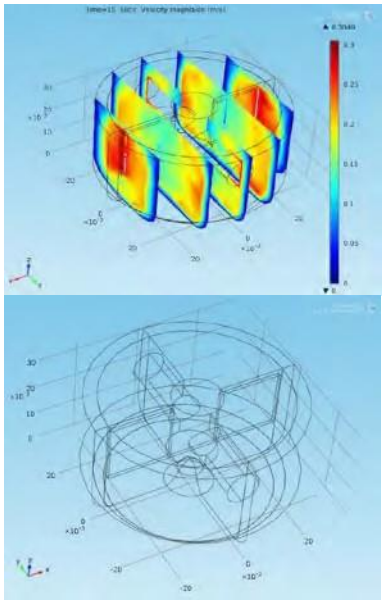

Figure 1: Velocity Profile of 100mL Bioreactor Rotated at 100rpm

Figure 2: Geometrical Shape of the 4 Bladed Impeller Built Using COMSOL Multiphysics

Continuum Mechanical Model of the Cardiac Muscle

Andrey Melnikov and Salvatore Federico
Department of Mechanical and Manufacturing Engineering, The University of Calgary 2500 University Drive NW, Calgary, Alberta, T2N 1N4, Canada

Introduction

Many theoretical models have been proposed and have proved valuable in

deformation does not affect the value of the fourth invariant $I_4(\boldsymbol{C})$. We propose the elastic strain energy potential to take the general form

understanding the mechanical behaviour of the cardiac tissue. So far, however, no large- model has been proposed that is biphasic and interacting, i.e., that accounts for two main phases of the tissue and their interaction: the extracellular matrix and the muscle cells (i.e., the muscle fibres). In order construct such a model, we refined the model of Guo et al. [1], originally developed for intervertebral discs, and whereas in the deformation extended it to the case of a general elastic accounted for is the "residual" after the axial strain energy potential. deformation has been applied.

$$W = W_f + W_s,$$

where the axial contribution W_f and the deformation contribution W_s are given by

$$W_f = \phi_0 W_0(I_{f1} - 3, I_{f2} - 3) + \phi_1(I_{f1} - 3, I_{f2} - 3, I_{f4} - 1, I_{f5} - 1)$$

$$W_s = \phi_0 W_0(I_1 - I_{f1}, I_2 - I_{f2}) + \phi_1(I_1 - I_{f1}, I_2 - I_{f2}, 0, I_5 - I_{f5})$$

W_f is a function solely of the invariants of $\boldsymbol{C}_f^*$, whereas in W_s the strain energy potential. deformation $\boldsymbol{C}_f^*$ has

Background

Guo's model [1] essentially adds a "correction" to a neo-Hookean material, by means of a term in the invariant $I_4 =$ which we weigh the contribution of matrix $\boldsymbol{C}: (\boldsymbol{M} \otimes \boldsymbol{M})$ of the right Cauchy-Green and fibres by their volumetric fractions, the deformation tensor $\boldsymbol{C}$, which indicates interaction between matrix and fibres is transverse isotropy in direction $\boldsymbol{M}$. However, accounted for by the decomposition of the the general case of transversely isotropic deformation. Moreover, since the invariant material is represented by 5 invariants: I_4 is not affected by shear deformation, the $I_1 \dots I_5$ [2]. Under the hypothesis of difference $I_4 - I_{f4}$ vanishes identically in incompressibility the number of invariants the expression of . This W_s leads to the reduces to 4 ($I_3 = 1$), and therefore the important conclusion that, in order to elastic strain energy potential is now a function of the sole invariants $I_1,\ I_2,\ I_4,\ I_5$. capture the anisotropic shear behaviour of a fibre-reinforced material such as the cardiac muscle, it is necessary to take into account

Proposed model also invariant . In other words, invariant I_5 I_5 allows for modelling the additional shear Guo et al. [1] showed that after two suitable stiffness that arises from the fibre subsequent rotations, the deformation reinforcement.

gradient $\boldsymbol{F}$ can be multiplicatively decomposed as $\boldsymbol{F}^* = \boldsymbol{F}_s^* \boldsymbol{F}_f^*$, where $\boldsymbol{F}_f^*$ is the uniaxial deformation and $\boldsymbol{F}_s^*$ is the shear deformation. In order to account for this decomposition we define the invariants I_{fk} of tensor $\boldsymbol{C}_f^* = \boldsymbol{F}_f^{*T} \boldsymbol{F}_f^*$, representing pure

Discussion

Note that, although we adopt an approach descending from the theory of mixtures, in

References

[1] Z.Y. Guo, X.Q. Peng, B. Moran, *J. Mech. Phys. Solids*, 54 (2006), 1952–1971.

[2] Spencer, A. J. M. 1984 Constitutive theory for strongly anisotropic solids. In *Continuum theory of*

stretch in the fibre direction, as a function of the four invariants of the whole deformation
pp. 1–32. Wien, Austria: Springer.
, i.e., . We showed that shear

the mechanics of fibre-reinforced composites (ed. A. J. M. Spencer). CISM Courses and Lectures, no. 282, $I_{fk}(\boldsymbol{C})\boldsymbol{C}$

Sensitivity Analysis of Sinoatrial node

Jaspreet Kaur, Edward Vigmond

12th Annual Alberta Biomedical Engineering Conference

Banff, Alberta October 21st – 23rd, 2011

Introduction

SAN rate regulation is influenced by multiple ion channels. If the SAN does not function, impulses in the SA node can block causing bradycardia, SAN dysfunction, atrial fibrillation and heart failure [1]. However, a detailed description of ionic gradients within the SAN is lacking.

Methods

We performed a sensitivity analysis of a computer model of rabbit SAN [2] with detailed ionic current descriptions for atrial and SAN myocytes. We explored the spread of the action potential in the SA node, and conduction block from the leading pacemaker site towards the septum. Lakatta ionic rabbit SAN model [3] was used as the base model because it incorporates local subsarcolemmal Ca^{2+} releases (Ca^{2+} clock) which interacts with the classic sarcolemmal voltage oscillator (membrane clock) by activating the Na^{+}-Ca^{2+} exchanger current (I_{NCX}). The differential equation describing the membrane potential (V) is:

[illegible]

[illegible] Ionic properties in the SAN were heterogeneous with six distinct regions. An explicit Crista Terminalis (CT) was included with conductivity much lower across it. Ionic conductances were adjusted to produce a stable firing rate with a Cycle Length (CL) of 375ms. We investigated how the CL, Maximum Diastolic Potential (MDP) and Peak Overshoot Potential (POP) were affected by perturbations to different parameters using Latin Hypercube Sampling (LHS). Simulations were run for 3 seconds to stabilize transients.

Results

I_h, I_{CaL} and I_{bNa} are important currents in SAN firing. The effects of varying one parameter at a time, blocking currents, increasing and decreasing conductances were also analyzed. Due to nonlinear interactions between components, system response was not always expected. I_{CaL}, I_{NCX} were vital for POP, whereas I_{Kr} mainly contributed to changes in MDP. Blocking I_{CaL}, I_{Kr}, I_{bNa} and I_{NCX} stopped pacemaker activity.

Blocking hyperpolarizing current (I_h) did not stop oscillations but CL increased by 280% whereas blocking T type calcium current (g_{CaT}), background Ca^{2+} current (g_{bCa}), or sustained inward current (g_{st}) increased CL by 13.3%, 8% and 5.3% respectively (Fig. 1). Sarcoplasmic reticulum uptake (P_{up}) and release rate (ks) block increase CL by 36% and 89% respectively**.** The interdependence between the Ca^{2+} and voltage clocks is thus evident from simulations.

Conclusions

Blocking SR inhibitors and I_h do not stop SAN firing, indicating synergistic dual automaticity in SAN at the tissue level.

Acknowledgements

Authors were supported by Natural Sciences and Engineering Research

Modeling, Control, and Performance Assessment of Blood Plasma Glucose Concentration in Type I Diabetics

Kovid Lee, Mike Foley
147 Silvercreek Drive NW
Calgary, AB T3B4G9

Introduction

With advances in continuous glucose sensing, fast-acting insulin analogs, and a mature technology in the construction of insulin pumps, there comes the commercial realization of a closed-loop pancreas. By removing the patient from the feedback loop and taking the role of a functioning pancreas, the artificial pancreas would be an invaluable solution for type I diabetics. In designing such a biomedical device, one of the most vital components would be the development of a mathematical algorithm that models the body, capable of regulating an insulin infusion given a glucose sensor measurement.

Methods

Simulation and comparison of the two most accepted diabetic models found in published literature was conducted on MATLAB / Simulink: Bergman's minimal model (1981) and Parker's compartmental model (1999). Following model selection and an extensive literature survey, a modified and innovative proportional-only (P-only) controller was implemented and compared to other published controller strategies, aimed to provide satisfactory glucose regulation by 'closing the loop'. Constraints and criteria for the P-only controller were also redefined based on physician recommendations. In addition, a novel performance assessment based only on continuous blood glucose monitoring (CBGM) data was developed. This performance assessment is based on the original work of Harris (1989), where he used the application of minimum variance controller theory to quantitatively evaluate chemical plant performance.

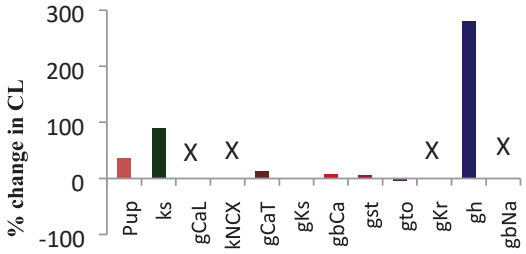

Fig. 1 Effect of blocking currents on SAN frequency

Results

Parker's compartmental model was selected as the model of choice based on its ability to accurately reflect human glucose physiology while being able to handle a wide variety of operations under various control algorithms. In using Parker's compartmental model, the P-only controller was able to provide adequate glucose control and was shown to outperform most published complex algorithms in the application of the artificial pancreas. The performance assessment was able to successfully discern between adequate and poor blood glucose control without bias; this was confirmed with the patient's HbA1c results, the current gold standard in assessing a type I diabetic's blood glucose control.

Conclusions

The simplicity and ease of implementation of a proportional-only controller makes it a

Council of Canada, and a Queen Elizabeth II Graduate Scholarship.

References

1. Circ J. 74(10), 2079-88, 2010.
2. Am J Physiol Heart Circ Physiol, article in Press, August 19, 2011.
3. Am J Physiol Heart Circ Physiol 296, H594H615, 2009.

Figures

feasible and universal solution in automatically regulating blood glucose levels in type I diabetics; this is in contrast to the many published control strategies that require invasive identification experiments and have more inherent complications due to their complex nature. The practicality of including a performance assessment to compliment the current HbA1c assessment to aid in future blood glucose management would make consults easier for the physician and allow the type I diabetic to analyze their own CBGM data. Because the performance assessment can also be conducted at home, it can also be used as an individualized educational tool, allowing the type I diabetic to make note of any improvements that could be made to their current insulin regimen and strive for better performance on a daily basis.

References

Bergman RN, Phillips LS, Cobelli C. **Physiologic Evaluation of Factors Controlling Glucose Tolerance in Man.** *J. Clin. Invest.* 1981; **68**:1456-67

Harris T. **Assessment of control loop performance.** *Canada. J. Chem. Eng.* 1989; **67:** 856-61

Parker RS. **Model-Based Analysis and Control for Biosystems.** *PhD Thesis.* University of Delaware, Department of Chemical Engineering; 1999

NORMAL AND OSTEOARTHRITIC SYNOVIAL STEM CELL-DERIVED TISSUE-ENGINEERED CONSTRUCTS RESPOND TO MECHANICAL STIMULUS FOLLOWING CHONDROGENIC DIFFERENTIATION

Geoff Buckley-Herd, Roman Krawetz, David A. Hart
University of Calgary

Introduction

Tissue-engineering (TE) comprises cells, a scaffold, and appropriate signals. In the context of TE of articular cartilage for treatment of osteoarthritis (OA), synovial tissue-derived mesenchymal stem cells (sMSCs) have been demonstrated to be particularly suitable. These MSCs are present in the synovial fluid and their numbers increase dramatically with the onset of OA. Recent studies generated scaffold-free tissue-engineered constructs (TECs) from sMSC monolayers treated with ascorbic acid (AA)[1,2]. These TECs retained their chondrogenic potential and were observed to aid in cartilage repair following transplantation into chondral defects within a porcine model. The repair could be improved by enhancing the TECs by obtaining a more mature chondrogenic phenotype. As it is also known that mechanical loading can be used to modulate MSCs differentiation[3] the goal of the study is to use chondrogenic factors and mechanical loading to enhance the TEC properties based on qPCR, histology, and mechanical properties.

Methods

Human sMSCs were derived from donor synovial membrane (SM) and synovial fluid (SF) and isolated using magnetic purification. When the cells reached confluence they were treated with either chondrogenic media containing TGF-β3, BMP-2, AA, and dexamethasone, or media supplemented with only AA (TEC) for a period of 14 days. The chondrogenic TECs (cTECs) and AA-treated TECs were then embedded in surrogate agarose scaffolds and subjected to mechanical compression of 10% strain at 1 Hz for 4 hours followed by 16 hours rest using a modified Flexcell system. Non-loaded TECs were maintained in parallel as controls. After loading, the remaining TECs and cultures were harvested for analysis. Analysis included cell viability, RT-qPCR, histology and immunohistochemistry, and mechanical testing.

Results

TECs were generated from SF and SM MSCs from both normal and osteoarthritic tissues. Assessment of cell viability showed viable cells following TEC generation and loading. Mechanical loading differentially regulated several genes commonly used as markers of chondrogenic differentiation in both the cTECs and AA-treated TECs. Following mechanical compression, mRNA expression of SOX-9 and aggrecan are upregulated compared to non-loaded controls, while type-II collagen expression is highly variable. Histological assessment using immunofluorescence indicated the presence of SOX-9 in loaded TECs.
Mechanical testing was used to approximate the elastic moduli of the TECs but no significant differences could be detected, likely due to the surrogate scaffolds.

Conclusions

TECs were successfully generated from all cell lines tested. Both chondrogenic differentiation and mechanical loading were found to enhance the TECs in terms of two of the three selected outcome measures. Optimization of the protocol in terms of loading regimen, initial cell population, and TEC generation could lead to further enhancements as well as larger, more uniform TECs. Refinement of the mechanical testing to decouple the contributions of the scaffold versus the TEC would also give additional insight.

References

1. Ando, W. *et al. Biomaterials*. 2007.
2. Ando, W. *et al. Biomaterials*. 2010.
3. Meyer, E.G. *et al. J. Biomech*. 2010.

Introduction

Soft biological tissues, such as articular cartilage, can be represented by a porous matrix saturated by a fluid and reinforced by a network of statistically oriented fibres. The permeability of such tissues has been previously modelled and implemented for small deformations [1,2]. Recently, a new mathematical model has been proposed for the study of permeability under large deformations [3] and has been incorporated with non-linear elasticity models [4].

The aim of this research is to implement a numerical formulation of the above mentioned mathematical model of porous fibre-reinforced biological tissues under large deformations. This involves implementation of both the non-linear elastic formulation, as well as the anisotropic formulation of the permeability tensor, which has not been done before.

Methods

Due to inability to manipulate certain variables in commercially available FEA packages such as ABAQUS, the full model was implemented in the open source package FEBio [5]. The use of an open source package allowed access to all the pertinent variables, but it also involved significantly more programming, since the implementation had to be programmed in C++ language.

The statistical nature of fibre orientation and the averaging integrals associated with it were accounted for by means of the use of spherical designs [6], as in the previously implemented non-linear elastic model [7]. This method of implementation, through the use of a

Numerical Implementation of a Large-Strain Model of Porous Fibre-Reinforced Tissues

Aleksandar Tomic and Salvatore Federico
Department of Mechanical and Manufacturing Engineering, University of Calgary
University Drive NW, Calgary, Alberta, T2N 1N4, Canada

parameter called the orientation or concentration parameter, can also be used to define the statistically dominant fibre direction. For example, a value zero of the orientation parameter gives an isotropic fibre orientation in the reference configuration, while increasing positive values give distributions closer and closer to aligned in the main direction, and decreasing negative values five distributions closer and closer to an in-plane isotropic distribution.

S. Federico and A. Grillo, *ICNAAM Conference 2010*, 351-354 (2010). [4] S. Federico and A. Grillo, *Mechanics of Materials*, in press
[5] S.A. Maas and J.A. Weiss, *FEBio User's Manual*, mrl.sci.utah.edu/software (2007) [6] R.H. Hardin and N.J.A. Sloane, *Discrete Comput Geom*, **15**, 429-441 (1996)
[7] S. Federico and T.C. Gasser, *J.R. Soc. Interface*, **7**, 955-966 (2010)
[8] Mollenhauer et al., *Conn. Tiss. Res.*, **44**, 201-207 (2003)

MMP-2 Cleavable Peptide Hydrogel Delivery System Kinetics

Kyle Koss, Larry D Unsworth
Department of Chemical and Materials Engineering, University of Alberta, 11487 89 ave, Edmonton, AB, T6G 2M7
National Institute for Nanotechnology, NRC, 11421 Sasketchewan Dr NW, Edmonton, AB, T6G 2M9

Introduction

Peptides are the fastest growing segment of the pharmaceutical industry, and are generally considered the ideal therapeutic: specific, potent, small enough for diffusion, etc. That said, peptide therapeutics suffer from a major drawback, they are easily cleaved by circulating proteases and are thus short lived; this factor makes them almost impossible to effectively deliver *in vivo*. Self-assembling peptide $(RADA)_4$ nanofibers are a novel class of biocompatible peptides that, upon injection, assemble into a 3D hydrogel matrix which is capable of storing water and large molecules. Moreover, it is thought that synthesizing peptide therapeutics to them and forming a hydrogel will afford protection from circulating proteases. Controlling the release kinetics of these bonded peptide therapeutics from the nanofibers is crucial

Results

Preliminary test simulations have shown physically admissible results. A sample with an initially anisotropic distribution of fibres develops anisotropy under compression, as expected, and this is evident in the pore pressure, fluid flux, and the stress. Similarly, compression of samples with fibres aligned in the main direction, or lying on the transverse plane have also shown evolution of the fibre direction during compression.

Conclusions

The preliminary tests performed will be followed by simulations of compression tests on cartilage samples with realistic fibre distributions, as from the literature [8], and comparison with experimental results.

References

[1] S. Federico and W. Herzog, *Int. J. Solids Struct.* **45**, 2160-2172 (2008).
[2] S. Federico and W. Herzog, *Biomech. Model. Mechanobiol.* **7**, 367-378 (2008). [3]

to their efficacy. Utilizing the spatiotemporal profile of tissue resident enzymes affords an 'on-demand' release strategy; the apparent kinetics of which being vital for successful clinical treatment. To this end, kinetic degradation models of $(RADA)_4$ based hydrogels with matrix metalloproteinase-2 (MMP-2) cleavable bonds will be developed using isothermal titration calorimetry (ITC)[1] [2] [3].

Methods

Initial enzyme kinetics and ITC sensitivity of MMP-2 were measured *via* the cleavage of a standard fluorescent tagged substrate [(7-methoxycoumarin-4-yl)Acetyl-PLGL(3-[2,4dinitrophenyl]-L-2,3-diamino proplonyl)-AR-NH_2][4]. ITC was used to as a continuous method to quantitatively characterize the cleavage rates derived from enthalpy and heat flow [3]. Pro and active forms of MMP-2 were used. Single injection and multiple injection methods were performed. The Michaelis-Menten approach was used to determine the maximum reaction velocity V_{max}, the reaction speed constant k_{cat}, and the overall reaction rate and Michaelis constant K_M [3]. However, heat flow change is non-specific; therefore MMP-2 cleavage was qualitatively assured using fluorescence photospectroscopy.

Ultimately, cleavage will be observed for $(RADA)_4$-GG-GPQG+IASQ and $(RADA)_4$GG-GPQG+PAGQ, known for their high and low MMP-2 sensitivity, respectively [5]. To assure nanofiber formation in the reaction conditions, circular dichroism was performed upon doping these peptides with pure $(RADA)_4$.

Results

Only active MMP-2 was ITC sensitive. Single injection method was also only able to perform within instrument sensitivity at the chosen reaction concentrations. The kinetic parameters were comparable to literature: K_M was 5.6nM, k_{cat} was 0.043s^{-1}, and V_{max} was 43.2nM/s, which gives a k_{cat}/K_M of 772,000$M^{-1}s^{-1}$ [4]. Control substrates were cleaved by both MMP-2 pro and active as they fluoresced at 400nm emission with 328nm excitation. Observable nanofiber structure was noted at 15% $(RADA)_4$ doping of the cleavable peptides.

Conclusions

ITC has adequate sensitivity for characterizing MMP-2 cleavage, which was confirmed using fluorescence spectroscopy. Therefore cleavage of $(RADA)_4$GPQG+IASQ and $(RADA)_4$-GPQG+PAGQ will be observed using ITC. Nanofibers form with $(RADA)_4$ doped $(RADA)_4$-GGGPQG+IASQ and $(RADA)_4$-GG-GPQG+PAGQ, allowing for hydrogel system kinetic analysis.

References

1. **Koutsopoulos, S., et al.**, 2009, PNAS, 106, 12: 4623-4628.
2. **Selikar, D., et al.**, 2004, Journal of Biomedical Materials Research, 64: 704-716.
3. **Todd, M. J. and Gomez, J.**, 2001 , Analytical Biochemistry, 2001, Vols. 296:179-187.
4. **Knight, C. G., et al.**, 1991, FEBS, 296(3):263-266.
5. **Nagase, H. and Fields, G. B.**, 1996, Biopolymers, 40: 399-416.

Engineering stem cell derived bone and cartilage in novel biomimetic bioreactor

Poh Lee[1]; Derrick Rancourt, PhD[1]; Roman Krawetz, PhD[2]

University of Calgary, [1]Department of Biochemistry & Molecular Biology, [2] Department of Surgery.

Introduction

Research in bone and cartilage engineering for regenerative medicine approaches has expanded over the last decade; however, few methods have been clinically translated.

Partially because most engineered constructs lack anatomical and mechanical characteristics of native tissues, and can be resorbed after implantation. Previous studies from our lab have demonstrated that collagen 1 and chondroitin sulphate can induce osteogenesis and chondrogenesis respectively. However, prolonged maintenance of culture remains a hurdle in a static tissue culture setting. In this study, a novel biomimetic bioreactor system capable of emulating the physiological environment was developed. We sought to engineer a collagen-based bone and cartilage construct (EBCC) that possess both anatomical and mechanical resemblance to tissue in physiology.

Methods

A perfusion bioreactor was designed to provide continual flow of media to the EBCC at constant rate. The design allows alternation of media compositions in realtime, based on the needs of the EBCC at each stage of differentiation. An isolated polymerized collagen 1 platform was fabricated within the bioreactor to support embryonic stem cells (ESC) differentiation. Nutrients and oxygen gradients developed within the bioreactor are based on the design of bioreactor and seeding density of ESCs. This gradient is exploited (with media supplementation) to promote both osteogenesis and chondrogenesis resulting in EBCC formation. Furthermore, the materials used to assemble the bioreactor are amenable to direct mechanical stimulation (bending and compression) and is applied to the EBCC to enhance differentiation.

Results

A dynamic cell culturing platform with differential pO_2 level was developed within the bioreactor. It ranged from 85mmHg at the top to 1.3mmHg at the bottom (Fig 1).

An EBCC with the length of 50mm and diameter of 5mm was derived after 45 days (Fig 2). Cells in EBCC remained viable for at least 52 days post-inoculation, with extensive cellular remodeling observed. Quantitative PCR (qPCR) analyses demonstrated significant decrease in pluripotent marker, OCT-4, with coinciding increases in osteogenic and chondrogenic markers. Immunofluorescence staining had shown positive expression of Sox-9, Osteocalcin and TRAP at distinct regions within the construct in correspondence to the pO_2 level. Positive Alcian blue staining was observed within the interior of the EBCC, whereas Alizarin red staining was distributed throughout the construct.

Conclusions

The novel system is capable of maintaining stable cell propagation over extended time. It enables the development of a large-sized engineered construct with structural integrity. Through exposure to differential pO_2, we have engineered a dynamic EBCC comprised of chondrocytes, osteoblasts and osteoclasts. In the future, external mechanical will be applied on the construct in real time; in an attempt to induce further maturation of EBCC to bear mechanical properties resembling the native tissue and used for treating patients with large size fractures or degenerative joint diseases. In addition, we aimed to generate an *in-vitro* OA model with this system for pharmacological studies. Figures

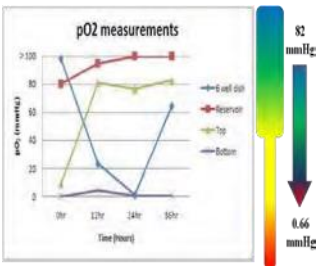

Fig 1: pO2 measurements at various conditions.

Fig 2: Dimension of EBCC after 48hrs of cultivation

Characterization of Recombinant Human PRG4 as an Ocular Surface Boundary Lubricant

N Masala[1,2], S Morrison[3], M Samsom[3], H Sheardown[4], T Schmidt[1,2,3]

Schulich School of Engineering – [1]Department of Mechanical & Manufacturing Engineering, [2]Centre for Bioengineering Research and Education; Faculty of Kinesiology – [3]Human Performance Lab; University of Calgary.
[4]Chemical Engineering, McMaster University.

Introduction

Dry-eye disease involves tear film instability that can lead to increased friction forces between the cornea and eyelid or contact lens, potentially contributing to ocular discomfort associated with the disease. Furthermore, these greater forces can result in surface-to-surface contact between the cornea and eyelid or contact lens, where boundary lubrication can be dominant[1]. Proteoglycan 4 (PRG4) is a mucin-like glycoprotein originally discovered in synovial fluid as a boundary lubricant[2] (this boundary lubricating ability is due to Olinked glycosylations[3]), which has recently been shown to function as an ocular surface boundary lubricant[4]. Motivated by advances in recombinant protein expression technology[5] and PRG4's potential use as a friction-reducing contact lens coating, which would ultimately require autoclave sterilization, the objectives of this study were to: 1) biochemically characterize recombinant human PRG4 (rPRG4); and 2) assess the boundary lubricating properties of rPRG4, both before and after sterilization by autoclaving, at a cornea-contact lens material (PDMS) biointerface.

Methods

SDS-PAGE western blot analysis using the anti-PRG4 antibodies LPN, J108N, and PNA was performed on native PRG4 (nPRG4) and rPRG4 samples, both nonreduced and reduced, with and without enzymatic removal of glycosylations by neuraminidase and O-glycanase. Human corneas and PDMS were articulated against each other, subject to physiological loads of 8-25 kPa, at effective sliding velocities of 0.3-30 mm/s. Test lubricant sequences were A) saline, rPRG4 @300µg/mL, nPRG4 @300µg/mL, and saline; and B) saline, autoclaved rh-PRG4 @300µg/mL, rPRG4 @300µg/mL, and saline. Static and kinetic coefficients of friction were calculated.

Results

rPRG4 demonstrated similar immunoreactivity to nPRG4, and effectively lowered friction at the cornea-PDMS biointerface. Western blotting indicated immunoreactive rPRG4 bands had a similar apparent molecular weight (MW) to nPRG4, and decreased appropriately upon reduction as well as enzymatic removal of glycosylations. Kinetic friction coefficients, which were highest in saline (0.31±0.06 to 0.40±0.06, mean±SEM), were similar in rPRG4 (0.12±0.01 to 0.25±0.03) and nPRG4 (0.19±0.02 to 0.28±0.03) across all velocities. Autoclaved rPRG4 had similar values to rPRG4 as well (0.19±0.02 to 0.27±0.03, 0.16±0.01 to 0.26±0.02, respectively).

Conclusions

rPRG4 demonstrated similar biochemical and ocular surface lubricating properties to nPRG4, and may function as an effective friction-reducing contact lens coating. The biochemical data suggests the rPRG4 is

appropriately glycosylated, which are necessary for its boundary lubricating properties[3]. The biomechanical data is consistent with a previous study, where nPRG4 reduced friction at a cornea-PDMS biointerface[4], and additionally suggests rPRG4's boundary lubricating ability is not affected by autoclaving. Future work examining other contact lens materials and modification of rPRG4 for enhanced binding will contribute to further development of PRG4 as a dry eye therapeutic.

References

1. Holly+ *Lacrimal Gland, Tear Film, and Dry Eye*

Syndromes, New York: Plenum Press, '94. 2. Swann+ *J Biol Chem* '81. 3. Jay+ *Glycoconjugate J* '02 4. Morrison+ *Eye & Contact Lens* (in revision).

5. Girod+ *Nature Methods* '07.

An Implantable Baroreceptor Stimulating Device; Its Ability to Improve Renal Blood Flow

Steven Burgoyne[1], Dimitrios Georgakopoulos[2], & John V. Tyberg[1]

[1] University of Calgary, Calgary, AB, Canada

[2] CVRx, Inc., Minneapolis, MN, USA

Introduction

Arterial baroreceptors are stretch receptors that respond to blood pressure changes by eliciting a response of the autonomic nervous system. High-pressure baroreceptors are located in the aortic arch and carotid arteries. Increased blood pressure stimulates an autonomic nervous system response, decreasing heart rate and reducing peripheral vascular resistance, thus decreasing arterial blood pressure[1].

CVRx Inc., a medical device company, has developed an implantable device to provide electrical stimulation to the carotid baroreceptor. The device is intended to treat patients with chronic high blood pressure for whom traditional drug therapy is unsuccessful.

Due to the kidney's sensitivity to sympathetic stimulation, it is hypothesized that electrical stimulation of the carotid baroreceptor will increase conductance and lower the zero-flow pressure, thus improving renal blood flow. These effects of electrical stimulation may be greater if sympathetic stimulation has already been enhanced.

Methods

Three 20kg mongrel dogs were anaesthetized and ventilated. Flow was measured using an ultrasonic flow probe on the renal artery. A pressure-measuring catheter was inserted via the femoral artery and advanced in the aorta to the level of the renal artery. The CVRx electrode was implanted on the right carotid artery at the level of the carotid sinus. The chest was opened and the left-anterior-descending coronary artery was dissected for occlusion.

Renal pressure and flow data were collected before and after device activation. Myocardial ischemia was produced by coronary occlusion; after occlusion, data were collected before and after device activation.

Results

Activation of the baroreceptor stimulating electrode produced an average drop in mean renal pressure of 15.3 mmHg. Renal zeroflow pressure decreased by 7.1 mmHg, while renal conductance decreased by 1.6 %.

After coronary occlusion, activation of the device reduced average renal pressure by 32.3 mmHg. Renal zero-flow pressure decreased by 25 mmHg while renal conductance increased by 34 %.

Conclusions

Electrical stimulation of the carotid baroreceptor produces a repeatable and sustainable drop in arterial blood pressure.

Effects on renal blood flow before coronary occlusion are mixed: a small decrease of zero-flow pressure and a decrease in conductance were observed in two of three experiments.

Presumably, coronary occlusion increases renal sympathetic stimulation. After occlusion, device activation increased renal conductance and decreased zero-flow pressure in all three experiments - despite a reduction in blood pressure and heart rate. Increased conductance means that the kidney accepts more flow at a given driving pressure and a decrease in zero-flow pressure means that diastolic flow, upon which vital organs (brain, heart, and kidney) appear to depend, tends to increase. These results suggest that device activation may improve renal blood flow most in disease states where sympathetic stimulation is increased, as may be true in hypertension and heart failure.

Reference

[1] Berne RM., Levy MN., (2001) *Cardiovascular Physiology* pp.187-189

Rapid Serial Sarcomere Loss Caused by Electrical Stimulation in Rabbit *Triceps Surae* Muscles

Maria Yamamoto, Tim Leonard, Walter Herzog
Human Performance Laboratory, University of Calgary

Introduction

Muscle spasticity, as occurs in patients with cerebral or people who have suffered from a stroke, are involuntary muscle contractions that usually occur due to lesions in the brain. Muscle spasticity causes muscles and fascicles to become short and stiff, thereby limiting the range of motion of joints and affecting everyday function. It has been suggested that stiffness in spastic muscles is caused by a decrease in the number of serially arranged sarcomeres, but the reason for this loss in sarcomeres remains a matter of scientific debate. In 1981, Tabary and Tardieu [1] showed that 12 hours of continuous low-level stimulation of the soleus muscles in guinea pigs caused a 25% decrease in the number of serial sarcomeres. Patients with brain lesions also have low level, involuntary stimulation of their “spastic” muscles, thus it seems possible that the loss of serial sarcomeres may be caused by this low-level stimulation. Therefore, the purpose of this study was to test if after 10 hours of continuous electrical stimulation of the tibial nerve in New Zealand White rabbits, there would be a substantial decrease in the number of serial sarcomeres in the soleus, plantaris and medial gastrocnemius (MG) muscles..

Methods

The MG, plantaris, and soleus muscles were stimulated via the tibial nerve in New Zealand White rabbits (n=3) for 10 hours in one of the legs (20 Hz at three times the α motoneuron threshold). The tibial nerve in the contralateral control leg was transected to ensure no cross-over training effects. After the stimulation period, the animals were sacrificed and the hind limbs removed. The hind limbs were then placed in a 10% formalin solution at carefully controlled knee and ankle angles, for at least a week. Four to

six tissue samples were harvested from each muscle from precisely defined locations, and were placed in 30% nitric acid for approximately 50 hours to digest the connective tissues. The acid digested samples were then placed in 100% glycerol. Following the digestion process, five individual fascicles were teased out from each of the tissue samples and mounted on prepared slides. These slides were then analyzed for fascicle length by using a camera system with specialized software, and sarcomere lengths were determined at five points along the entire fascicle length using a laser diffraction method. The number of serial sarcomeres in the muscles was then calculated by dividing the fascicle length by the average sarcomere length.

Results

The serial sarcomere number in the experimental MG was 23% (± 4.4%) smaller, in the Plantaris was 25% (± 2.9%) smaller, and in the Soleus was 29% (± 7.0%) smaller than the corresponding contralateral control muscles. The decrease in sarcomeres in the soleus was significantly greater than in the MG (r=0.0353). The sarcomere loss observed here is similar to the 25% loss reported by Tabary and Tardieu in guinea pigs.

Conclusions

The results of this study suggest that chronic, low-level muscle stimulation is a potent regulator of serial sarcomere number. Future studies will need to focus on how this sarcomere loss may be limited or stopped in patients with chronic, involuntary stimulation of muscles caused by brain lesions.

References

[1] Tabary, J. C., Tardieu, C., Tardieu, G., Tabary, C. (1981) "Experimental rapid sarcomere loss with concomitant hypoextensibility." *Muscle and Nerve*, 4, 198-203

Assessing Arrhythmia Risk in Diabetic and Ischemic-preconditioned Rat Hearts

Mishriki S.[1], Randall, A.[2], Nygren, A. [2],
Chemical Engineering, [2] Electrical and Computer Engineering, [1,2] Libin Cardiovascular Institute of Alberta,
University of Calgary, Calgary, AB

Introduction

Arrhythmia is an irregular heartbeat that results in inefficient mechanical heart output, which often times is fatal. Arrhythmias can occur during stresses such as ischemia reperfusion where the heart is deprived from nutrients and oxygen.

Diabetic tissue cannot access glucose and switches to fatty acid metabolism as a source of energy [1]. Ischemic-preconditioning (IPC) involves a short period of ischemia (no flow) before a prolonged period of no flow. As a result, similar to the diabetic tissue, tissue exposed to IPC switches from glucose-based to fatty acid-based metabolism.

Fatty acid metabolites activate cardioprotective mechanisms that protect the heart from arrhythmia during ischemia reperfusion (IR) injury.

Methods

Male, 200-300 gram Sprague Dawley rats were used. Rats were anesthetized and hearts were extracted and hung using the Langendorff perfusion method. Hearts were perfused with standard 37˚C Krebs-

Henseleit buffer aerated with 95% O_2/ 5% CO_2.

Three electrodes were sutured and ECG recordings were collected and analyzed. The four groups analyzed were control, diabetic (STZ), ischemic-preconditioned (IPC), and a combined treatment (IPC+STZ).
Arrhythmias were categorized into different categories based on the Lambeth Conventions standards [2].

Results

The time elapsed to flatline during ischemia for the STZ group was significantly different from the control group (15.5± 3.7 minutes for STZ compared to 7.33 ± 0.8 minutes for control).

Ventricular Tachycardia (VT), and Fibrillation (VF) in the treated groups were not significantly different from the control group when analyzed individually.

During the first 5 minutes of reperfusion, STZ and IPC+STZ groups have a higher chance of developing normal sinus rhythm (SR) in comparison to control ($P<0.05$).

Conclusions

IPC + STZ group has a reduced risk of arrhythmia during reperfusion. STZ hearts react differently to IR in comparison to control hearts and the condition of the tissue should be considered to predict outcome of IR and for possible treatment strategies.

References

[1]Am J Physio Heart Circ Physiol., 300(1).2011 H326-34.
[2] Cardiov. Res., 2:441-455, 1988

Figures

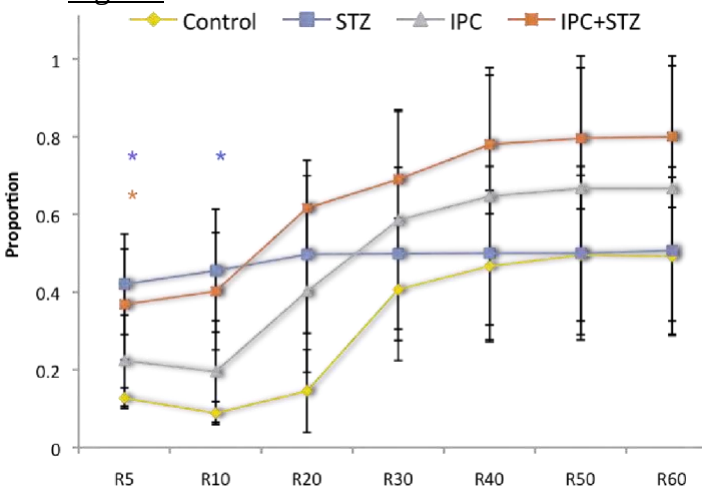

Figure 1: Proportion of SR during Reperfusion

A) 

Figure 2A: a normal beat (Sinus Rhythm)

B) 

Figure 2B: Ventricular Fibrillation

C) 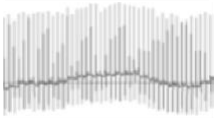

Figure 2C: Ventricular Tachycardia

Figure 2: Images of ECG Recordings

Kinematic Differences between Gender Specific and Traditional Femoral Implants

Saevarsson SK, Sharma GB, Ho KC, Ramm H, Lieck R, Zachow S, Anglin C
University of Calgary

Introduction

In the last few years gender-specific (GS) implants have been introduced that suit the female knee shape better. Several studies have been published showing how the knees of females differ from the knees of males (Mahfouz 2007).

To increase the success rate of total knee replacements (TKR) in females the industry is offering GS knee implants. Several studies have been published comparing the clinical outcome between males and females with traditional implants and what effect gender-specific knees might have. Most of these studies did not find a significant difference in outcome once other factors are accounted for, nor did they find any indications that GS implants might be better than the traditional (Emerson 2008; MacDonald 2008). However, clinical scores are unable to detect subtler differences related to patellofemoral function, which could lead to differences in patient satisfaction. The industry claims that the design differences should lead to better patellar tracking in women but, to our knowledge, no *in vivo* study has been performed that evaluates what effect GS knees have on patellofemoral kinematics. We have developed a unique protocol that makes it possible to evaluate this.

Methods

We imaged 25 subjects who had undergone a TKR. Of these, 3 subjects were bilateral resulting in 17 GS implants and 11 traditional implants. Static radiographs were taken at 8 different knee flexion angles, 0°,

15°, 30°, 45°, 60°, 75°, 90° and at max flexion. In order to have the subjects weightbear their knee, we had them put their foot up on different heights of plexiglass increments. For each knee flexion angle two images were taken, one with the X-ray source at 10° and one with the X-ray source at 0°. Having images from two different angles makes it easier to match 3D models of the implants to the sagittal 2D images.

The 3D models of the implants were created by reverse engineering a computed tomography scan of the implants. A calibration frame was built and placed around the subject's knee, which makes it possible to calibrate the 2D images.

Results

To date the kinematics of 6 subjects have been analyzed, 3 subjects with GS implants and 3 with traditional implants. The results are presented in Figure 1. As can be seen, the standard deviations within each group are large. Significant differences between the two groups were not found ($p>0.05$).

Conclusions

We aim to analyze at least 10 subjects in each group within the next month. The trends regarding differences in mediolateral translation and rotation may become significant with greater numbers of subjects. The different implant design for the GS implants could potentially have other effects; we intend to compare the quality of life between the two groups as well as take a closer look at the geometry and how well the patella tracks in the femoral groove.

References

Emerson, R. H. et al. (2008) *Clin Orthop Relat Res*, 466(11), 2706-10.

MacDonald, S. J., et al. (2008) *Clin Orthop Relat Res*, 466(11), 2612-6.

Mahfouz, M. et al. (2007) *Comput Methods Biomech Biomed Engin*, 10(6):447-456.

Figures

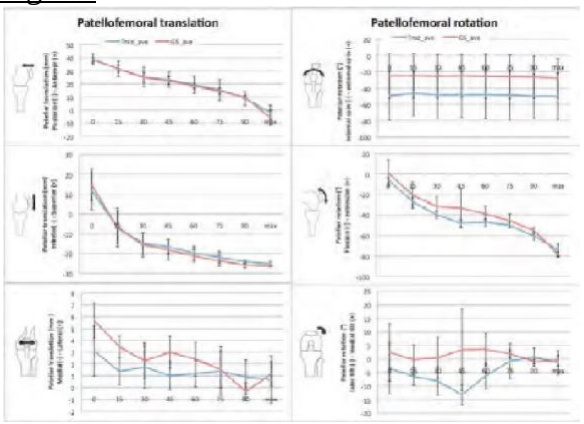

Fluid Flow Induced Cell Signaling in Cardiovascular Tissues

Alexander G. Obrejanu, Robert D. Shepherd, and Kristina D. Rinker
Cellular and Molecular Bioengineering Research Laboratory, University of Calgary, Calgary AB, Canada

Introduction

Local blood flow characteristics affect the localization of cardiovascular diseases within the vasculature[1]. Endothelial cells (ECs) that line artery walls are directly exposed to forces of blood flow, such as shear stress (the frictional force), which profoundly influences vessel physiology. ECs exposed to different levels of fluid shear stress display altered gene expression profiles, which dictate their susceptibility to the development of atherosclerosis[2]. While outcomes such as this can be readily observed, the mechanisms by which mechanical forces are translated into chemical signals are not fully understood. Investigation of signal transduction *in vivo* is difficult because local flow environments vary greatly with small changes in position making it challenging to harvest samples exposed to the same flow conditions. Our lab has developed a system based on the parallel-plate flow chamber design to provide uniform flow forces on endothelial cells[3]. Using this system, we have identified a new signaling pathway that cells use to respond to fluid forces. We have found Smad and Akt to be key components in this pathway[4]. Little is known about the role of these molecules in fluid flow exposed ECs. Therefore the objectives of this research were to investigate the effects of Smad2 knockdown on EC gene expression and to examine Akt levels in animal vessels as a function of position and fluid flow.

Methods

Human aortic ECs (HAECs) were exposed to 2 and 10 dyne/cm^2 shear stress in parallel plate flow chambers for up to 24 hours. Flow experiments were performed with Smad2 siRNA transfected HAECs.

Expression levels for molecular targets from static and flow cultures were determined by western blot and real-time qRT-PCR. Immunofluorescence microscopy was performed on aortic and thoracic rat arterial tissue following approved ethics protocols.

Results

Static cultures transfected with Smad2 siRNA displayed reduced total Smad2 mRNA and protein levels compared to nontransfected cells. Treatment with siRNA changed the gene expression of a number of genes including Serpine-1, PDGF-B, and KLF2, which are all known to be affected by shear stress. Also, the flow-induced expression of Akt in culture from previous studies was validated in rat aortic tissue. Levels of the phosphorylated protein species pAkt(473) were higher in thoracic aorta samples (high fluid shear stress regions) when compared to aortic arch samples (low fluid shear stress regions).

Conclusions

The magnitude dependent activation of Smad signaling pathway components and their

[1] Malek AM, Alper SL, Izumo S. (1999). *JAMA*. **282**(21): 2035-2042.
[2] Brooks AR, Lelkes PI, Rubanyi GM. (2002). *Physiol Genomics*. **9**(1): 27-41.
[3] Viegas KD, Dol SS, Salek MM, Shepherd RD, Martinuzzi RM, Rinker KD. (2011). *Biomed Eng Online*. **10**:20.
[4] Shepherd RD, Kos SM, Rinker KD. (2011). *Am J Physiol Heart Circ Physiol*. **301**(1):H98-H107.

presence in the nucleus of fluid flow exposed endothelial cells suggests that they are important for flow dependent mechanotransduction and changes in gene expression. The finding that siRNA knockdown of Smad modulated the expression of a number of genes under flow further implicates its importance in EC function under flow exposure. The presence of this pathway *in vivo* was shown in arterial rat tissue and suggests this mechanism is conserved in multiple species. Further investigation of this pathway is underway and could lead to the development of new approaches to activate the protective functions of high shear stress in cardiovascular disease prone regions in the vasculature.

References

1. Ferrari, M. Cancer nanotechnology: opportunities and challenges. *Nature Reviews Cancer* **5**, 161-171 (2005).
2. Ross, R. Atherosclerosis--an inflammatory disease. *N Engl J Med* **340**, 115-126 (1999).
3. Chithrani, B. D., Ghazani, A. A. & Chan, W. C. Determining the size and shape dependence of gold nanoparticle uptake into mammalian cells. *Nano Lett* **6**, 662-668 (2006).
4. Gratton, S. E. A. *et al.* The effect of particle design on cellular internalization pathways. *Proc Natl Acad Sci U S A* **105**, 11613-11618 (2008).
5. Dai, G. *et al.* Distinct endothelial phenotypes evoked by arterial waveforms derived from atherosclerosis-susceptible and -resistant regions of human vasculature. *Proc Natl Acad Sci U S A* **101**, 14871-14876 (2004).

Disturbed Flow Alters Nanoparticle Adhesion to Vascular Endothelial Cells

Robyn Steele, Amber Doiron, Robert D. Shepherd, Sarah Childs, Sean Jiang, Kristina D. Rinker

Schulich School of Engineering – Department of Chemical & Petroleum Engineering, Cellular and Molecular Bioengineering Research Laboratory, University of Calgary

Introduction

Nanotechnology is a rapidly growing field with a wide range of applications including drug delivery and medical imaging (1). In order to predict how nanoparticles (NPs) will distribute once they enter the blood stream, a greater understanding of the effect of fluid flow is required. Blood flow varies greatly throughout the vasculature with some regions experiencing disturbed flow, or eddies, in areas of vascular branching or curvature, regions of new vessel growth or in the presence of atherosclerotic plaques (2). Recent research by us and others has examined the effect of NP shape, size, and density on uptake on endothelial cells, which form the blood vessel lining (3,4). However, little is known regarding how flow affects NP adhesion. In this study, a flow chamber was used to examine the effects of flow rate (shear stress) and flow pattern (disturbed flow) on NP uptake by human umbilical vein endothelial cells (HUVEC).

Methods

HUVEC were seeded on collagen coated glass microscope slides and grown at 37°C and 5% CO_2 until confluent. A polycarbonate flow chamber was assembled consisting of two rectangular silicon gaskets, a cultured slide and a glass field finder slide.

One of the two gaskets contained a backwards-facing step, creating a disturbed flow region near the step followed by a laminar flow region downstream. In nonpreconditioned assays, slides were exposed to flow at two shear stresses (1 Dyne/cm^2 and 8 Dyne/cm^2) with NPs (Invitrogen 200 nm polystyrene spheres at 10µL/mL) for 30 minutes. Preconditioned slides were exposed to flow (at 1 Dyne/cm^2) for 24hr; NPs were injected into the flow loop at 10µL/mL and allowed to circulate for 30 min. Slides were washed using warm Hepes Buffered Saline Solution (HBSS), fixed with 4% para-formaldehyde and stained with Hoechst and Cellmask. Images were acquired on an Olympus fluorescence microscope. NP adhesion analysis was performed with ImageJ and Matlab.

Results

As previous findings suggested (5), an increase in shear stress resulted in a decrease in NP uptake. Non-preconditioned cells exhibited over a 13-fold increase in NP uptake at 1 Dyne/cm^2 compared to at 8

Dyne/cm^2. No significant difference in NP accumulation was found between flow patterns in the non-preconditioned cells. However, the flow preconditioned cells showed a significant decrease ($p<0.001$) in NP uptake in areas of laminar flow when compared to that in the disturbed region.

Conclusions

These results indicate that NP uptake by endothelial cells is affected by the magnitude and profile of fluid flow, and that pre-exposure of the cells to flow alters the response. Changes in flow rate and flow pattern may cause physiological changes that affect NP uptake. In regions of laminar flow (and higher shear stress) such changes may include increased production of glycocalyx (a protective layer covering the cells) or a change in amount and composition of exposed extracellular matrix. Results from this study are being compared with those from zebrafish studies to determine if similar behavior is seen in living organisms. These findings warrant further exploration to determine the mechanisms of flow-modified NP uptake and to verify that *in vitro* flow models are more accurate predictors of NP behavior in biological systems than static assays.

References

1. Dobson, J., 2006. Drug Dev Res. 69: 55-60.
2. Chiu, J. and Chein, S., 2011. Phys Rev. 91: 327387. 3. Doiron, A., Clark, B., and Rinker, K.D., 2011. Biotech Bioeng, in press. 4. Toy, R. et al, 2011. Nanotech. 22. 5. Lin. A et al., 2010. J Biomat Med Res.93: 833-842.

A Posture Training Tool for Adolescents with Scoliosis

C Woloschuk[1, 2], E Lou[1, 2], V Zhao[1]

[1] Department of Electrical and Computer Engineering, University of Alberta, Edmonton, AB, Canada

[2] Glenrose Rehabilitation Hospital, 10230 111 Ave, Edmonton, AB, Canada T5G 0B7

Introduction

Adolescent Idiopathic Scoliosis (AIS) is a three-dimensional deformity of the spine affecting 2-3% of adolescents [1] and more predominately found in girls [2]. Adolescents with scoliosis may have abnormal curves on the sagittal, transverse or coronal planes. Adolescents with mild scoliosis normally receive no active treatments. From literature, intensive posture training may help adolescents adopt a more balanced and correct posture which can aid in preventing their curve from worsening by strengthening their back muscles [3]. This study reports on the development and test results of a wireless posture training device that will teach adolescents to maintain a better posture in the sagittal plane.

Methods

The posture training device is comprised of two sensor units, a USB wireless dongle, a harness and a Windows interface. Each sensor unit consists of a microcontroller with built-in 802.15.4 wireless transceiver, a 3-axis accelerometer, a 2-axis gyroscope and a lithium polymer battery. Sagittal plane angles were calculated from each sensor unit and transmitted to a PC wirelessly. Each sensor unit transmits an angle calculated using the accelerometer and an angle calculated using the gyroscope. An excessive drift prevention algorithm was developed for the gyroscope to maintain the accuracy of the angle calculations. The Windows program computes the final sagittal angle in real time based on a weighted average of the accelerometer and gyroscope angles. If the program detects the sagittal angle is above a user defined threshold, the program provides audio and visual feedback (on the PC) to

request the adolescent to correct their posture. Static and dynamic tests have been performed in a laboratory environment. A sensor unit was attached to a 360º rotated wheel to test the accuracy of the static measurements 3 times. A volunteer wore the device (two sensor units attached to the harness) and performed 4 motion tests in a camera capture motion (gait) laboratory. Wireless range and power consumption of the device were measured.

[3] E. Lou, et al., "Smart Garment to Help Children Improve Posture", Proceedings of the 28th IEEE EMBS Annual International Conference, New York
City, USA, Aug. 30-Sep. 3, 2006, pp. 5374-5377

Toward an Automatic ASPECTS Method: Classification of Ischemic Brain Tissue on Noncontrast Computed-tomography Images with Image Texture Analysis

QP Thomson, J Modi, SB Coutts, AM Demchuk, MD Hill, M Goyal, and JR Mitchell
Imaging Informatics Lab, Department of Diagnostic Imaging, University of Calgary

Results

Each sensor unit measures 57x36x14mm (LxWxH) and weighs approximately 30g. The accuracy of the angle in the static case was 1.68º±0.06º. The accuracy of the angle in the dynamic case was 2.28º±0.92º over 4 trials in the gait laboratory compared to the camera system (accuracy ±1º). The wireless range between the PC and the sensor unit is approximately 1m. Power consumption was 35mA during normal operations, allowing the device to run 21 hours on a single fully charged battery.

Conclusions

A posture training device was developed to aid in the treatment of AIS. The system provides visual and audio feedback when it detects improper posture in the sagittal plane and can be customized to the adolescent's needs. Future work will involve expanding the system to measure curves in the transverse and coronal planes.

References

[1] J. E. Lonstein and J. M. Carlson, "The Prediction of Curve Progression in Untreated Idiopathic Scoliosis during Growth", The Journal of Bone and
Joint Surgery, vol. 66-A, No. 7, pp. 1061-1071, 1984

[2] J. E. Lonstien, "Adolescent Idiopathic Scoliosis", Lancet, vol. 344, No. 8934, pp. 1407-1412, 1994

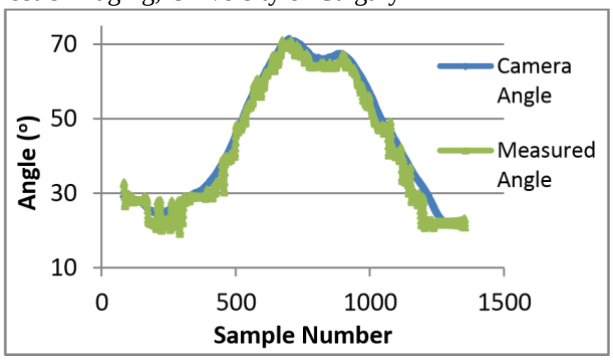

Fig. 1 Comparison of sagittal angle measurement in a dynamic case

Introduction

12km of myelinated fibers are destroyed each minute in an average ischemic stroke [1]; consequently, early intervention is critical to improve outcome. Unfortunately acute brain computed tomography (CT) images, which are used by stroke experts, only show very subtle changes in the area of ischemia [2]; this leads to increased variability by radiologists. We hypothesize that image texture analysis can identify subtle regions of ischemia found in early CT images.

Methods

In order to localize the ischemic regions, we rely on the comparison of the stroke-affected side of the brain to the contralateral healthy side. Radiologists use this technique in their diagnoses. This comparison is done with

image texture analysis, which has been previously used in the analysis of stroke [3].

Our texture analysis algorithm compares 3 image texture statistical values from spherical volumes on contralateral sides of the brain. The whole brain is scanned in this method. If the value collected is past a certain threshold, then all pixels within that volume are lightly coloured; overlapping spheres result in brighter colours, which indicate the areas that are more likely to be ischemic. This fuzzy data from the texture analysis is thresholded in order to create a binary map localizing the ischemia.

Numerical optimization is used to tune this threshold and other parameters to expert radiologists' results.

Analysis was performed on non-contrast CT scans obtained from 20 patients with middle cerebral artery strokes who presented at Foothills Medical Center in Calgary Alberta.

Preliminary Results

The figure shows how the early CT in panel A correlates to the results by texture analysis in panels B and C. The fuzzy data in panel B is thresholded to create the binary data in panel C. The texture analysis results visually correspond to the ischemic black areas in the follow-up CT in panel D.

Discussion

Preliminary results localizing subtle ischemia in early brain CTs are promising. The thresholding of the fuzzy data into a binary map resulted in clear contiguous regions. While some extraneous healthy regions were identified, they tend to be small and could be filtered out by the attending radiologist. The localization of ischemia is possible, but further parameter optimization and quantitative evaluation is needed.

References

1. Saver, J.L., *Time is brain--quantified.* Stroke, 2006. 37(1): p. 263-266.

2. Przelaskowski, A., K. Sklinda, and G. Ostrek, *Stroke Display Extensions: Three Forms of Visualization*, in *Information Technologies in Biomedicine*. 2008. p. 139--148.

3. Maldjian, J.A., et al., *Automated CT Segmentation and Analysis for Acute Middle Cerebral Artery*

Stroke. American Journal of Neuroradiology, 2001. 22: p. 1050-1055.

Figure

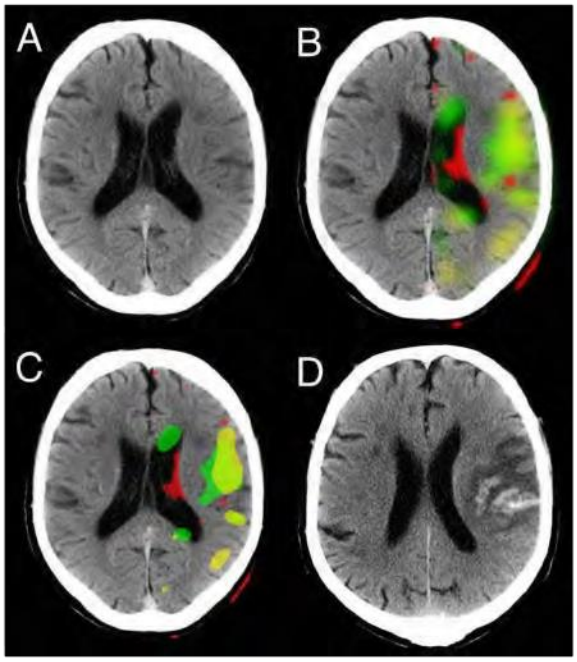

A) Early non-contrast CT brain image less than 1 hour after stroke onset, B) Ischemic regions identified by texture analysis are shown in green, yellow and red, C) Thresholded texture analysis data from panel B, and D) Follow-up non-contrast CT brain image from about 72 hours after stroke onset.

Difference in Active Joint Laxity between Dominant and Contralateral Knees of Healthy Individuals

[1] [1] [1]
Enns-Bray, W S; Bishop, E L; Mathison, C; Ronsky J L
University of Calgary, Calgary, AB

Introduction

Abnormal knee mechanics have been proposed as an initiating factor of OA[1]. Increased joint laxity can result from damage to the anterior cruciate ligament (ACL). Risk of developing OA has been shown to increase after ACL injury[2]. Current clinical joint laxity

tests are performed on patients in a state of muscle relaxation, thus are unable to correlate dynamic stability to functional outcome[3]. With motion analysis, joint laxity can be evaluated in-vivo during muscular activation. Active joint laxity can then be quantified with a finite helical axis (FHA) which can more effectively describe functional joint stability[4]. Before FHA can become clinically useful, the variability of active joint laxity in healthy individuals must first be understood. This study quantified and compared joint stability using four FHA parameters from 3D kinematic data. It was hypothesized that there would be no statistically significant differences in FHA parameters between dominant and contralateral knees.

Methods

Three healthy subjects (ages 18-40, 22±1) were recruited and tested at the McCaig Center for Bone & Joint Health. Three markers were placed on the thigh, shank, and foot. 3D kinematic data was captured at 120 Hz with an 8-camera high speed motion capture system (Motion Analysis Corp., California US). Subjects performed two functional tasks with each leg: A one-legged squat (Sq) and seated leg swing (Sw). Each motion was repeated five times per trail, and three trails total. Motion was further divided into flexion (F) and extension (E) phases. Four FHA Parameters were calculated: location, displacement, orientation, and dispersion. Data was analyzed within the range of 20-40º flexion, where full extension is 0º. Data from the best of three trails was averaged across all repetitions. A parametric, two tailed, paired t-test was used to look for significant differences ($p<0.05$) between groups for all four parameters. For the small sample size, a non-parametric, Wilcoxon signed ranks test was also performed to verify significance.

Results

FHA location and dispersion parameters more effectively describe relative motion between the tibia and femur, and thus stability of the joint. FHA location is the intersection of the instant axis of rotation of the knee and the midsagittal plane of the femur. The change in x & y coordinates of this intersection gave the relative motion between femur and tibia in that plane. The change of x, y cooridnates and the resultant displacement were compared separately with no significance detected between dominant and contralateral groups. Graphs of the changing FHA location which demonstrated these similarities were also produced. FHA orientation is the angle between the axis of rotation and the trans-epicondylar line of the femur. FHA dispersion is the angle between the mean FHA orientation over the entire trail and the instant FHA orientation at each time point, which is then averaged for each trail. This describes the relative angular motion between limb segments. FHA dispersion also showed no significant difference between groups.

Conclusions

No significant differences were detected between dominant and contralateral groups. This encourages future study of active joint laxity in healthy and ACL deficient subjects using FHA analysis to make quantified comparisons in functional joint stability.

References

[1] Berchuck M, et al. J Bone Joint Surg Am 72 (6), pp.871-877, 1990. [2] Kannus P Clinical rheumatology, 8(2), pp.251-60, 1989 [3] Eastlack ME Med Sci Sports Exerc 31 (2), pp.210-215, 1999. [4] Küpper JC Clinical biomechanics, 22(1), pp.1-13, 2007.

Table 1: p-values for FHA Location and Dispersion

Loc Δx	SqF	0.242	Loc Δy	SqF	0.365	Loc ΔR	SqF	0.613	Disp	SqF	0.109
	SqE	0.261		SqE	0.802		SqE	0.253		SqE	0.844
	SwF	0.254		SwF	0.452		SwF	0.696		SwF	0.531
	SwE	0.233		SwE	0.915		SwE	0.325		SwE	0.456

The Application of Prime Number-Sampling in Compressed Sensing Reconstruction

Estee Lee, Jerome Yerly, Richard Frayne
Biomedical Engineering, University of Calgary and Seaman Family Centre, Foothills Medical Centre
Calgary, Alberta

Introduction

Compressed sensing (CS) is a rapidly developing method for the reconstruction of signals/images using much fewer sample measurements than required in conventional imaging techniques [1]. This technique is especially useful for reducing medical imaging time in diagnostic imaging (*i.e.*, MR, CT, *etc.*). However, the application of CS requires that the image in *k*-space, the spatial-frequency domain, to be sampled in an incoherent manner [2]. Thus, a sampling system that is seemingly random, but more concentrated in the lower frequencies (where most of the image energy is contained) is potentially a good strategy. The sequence of prime numbers was chosen and implemented into a sampling scheme that fulfills this requirement for CS reconstruction in MR imaging applications.

Methods

The low-frequency components of a 256 × 256 test *k*-space data set were shifted to the center, *i.e.* 0 Hz at (128, 128); positive and negative frequencies and row indices were labeled outwards from this center point. The initial sampling scheme (*aka*, prime rows) sampled rows corresponding to primenumbered row indices. The second sampling scheme (prime odd rows) first assigned incrementing odd numbers to each row, *e.g.* row indices 1, 2, 3… were assigned 1, 3, 5…, respectively, for both positive and negative row indices. Only rows with assigned prime numbers were then sampled (Figure 1) and the image reconstructed using CS. Both sampling schemes were programmed to sample the middle three rows (*i.e.*, the lowest frequencies) in order to retain the strongest components of the image. For preliminary results, sampling was only applied in the vertical direction.

Results

The sequence of prime numbers is naturally more concentrated in the lower values, thus more sampling occurred in lower frequencies as required for CS. The prime rows scheme resulted in image aliasing artifacts in the vertical direction (Figure 2a) because only odd (prime) numbered rows were sampled. This effectively introduced sinusoidal frequency components, as the even-numbered rows were not acquired, resulting in significant ghosting artifacts. The second sampling scheme sampled an incoherent mixture of both even- and oddnumbered rows, resulting in a reconstructed image with much better quality (Figure 2b).

Conclusions

The random nature of prime numbers met the requirements for CS, and was implemented into a sampling scheme that resulted in successful image reconstruction. Further development of this design has the potential to be applied in clinical settings to drastically reduce medical imaging time.

References

[1] Lustig, M., et al. (2007). Sparse MRI. Magnetic Resonance in Medicine, 58 (6), 1182–1195.

[2] Candes, E., et al. (2006). Robust uncertainty principles. IEEE Transactions on Information Theory. 52: 489-509.

Figures

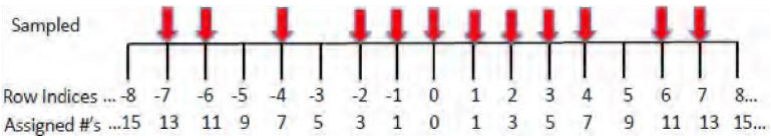

Figure 1. The initial sampling scheme sampled rows with (the absolute values of) row indices corresponding to prime numbers. The second sampling scheme sampled rows that had assigned labels corresponding to prime numbers, shown by the red arrows.

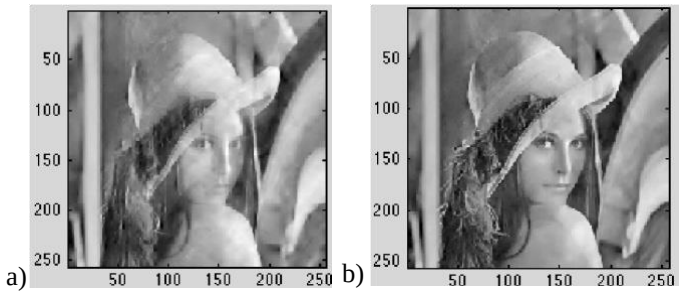

Figure 2. CS reconstruction of lena.jpg after sampling in *k*-space of the prime numbered rows with respect to a) row indices and b) odd-number assignments.

rate of 0.66 Hz can be achieved with a 64 ×

A 3D Real-Time Magnetic Resonance Imaging Application to Visualize Contrast Inflow

David Adair, M Ethan MacDonald, Richard Frayne
Department of Electrical and Computer Engineering, University of Calgary, Calgary, AB, Canada
Seaman Family MR Research Centre, Foothills Medical Centre, Calgary, AB, Canada

Introduction: Real-time magnetic resonance (MR) imaging has been proposed as a method for device tracking and visualization by several research groups[1,2]. Currently, the gold standard imaging modality for clinical real-time applications is X-ray imaging, as it has higher resolution in both space and time. MR imaging has several advantages over Xray imaging, including: 1) Superior contrast of soft tissue, 2) potential for 3D imaging, and 3) absence of ionizing radiation. Challenges with real-time MR imaging include design of fast acquisitions and efficient processing, which has led to most real-time MR implementations to be strictly 2D. In this study we design a hardware configuration and software application for fast MR image reconstruction in real-time to be viewed on the MR console, we then time the application imaging at various volume sizes and report the results. It is our hypothesis that a frame 64 × 8 acquisition matrix, to visualize contrast inflow.

Methods: Experiments were performed with a 3 T MR scanner (Discovery MR 750, General Electric Healthcare, WN, USA). A hardware solution was assembled from set data processing requirements. To maximize compatibility with the GE console computer, the computer was configured with a UNIX operating system (OpenSUSE 11.4 32 bit edition, NOVELL, MA, USA). The application was run on the console computer via X11 display. Description of hardware is in Table 1. A software application using the GE raw data server feature was written in C++ using open source libraries, including: the Qt4.7 framework, Fastest Fourier Transform in the West (FFTW)[3], and Visualization Toolkit (VTK). Raw volume data was acquired and processed in real-time for several matrix acquisition sizes. The time

required to run each processing stage was measured. A flow phantom was used to image contrast inflow.

Results: Stage timing is shown in Fig 1. Contrast inflow within a flow phantom was imaged at a resolution of 64 × 64 × 8 at 0.66 Hz. Images of a contrast agent injection are shown in Fig 2 with the time stamp of when they were collected.

Conclusions: Fundamentally, real-time MR imaging is limited by the underlying physics and acquisition. We demonstrate here a method of fast image reconstruction for realtime applications, where feedback may be required for the operator. The timing of processing stages gives a state of the art lower bound for image reconstruction speed. Contrast inflow was visualized at 0.66 Hz, with a 64 × 64 × 8 acquisition matrix. A faster frame rate for the demonstrated resolution should be achievable with additional image acceleration techniques, such as: random under sampling, parallel imaging or compressed sensing.

References: [1] Gobbi, *et al.*, Medical Image Computing and Computer-Assisted Intervention. Springer Berlin/Heidelberg, 2000.

[2] Quick, *et al.*, MRM, 2003 [3] Fringo, *et al.*, IEEE Signal Processing, 1998

Table 1 – Hardware Configuration

Component	Specification
Processor	3.4 GHz 8 Core Intel i7
RAM	8 GB 1866 MHz DDR3
Graphics Card	NVIDIA GTX 570
Hard Drive	Intel 510 SSD 120 GB

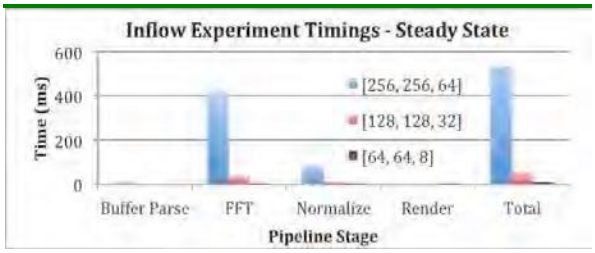

Figure 1 – Pipeline Stage Timings

Figure 2 – Contrast Inflow Frame Timing

Numerical Analysis of Augmented Locking Plate Fixation Repair for Proximal Humeral Fractures

Farhana Begum, Muntaseer Kainat, Samer Adeeb, Jason P. Carey

Introduction

Augmented locking plate fixation is an improved treatment technique for proximal humeral fractures, especially in osteoporotic bone without medial column support. Previous biomechanical studies of our research group have compared the locking plate fixation alone vs. the locking plate fixation with fibular graft, for both the static and the cyclic loading conditions (Roxanne et al, 2011; Mathison et al, 2010) and their results suggest that fibular graft can increase the stiffness and stability of the implant systems. However, comprehensive experimental research using cadaveric specimens may not always be possible due to various reasons such as scarcity of samples, increased cost, complex experimental setup etc. Under these circumstances, the powerful finite element analysis can help for pre-clinical evaluation of the response of the different implant systems (Huiskes and Chao, 1983). The objective of this study is to develop a finite element model to simulate the experiment under the static loading condition, and explore how closely it represents the actual behavior of the specimens.

Methods

We used the digital images (MRI) of a humeral head to create its complex geometry. To create the 3D model of the humerus, fibular graft and the locking plate fixation, MIMICS, Geomagic Studio12 and Solid Works software were used. To replicate the experiment, a 10 mm osteonomy was created in the surgical neck. ABAQUS software was used for Finite Element Analysis where all

solid parts were assembled according to the experiment. Two models were developed for two types of implant systems and then material properties and mesh were assigned. Appropriate boundary conditions and loads were provided to simulate the experiment for the static loading conditions.

Results

The FEA results showed that the augmented construct can increase the initial stiffness 6.22 times. This is comparable to the experimental study results where the augmented construct increase the initial stiffness 3.84 (SD 1.92) times. Augmented construct can increase the required load to develop damage in the bone material, 1.81 times for tension and 1.88 times for compression.

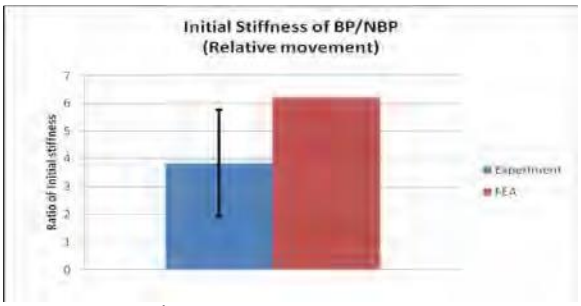

Figure 1: Ratio of initial stiffness

Conclusions

The finite element analysis results identified the area close to the screw holes in the humeral head to be the weakest point of the construct which is similar to the results of the experimental study. Both the FEA and experimental results showed that the augmented fixation can increase the initial stiffness. Figure 1 compared the ratio of initial stiffness.Comparing the experimental and simulation results, we can conclude that the finite element model can mimic the behavior of the implant systems for static loading conditions.

References

1. Mathison C., Chaudhary R., Beaupre L., Reynolds M., Adeeb S., Bouliane M. Biomechanical analysis of proximal humeral fixation using locking plate fixation with an intramedullary fibular allograft. Clinical Biomechanics 2010; 25(7): 642-46.
2. Chow R., Begum F., Beaupre L. Carey J.P., Adeeb S., Bouliane M. Proximal Humeral Fracture Fixation:Locking Plate Construct +/- Intramedullary Fibular Allograft. JSES, 2011 (accepted).
3. Huiskes R., Chao EY-S. A survey of finite element methods in orthopaedic biomechanics: the first decade. J. Biomechanics 1983; 16: 385-409.

Computer Modeling of Arrhythmia Vulnerability in Diabetic Cardiac Tissue

Amin Ghazanfari[1], Militina Gorobets[1] and Anders Nygren[1,2]

Electrical and Computer Engineering[1], Center for Bioengineering Research and Education[2] – University of Calgary

Introduction

Patients with diabetes are considered at risk of arrhythmias or other cardiac problems. Arrhythmias can be generated due to different parameters variations such as opening and closing of ATP-dependant potassium channels (I_{KATP}), changes in gap junction locations within the cell, and different extracellular potassium concentrations ($[K^+]_o$).

Gap junctions are affected through connexin 43 (Cx43) which is a major component of gap junctions. Cx43 lateralization represents the migration of gap junctions from the ends of the cell to the sides, affecting wave propagation in the tissue. These changes can be arrhythmogenic[1].

In this study, we used a mathematical model of both healthy and diabetic tissues to investigate different aforementioned factors. We found that diabetic tissue with lateralized functional gap junctions are at the lowest risk of reentrant arrhythmias.

Methods

The myocyte model for healthy and diabetic cells were implemented from models by *Pandit et al*[2,3]. Simulations were done for

5.4mM and 9.0 mM values of $[K^+]_o$ for a 1cm by 1cm piece of tissue. Cx43 lateralization was modelled by changing longitudinal and transverse conductances of the tissue (g_L and g_T). Three variations of Cx43 were used in diabetic model simulations: normal, lateralized functional, and lateralized non-functional gap junctions (g_L/g_T = 9/1, 5/5, and 5/1 respectively).

An S1-S2 protocol was used to generate reentrant activity. S2 occurs a certain time after S1. The delay between S1 and S2 is noted. Window of vulnerability (WoV) is defined as an interval of time delay between S1 and S2 when reentry happens.

Results

Action potential duration (APD) is prolonged in the diabetic tissue. Longer APD results in longer refractory period so lower risk of reentrant activity. I_{KATP} results in significant decrease in APD which increases the chance of getting reentry. As depicted in figure 1, there are larger WoVs in the presence of I_{KATP}. A large WoV represents a greater chance that the tissue will develop reentrant activity. The diabetic tissue with functional lateralized gap junctions (50%-50% split) has the smallest WoV in both presence and absence of I_{KATP} while the diabetic tissue with non-functional Cx43 lateralization (50%-10% split) is at the great risk of reentry arrhythmias. One possible reason is that anisotropy provides opportunities to unidirectional conduction block and hence facilitates reentry, while isotropy has the opposite effect[4].

Conclusions

The result of this study has shown that healthy tissue may not be an advantage in comparison to the diabetic tissue in possibility of reentrant arrhythmias. Lateralization of Cx43 presents an opportunity for creation of isotropic tissue that has smaller risk of developing reentry activity.

References

[1] *J Physiol* 580.2, 543-560, 2007.
[2] *Biophys J* 81, 3029-51, 2001. [3] *Biophys J* 83, 832-841, 2003.
[4] *APJ Heart* 300, 271-278, 2010.

The Principle of Superposition During Lifting of an Object Exerting Two-Dimensional External Torques

Jason W. Robertson B.Sc. and Jamie A. Johnston Ph.D.
Faculty of Kinesiology, University of Calgary, 2500 University Dr. NW, T2N 1N4

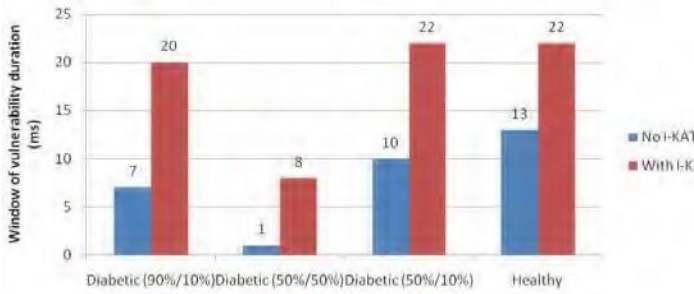

Fig. 1: Window of vulnerability duration for different cell types.

Introduction

Multi-digit grasping requires the fine coordination of many muscles across many joints. While this introduces many redundancies, the central nervous system tends to select from families of solutions, or synergies (1). One way to study these is the application of the superposition principle, which suggests that grasp can be broken into small, independently-controlled elements which sum to produce a whole action (2). Previous studies have shown that grip and torque are controlled separately when lifting an object exerting a one-dimensional moment (3); our purpose was to determine if this principle held when lifting an

object exerting a two-dimensional moment. We hypothesized that grip and torque control would remain separate, and that the principle of superposition would hold when lifting against a two-dimensional moment.

Methods

Ten healthy volunteers (age 25.6±5.4 yr, mean±SE) participated in this study. The experimental apparatus consisted of an instrumented handle attached to a round base, under which one of two weights could be hung on one of nine marked points around a ring (Fig. 1). The 18 centre of mass conditions were presented in pseudorandom order, in blocks of seven trials. In each trial, subjects lifted the object, held it in vertical orientation for several seconds, and then lowered it. The components of the moments about each axis were calculated as functions of finger or thumb forces. Principal components analysis (PCA) was then used to determine if variables related to grip force appeared on separate components from variables related to moment generation. PCAs were run for groups of variables influencing M_x, M_y, and M_z, as well as a collection of all calculated variables (M_{3D}).

Results

Analysis of the M_x and M_y groups showed grip force variables appearing on separate components from moment variables. Analysis of the M_z group did not contain grip force variables; thus, their results did relate to superposition. Analysis of M_{3D} showed not only a separation of grip force and moment variables, but a separation of M_x, M_y, and M_z variables from one another.

Conclusions

Our data show that grip and torque were controlled separately when lifting an object exerting a two-dimensional moment. Thus, we conclude that the principle of superposition holds under this condition.

References

(1) Santello M, Soechting JF. Force synergies for multifingered grasping. *Exp Brain Res* 133: 457-467, 2000.

(2) Zatsiorsky VM, Latash ML, Gao F, Shim JK. The principle of superposition in human prehension. *Robotica* 22, 231-234: 2004.

(3) Shim JK, Latash ML, Zatsiorsky VM. Prehension synergies: trial-to-trial variability and principle of superposition during static prehension in three dimensions. *J Neurophysiol* 93: 3649-3658, 2005.

Figures

Fig. 1: Experimental apparatus.

A Way to Seek the Bijective Mapping of Morphological Changes was

Amin Komeili[1], Samer Adeeb[1] and ,-Marwan El-Rich[1]

1)Civil & Environmental Eng Dept. University of Alberta, Edmonton, AB

Introduction

In order to accurately model morphological changes associated with growth, it is imperative to develop a technique that is able to predict the mapping between the different geometric stages of growing objects. For example, investigating the spinal deformation by measuring the magnitude of the strains in the scoliosis patients could be accomplished by finding the mapping function between the healthy and patient spine geometry (Figure 1). The purpose of this study is to find the appropriate mapping function between to stage of the configuration by minimizing adopted objective function. The geometrical change can be predicted by seeking some certain optimization functions. In order to find the optimum mapping, an objective function was considered base on the certain criteria and minimized respect to unknown constants. The developed method was employed on the parametric curves and accuracy of the method was investigated.

Methods

In order to describe planer curves in original and deformed configuration the parametric form employed as [1]:

$$x = x\,t(\,),\quad y = y\,t(\,) \qquad t_0 \le \le t \qquad t_n \qquad (1)$$

$$X\,X\,T = (\,),\quad Y\,Y\,T = (\,) \qquad T_0 \le \le T\,T_n \qquad (2)$$

Where, t and T are the independent parameter in the original and deformed configurations. Assuming the two stages of the growth are known, the question becomes finding the bijective mapping between the two sets. The following discusses some possible criteria the mapping may base on: Minimize the Strain, the Curvature and a combination of Strain and Curvature. The optimization functions for different the criteria are:

$$Obj_{length} = \int (ds - dS)^2 \qquad (3)$$

$$Obj_{curvature} = \int (d\kappa - \mathrm{K}d\,)_2 \qquad (4)$$

$$Obj_{comb} = C_c \times Obj_{curvature} + C_l \times Obj_{length} \qquad (5)$$

Results

The accuracy of the method was examined by generating two curves. A combination of compression in x-direction and 45 degrees rotation considered for the deformed curve. The exact solution T= tan(t) was employed as the mapping function. A third order polynomial function was considered for mapping function with unknown constants. The final forms of the equations in original and deformed configuration are:

$$\begin{cases} x = t - \pi/3 \\ y = \cos\left(t + \pi/3\right) \\ X = \dfrac{\cos 45 \times \left[\tan^{-1} T + \pi/3\right] - \sin 45 \cos 2 \tan\left[\tan^{-1} T + \pi/3\right]}{2} \\ Y = \sin 45 \times \left[\tan^{-1} T + \pi/3\right] + \cos 45 \cos 2\left[\tan^{-1} T + \pi/3\right] \end{cases} \qquad (6)$$

The accuracy of the method has been investigated in Table (1) compare with the exact solution T=tan (t).

Table 1- The predicted third order polynomial mapping function using different criterion.

Criteria	Final Form of Mapping Function	$Error = \int (\tan(\,)t - T\,dt)$
Obj_{curvat}	$T\,t(\,) = 3.5t^3 - 19.9t^2 + 37.9t - 20.5$	0.480
Obj_{length}	$T\,t(\,) = 0.37t^3 - 0.13t^2 + 1.24t + 0.14$	0.274
Obj_{comb}	$T\,t(\,) = 0.75t^3 + 0.03t^2 + 0.83t - 0.03$	0.06

Conclusions

Based on Table(1), it is apparent that , Obj_{Comb} leads to more accurate approximations for the mapping function. This criterion predicted the tending of the living organs to grow or deform uniformly by minimizing strain, and try to avoid large deformation in shapes during deformation by minimizing the curvature.

References

1. Coolidge, J.L. "The Unsatisfactory Story of Curvature". The American Mathematical Monthly, Vol. 59, No. 6 (Jun. - Jul., 1952), pp. 375–379

Figures

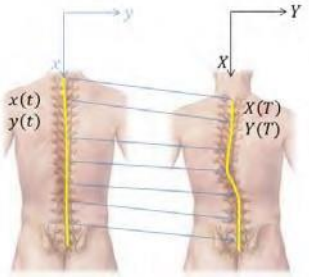

Figure 1-Application of the method in scoliosis

A Variable Resistance Wheelchair Ergometer for Propulsion Biomechanical Studies

Jiajie Wu, Mojtaba Azadi, Liping Qi, Martin Ferguson-Pell
Faculty of Rehabilitation Medicine, University of Alberta, Edmonton, Alberta, Canada, T6G2C6
AHFMR Bone and Joint Health Team Grant

Introduction

Laboratory studies investigating the biomechanics of wheelchair propulsion have either employed treadmills or roller ergometers[1, 2]. In the "real-world", the wheelchair occupant has to generate propulsion forces that overcome rolling resistance and inertia associated with the mass of the user and wheelchair. Rolling resistance is relatively insensitive to the speed of propulsion, however the forces needed to overcome inertia are proportional to the acceleration of the body and wheelchair system. "Static" mechanisms have been used to represent rolling resistance on typical propulsion surfaces, but a method to include the inertial component has not been reported for treadmills or roller ergometers. **Hypothesis:** By dynamically adjusting resistance applied to rollers, a laboratory ergometer can represent the biomechanics of "real-world", variable rolling resistance, straight-line wheelchair propulsion. **Methods**

A double roller ergometer was constructed and incorporated a belt braking system attached to pneumatic actuators. The system was connected to an A/D converter (DT304, Data Translation Inc., Marlboro, MA, USA) and controlled by a customized LabView (National Instrument Corp., USA) program. An algorithm was developed that controlled the roller resistance in response to the instantaneous roller acceleration generated by the occupant‟s propulsion forces on the wheelchair handrim. The total resistance of the rollers was therefore the combination of: roller inertia, known rolling resistances of a „real world‟ scenario, and the simulated inertia of the wheelchair occupant and wheelchair, calculated in real time.

To validate the system, 25 able-bodied participants pushed a wheelchair on a „real world‟ surface comprising 8m of medium pile carpet and 8m Astroturf as well as on the ergometer. Propulsion biomechanics parameters (including propulsion moment, cadence, push length and average velocity) were collected using two SmartWheels (Three Rivers Inc., Mesa, AZ, USA). The test was then repeated with ergometer settings that simulated the 2 real world surfaces. The ergometer system was operated at 50Hz. A visual display provided a simulation of the real world experience when using the ergometer. **Results**

Data from one participant has so far been analyzed in detail. Biomechanical variables were compared between real world and ergometer simulated settings. There is a difference of 13 to 20% in the propulsion moment applied to the forward direction of wheelchair comparing the „real world‟ and simulated environments and there was less than 0.1% difference between the performance of participant in the two environments in terms of push length, push frequency and average velocity. Data from the other 24 participants is currently being processed.

Conclusions

Our results so far show that the participant performed similarly in the „real world‟ and on the ergometer. By adding the inertial component of propulsion, the ergometer can effectively represent „real world‟ propulsion of the wheelchair user for straight line pushing on surfaces with

differing rolling resistances. In order to better simulate the inertial component, we anticipate that better correspondence in propulsion forces will be achieved if the sampling rate of ergometer system is increased thereby reducing lag in the resistance response.

References

1. Veeger, H.E., L.H. van der Woude, and R.H. Rozendal, *A computerized wheelchair ergometer. Results of a comparison study.* Scand J Rehabil Med, 1992. **24**(1): p. 17-23.
2. Kwarciak, A.M., et al., *Comparing handrim biomechanics for treadmill and overground wheelchair propulsion.* Spinal Cord, 2011. **49**(3): p. 457-62.

STRUCTURAL AND MECHANICAL CHARACTERIZATION OF THE ATRIA

Nathanael L. Lee, Chiara Bellini, Elena S. Di Martino
Department of Civil Engineering and Centre for Bioengineering Research and Education
University of Calgary - 2500 University Drive NW, Calgary, Alberta

Introduction

Most pathologies affecting the heart develop because of the effects of biochemical, electrical and mechanical changes. Hence, the ability to measure and model the structural and mechanical properties at different length scales may provide useful insights on disease onset and progression and suggest possible therapies. This study reports on polarized light microscopy (PLM) experiments and planar biaxial tests that were performed to investigate the arrangement of fibers and the passive mechanical behavior of tissues in the atria.

Methods

Tissues from porcine atria proved to be excessively thick to be imaged with PLM. Based on inter-species similarities in the atrial fiber arrangement [1], specimens from healthy New Zealand rabbits were used instead. Five regions were identified on the atria: the anterior and posterior portions of the left atrium, the body of the right atrium, the left (LAA) and right atrium appendages. Hydrated tissue samples were illuminated with circularly polarized light while the transmitted light was analyzed with a computer-controlled liquid crystal analyzer. The output images showed in a color scale (0-255 in RGB) the retardance azimuth, which coincides with the principal axis of the bundles in structures including highly organized collagen fibers [2]. Tissue samples from Yorkshire pig atria were excised consistently with the rabbit atria specimens and tested on a planar biaxial device, following a protocol proposed by Sacks [3]. Based on mechanical response and microstructure, the experimental data were fitted to four constitutive models, which mathematically describe the mechanical behavior of the atrial tissue and can be used to solve computational models of the atrium. In particular, two isotropic (Neo-Hookean and Ogden) and two anisotropic (Fung and microstructurallymotivated, Holzapfel-like) models were chosen, with the main difference relying on the ability of the last two models to account for a direction-dependent mechanical response.

Results

Two orthogonal families of fibers were observed on all the atrial specimens that were analyzed under polarized light (Fig. 1). Mechanical test results recorded a nonlinear elastic and anisotropic behavior.

Consistently, the isotropic models provided the poorest fitting quality (average R^2=0.685). Accounting for the fiber-induced anisotropy brought average R^2=0.828 for the microstructurally-motivated and R^2=0.943 for the Fung model.

Conclusions

The process of mechanical characterization and modeling benefits from the knowledge of the fiber arrangement, as this guides the excision of the specimens for the mechanical tests

in a way that is consistent with the microstructure and it provides the anatomical foundation for the development of meaningful material models.

References:

1. Papez, J. W. Heart musculature of the atria. Am. J. Anat. 27:255-285, 1920
2. Xia, Y. et al. Quantitative *in situ* correlation between microscopic MRI and polarized microscopy studies of articular cartilage. Osteoarth. Cartilage 9:393-406, 2001.
3. Sacks, M.S. Biaxial mechanical evaluation of planar biological materials. J. Elast. 61:199-246, 2000.

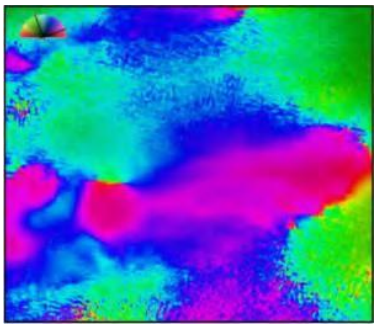

Figure 1 - PLM image for a specimen from LAA

Soft tissue vibration characteristics while treadmill running in shoes and barefoot

Hendrik Enders[1], Vinzenz v. Tscharner[1], Benno M. Nigg[1]

[1] Human Performance Lab, University of Calgary, 2500 University Dr NW, Calgary, AB, Canada, T2N 1N4

Introduction Soft tissue vibrations can be initiated by a sudden impact or a collision between two objects (e.g. foot with the ground). Inertial sensors such as accelerometers can be used to measure these vibrations. The concept of muscle tuning involves the idea that vibrations of soft tissue compartments are damped by the preactivation of muscles [1]. The current study investigates how the damping coefficient changes during treadmill running with shoes and in a barefoot condition.

Methods Muscle vibrations were measured from the soft tissue overlying the muscle belly of the medial gastrocnemius using a skin-mounted accelerometer. Acceleration data was recorded at a sampling frequency of 2400Hz using a 12-bit data acquisition system. Eight healthy male subjects performed treadmill running at a speed of 3.5m/s in a barefoot condition as well as with their own comfortable running shoes. Prior to data collection the subject was given a three minute warm up period in order to familiarize with treadmill running. 20 steps were collected for each subject in both conditions. A wavelet transform of the signal was computed using non-linearly scaled wavelets [2]. Subsequently the frequency range suitable for the vibrations was further analyzed and the damping coefficient was calculated from the exponential decay within this frequency range of 8 – 16Hz.

Results Analysis in the frequency domain revealed that the peak average muscle vibration occurred at 13.5Hz ± 1.37Hz. All subjects showed significant differences between the two tested conditions ($p < 0.5$) whereas six subjects showed higher damping coefficients while running barefoot and two subjects showed higher values for the shod condition. Comparing the two conditions an average difference of $2.15s^{-1} \pm 1.4s^{-1}$ was found in the damping coefficient of the medial gastrocnemius.

Conclusions The results from this study did not display consistent results for the damping coefficient of the two conditions. Related to soft tissue vibrations the results from this study indicate two possible explanations for this inconsistency. One possible explanation involves a more passive mechanism where changes in the length of the muscle tendon unit occur due to altered kinematics in barefoot running that may change the damping coefficient within a muscle. It may also be a more active mechanism based on changes in muscle activation patterns in order to damp vibrations adequately.

This more active mechanism would imply a strategy which is used by the body to control vibrations within a soft tissue compartment. In order to review these hypotheses, further analysis is needed including EMG measurements. Future studies should focus on investigating the change in muscle activity as vibrations are changed due to different running styles, input signals and sports equipment (e.g. compression apparel).

References

[1] Nigg, B.M., Clin J Sport Med 11, 2-9, 2001

[2] von Tscharner,V., J Electromyography Kinesiol 10,433–445, 2000

Figures

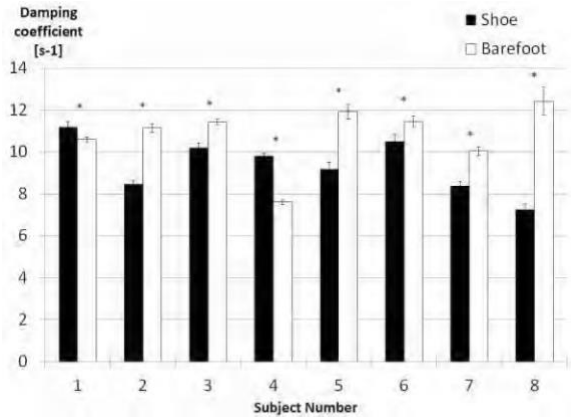

Figure1 Average damping coefficient for 8 subjects while running in shoes (black) and barefoot (white).

The influence of calcaneal motion and tibial torsion on leg axial rotation

Michael G. Chizewski, Kaylynn S. Shewaga, Samantha N. Porter, and Loren Z. F. Chiu
University of Alberta, Edmonton, AB, Canada

Introduction

The sub-talar joint is often defined as a mitered-hinge. In theory, calcaneal eversion will result in internal rotation of the leg. Preliminary analyses of 3D leg rotation during squatting and jumping tasks suggest two groups – one where the leg internally rotates, and the other with externally rotating legs. A hypothesis to explain the difference in leg rotation is tibial torsion angle (Fig. 1). Tibial torsion differences have been reported between men and women [1] and may influence gait mechanics [2].

The purpose of this research was twofold. To study the influence of calcaneal motion on leg rotation; and to examine whether tibial torsion could explain the differences between internal and external leg rotation.

Methods

Participants included healthy adult women (n=25) and men (n=23). Twenty-two retroreflective markers (in a 6 degree of freedom formation) were recorded using a 6-camera motion capture system (Qualisys) at 120 Hz.

Participants flexed at the hip, knee and ankle to a position of maximum dorsiflexion. The leg and calcaneus were modeled as rigid segments in Visual3D software. Rotations of these segments were determined relative to the lab using a ZYX Cardan sequence [3]. Participants were grouped by whether their leg internally or externally rotated. Tibial torsion and calcaneal motion were compared using unpaired two-tailed *t* tests.

Results

Calcaneal anterior tilt and external rotation were not significantly different between the two groups. Significant differences were found for calcaneal eversion, with externally rotating legs showing greater eversion than internal rotators (6.60±2.47° vs. 4.66±2.46°).

For the legs that internally rotated, torsion angles were 11.56±6.24° and 11.65±5.56° in left and right limbs respectively. For legs that externally rotated, torsion angles were measured at 19.93±9.57° and 18.89±4.03°. Significant differences were noted for left and right tibial torsion angles

Hybrid Hydrogel/Polymer Scaffolds for Cartilage Tissue Engineering Applications

J. Little, W. K. Kulyk, and X. B. Chen
University of Saskatchewan; Saskatoon; Saskatchewan

comparing internal versus external rotators.

Conclusions

The association between calcaneal eversion and eternally rotating legs directly opposes the mitered-hinge theory. The direction of axial leg rotation will affect loading on the structures of the knee and the hip [2], and rotation of the tibia has been implicated as a factor in lower extremity injuries. Research of injuries where tibial rotation is a factor should consider tibial torsion angle as a nonmodifiable risk factor.

The study presents an anatomic factor that influences leg rotation. It is important to study how tibial torsion influences leg and foot mechanics in non-weight-bearing tasks, and during the transition to weight-bearing tasks such as gait.

References

1.Yoshioka Y, et al. *J Orthop Res* **7**, 132-137, 1989.

2.Hicks, J, et al. *Gait Posture* **26**, 546-552, 2007.

3.Baker, R. *Gait Posture* **13**, 1-6, 2001.

Figures

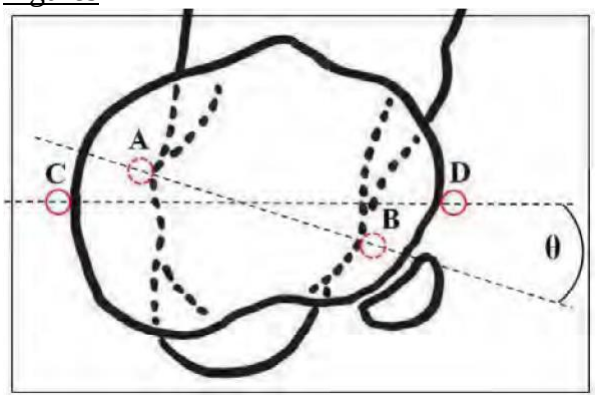

Fig. 1: Tibial torsion angle (θ) (tibia superior view) A-medial malleolus; B-lateral malleolus; C-medial tibial condyle; D-lateral tibial condyle.

Introduction

If artificial cartilage constructs can be created with suitable biomechanical properties, it would help alleviate the suffering of the millions of North Americans living with osteoarthritis. Many of the tissue engineered cartilage constructs currently available lack the chemical stimuli, cellfriendly environment, and/or mechanical strength needed for use in joint cartilage repair. The goal of our research is to test the efficacy of hybrid scaffolds comprised of a solid synthetic polymer framework impregnated with a fibrin/alginate hydrogel containing hyaluronic acid (HA) and/or chondroitin sulphate supplements (CS).

Methods

Hydrogel with hyaluronic acid and/or chondroitin sulphate: Porcine chondrocytes were seeded in a fibrin-alginate hydrogel (HG) at $5x10^6$ cells/ml density. The HG was supplemented with 0.1 mg/ml HA alone, 0.1 mg/ml CS alone, both HA and CS, or neither additive. After 10 days of culture, the HG was analyzed by a modified 1,9-dimethylmethylene blue (DMMB) method [1, 2] to quantify glycosaminoglycan deposition by chondrocytes. A fluorometric DNA assay using Hoechst dye was used to determine viable cell numbers. Some hydrogels were cryogenically sectioned and stained with Hoechst dye to visualize the cell distribution within the hydrogel, or immunostained to detect accumulation of cartilage-specific type II collagen.

Fabrication of solid polymer framework:
To fabricate the solid framework, poly(lactic-co-glycolic acid) (PLGA) was solubilized in chloroform and mixed with iron oxide nanopowder. The slurry was loaded into a scaffold fabrication system [3], extruded in strands and assembled layer by layer into a mesh-like framework.

DOES KNEE EXTENSOR MUSCLE IMBALANCE CAUSE CHANGES IN PATELLAR TRACKING?

Andrew Sawatsky, Tim Leonard, Walter Herzog
University Of Calgary

Results

Our modified DMMB assay showed good linearity. Preliminary results suggest that both CS and HA supplements stimulate chondrocyte proteoglycan production (2.1fold increase for CS, and 1.7-fold increase for HA), but their effects are not additive. In these experiments, there were significantly fewer cells in HA supplemented hydrogels than in non-supplemented control gels. Hoechst staining confirmed that cells were proliferating throughout the gel, and immunostaining revealed the deposition of type II collagen fibrils around and between the embedded chondrocytes. A composite PLGA/iron oxide scaffold was fabricated having a repeatable, overhanging 3dimensional structure. Hoechst staining shows that cells are capable of surviving on the solid scaffold material.

Conclusions

Chondrocytes can be successfully cultured in hydrogels supplemented with CS and/or HA. The results of the DMMB assay and the type II collagen immunostaining suggest that the cells are producing the appropriate extra cellular matrix components and, therefore, retaining their chondrogenic phenotype. In addition, it appears that both CS and HA have effects on both chondrocyte proliferation and proteoglycan synthesis. Future work will involve impregnating the hydrogel into the solid scaffold framework and to perform *in vitro* and *in vivo* tests for cartilage repair.

References

1. Enobakhare, B.O., Bader, D.L., and Lee, D.A. Analytical biochemistry **243**, 189, 1996.

2. Müller, G., and Hanschke, M. Connective tissue research **33**, 243, 1996.

3. Chen, X.B., Li, M.G., and Ke, H. Journal of manufacturing science and engineering **130**, 021003, 2008.

Introduction

Patellofemoral pain syndrome (PFPS) is one of the most common knee disorders. The main region of pain is the lateral aspect of the patellofemoral joint. Force imbalance in the knee extensor muscles has been associated with changes in patellofemoral tracking (*1*) and is suspected to cause PFPS. Weakness of the vastus medialis (VM) relative to the vastus lateralis (VL) is the usual imbalance associated with PFPS (*2*). The purpose of this study was to create an animal model of quadriceps muscle imbalance and to test the effect of a VM/VL imbalance on patellar tracking. The muscle imbalance was produced by eliminating the function of VM by cutting it in mid-belly. We hypothesised that transection of VM causes the patellar tracking to shift laterally in the femoral groove.

Methods

All experiments were performed on knees (n=9) of skeletally mature New Zealand White rabbits. Patellar tracking was recorded with a high speed camera at 200Hz and a spatial resolution of 80µm. Two markers were placed on the patella and two further markers on the femur via bone pins, to record frontal plane movements of the patella relative to the femur. The rabbits were fixed in a stereotaxic frame, while the tibia was attached to a lever arm connected to a motor allowing for knee extensions and flexions between 30° and 90°at an angular speed of 40°/s. Movements of the patella relative to the femur were recorded for passive and active concentric and eccentric knee extensor contractions, before and after VM transection.

Results

The primary result of this study was that patellar tracking was shifted laterally by 0.2 ± 0.2mm and 0.1 ± 0.2mm for concentric and eccentric

contractions, respectively following VM ablation. However, and to our great surprise, patellar tracking occurred much more laterally for the passive compared to the active contractions and these differences were in the range of 23mm (Figure 1). Since VM ablation caused a loss in average knee extensor force of 19%, we speculate that the lateral shift of patellar tracking following VM ablation was not so much caused by the lack of medial pull from the VM, but rather, was caused by the decrease in overall knee extensor force.

Conclusions

While the removal of the VM appeared to cause a small lateral shift in patellar tracking, we hypothesize that this the lateral shift was caused by the loss in knee extensor force following VM ablation, rather than a lack of medial pull by the VM. This hypothesis will need testing by repeating these experiments with careful matching of the knee extensor forces prior to and following VM ablation.

References

1. N. A. Wilson, J. M. Press, J. L. Koh, R. W. Hendrix, L. Q. Zhang, *J Bone Joint Surg Am* **91**, 558 (2009).

2. F. J. Lieb, J. Perry, *J Bone Joint Surg Am* **50**, 1535 (1968).

Figures

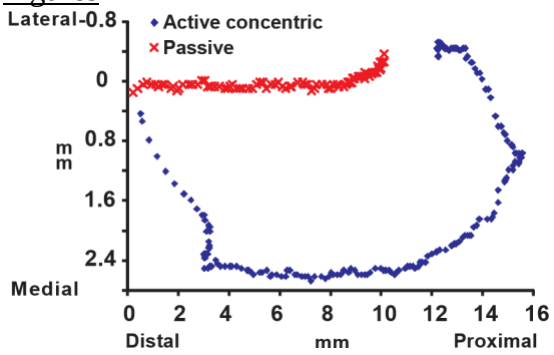

Figure 1: Medial-lateral (vertical axis) and distalproximal displacement [in mm] of the patella relative to the femur during an active (blue) and a passive (red) knee extensor contraction.

Extending Purkinje System Model Using Fractal Structures

Elham Behradfar and Edward J. Vigmond

Dept. Of Electrical & Computer Engineering, Schulich School of engineering, University of Calgary

Acknowledgements

CIHR, CRC, and the AHFMR Team Grant on OA.

Introduction

One part of the cardiac conduction system that has not been extensively modeled in detail, due to its intricate structure, is the Purkinje System (PS). The PS is a network located on the endocardial surface of the heart and is responsible for ensuring the synchronized timing and sequencing of ventricular contraction.

In this study, we used a fractal method to extend the Purkinje network that had been manually constructed by our research team[2,3]. This new detailed PS allows for accurate modeling of PS role in normal heart rhythm and arrhythmia.

Methods

A manually constructed PS model was based on schematics and pictures of the conduction system, textual descriptions of heart anatomy, and excitation mappings of the heart[2]. This part is shown by red lines in Fig. 1. To grow new branches of PS on the endocardial surface, endpoints of the manually constructed network were used as starting points. The growth process of new branches was based on fractal structures and generating rule suggested in [1]. The parallel rewriting system replaces each part of the current structure by applying the rule sequentially. Here, a branch which can grow in each iteration is called active branch while a branch which stops growing is called inactive. This growth simulation had one rewriting rule: in each step, every active branch was replaced with one inactive branch and two new active branches grew from the endpoint of that branch.

To generate uniform branch distributions on the surface, each branch consisted of five line segments. At the start point of each segment, the gradient of the distance field was calculated and

the growth direction of that segment was defined as the weighted sum of the gradient direction and the previous segment direction.

To generate a closed mesh structure like those seen in the PS, the system connected growing branches to the existing branches located a distance less than a threshold, k, and stopped growth.

Results

Figure 1 shows the generated network on endocardial surface. The directions and lengths of branches and weight of the gradient of distance field are determined by the user specified parameters. Adjusting the parameters is based on comparing the generated network with photographs of the PS and measured branch lengths in an actual PS. This method created a uniform distribution of branches since the new branch gradually curved to keep away from all existing branches. We stopped the growth iteration when there was no active branch and all active branches stepped out of the user specified endocardial region in the left and right ventricles. This method performed the growth simulation that constructed the 3D mesh structure of PS in a few minutes.

Conclusions

We generated a 3D model of the PS which closely resembles an actual PS. It has a more detailed structure compared to manually constructed models[2] and better reproduces PS activation patterns.

References

[1] J. Physiol. Sci. Vol. 58, 481–86, 2008.
[2] IEEE Trans. On Bio Med, Vol. 45, 389-99, 2007.
[3] Proc. of the IEEE Eng. in Med, 4235-8, 2005.

Adhesive Capabilities of Commercially Available Surgical Glues for the Repair of Defects in the Annulus Fibrosus

Terri L. Semler, Neil A. Duncan and Michael S. Kallos
McCaig Institute for Bone and Joint Health, University of Calgary

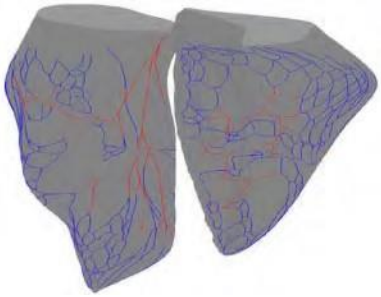

Figure 1: Generated Purkinje network laid out on endocardial surface

Introduction

The intervertebral disc (IVD) is a structure consisting of the outer annulus fibrosus and the inner nucleus pulposus. Degeneration of the disc is a significant problem with one in fifty Canadians being disabled by back pain in their lifetimes[1]. New techniques to repair the disc include injection of a replacement material for the nucleus pulposus, however without proper repair of the annulus, these treatments have minimal success[2].

Surgical adhesives are widely studied for soft tissue repair. Currently surgical adhesives are used commercially to achieve hemostasis or as adjuncts to sutures, primarily in cardiovascular surgeries. An adhesive that has the ability to seal small puncture holes left in the annulus after injection of therapeutics or replacement materials may enhance the success of such treatments[2]. In this study we compared the

adhesive strength of three commercially available surgical glues to bovine annulus tissue: Tisseel (Fibrin Sealant; Baxter International Inc.), BioGlue (Glutaraldehyde Sealant, Cryolife) and FloSeal (Collagen Sealant; Baxter International Inc.). Cyanoacrylate adhesives were not studied due to their high toxicity when applied internally[3].

Methods

To test the adhesive strength of the surgical glues, ASTM standard F225-05 was followed with slight modifications. Samples of bovine annulus were excised from fresh ox tails and two samples joined together with one of the three surgical glues using either a lap shear or butt joint configuration. The samples were loaded onto a tensile testing machine (Bose Electroforce 3200, Bose Centre, University of Calgary) and pulled at a constant crosshead speed of 10mm/min until failure. Whole annulus tissue was also tested in tension as a control.

Results

FloSeal was unable to form a bond with the annulus tissue and no adhesion was observed. Both Tisseel and BioGlue were able to adhere two pieces of annulus tissue together; however all of the BioGlue samples failed while bring loaded onto the machine. The Tisseel samples were tested, but significant force was not recorded at failure. The whole annulus tended to slip out of the grips prior to failing; one sample failed at the interface between the grips and the tissue at a stress of 1308 kPa.

Conclusions

Existing surgical adhesives do not provide sufficient adhesion to annulus tissue for applications in repairing the intervertebral disc. This study has shown that there is a significant need for the development of new adhesives that will provide sufficient adhesion to withstand the physiological strains present in the IVD. Novel combinations of synthetic and natural materials such as polymers, fibrin, collagen, elastin, and proteoglycans should be investigated to bond with proteins in cartilage in order to develop a regenerative solution for tissue repair in the IVD.

References

(1) Kandel et al. *Eur Spine J.* 2008 17(4): 480-491 (2) Schek et al. *Eur Cells Mater* 2011 21:373-383

(3) Taguchi et al. *Mat Sci Eng C* 2006 9-13.

Figures

3D Knee Joint Reconstruction from MR Images

H. Zheng, M. Kazemi, Y. Dabiri, L.P. Li*

Department of Mechanical and Manufacturing Engineering

University of Calgary, Alberta, Canada, T2N 1N4

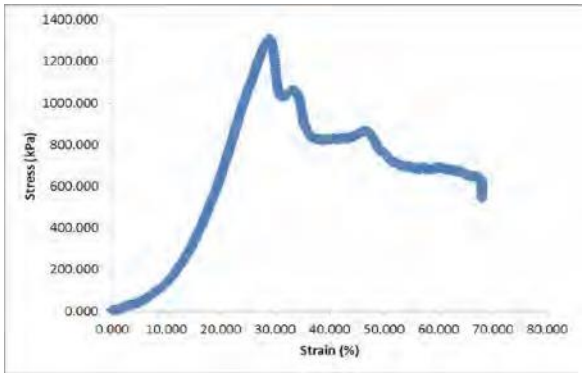

Figure 1: Stress Strain Curve for Bovine Annulus Fibrosus in Tension

Introduction

Osteoarthritis is one of the major diseases that cause disability. Previous studies implicate that the onset of osteoarthritis is associated with the changes in biomechanics of

articular cartilages in the joint. In recent years, computer models have been extensively used to study the biomechanics of the cartilaginous tissues. One of the first steps of such studies is to construct anatomically accurate models of the knee using available software packages. The objective of this study was to explore and compare the capability of two software packages, Rhinoceros 3D and Mimics, in the 3D reconstruction of the knee joint.

Methods

MRI data of the right knees were collected from two healthy volunteers (one 28-year female and one 27-year male) with the kind help from Dr. Richard Frayne at the Seaman Family MR Research Centre in Calgary. In Rhinoceros 3D, the original MRI data was first imported to Sante DICOM Viewer and then exported as JPEG format. The exported images then were imported by Rhinoceros 3D for segmentation. Mimics software has a built-in tool to read MRI data directly. A tool called 3D LiveWire was used for segmenting. Finally, 3D surface models were obtained using segments.

Results

Both Rhinoceros 3D and Mimics were successfully used for the reconstructions of distal femur. We experienced difficulties in reconstructing other cartilaginous surfaces with Rhinoceros 3D; we were only able to obtain femoral surface models (Figure 1). However, using Mimics, all tissue surfaces were successfully reconstructed. (Figure 2) A completed joint model included the following parts: femur, tibia, fibula, patella; all articular cartilages and menisci; and the four ligaments.

Conclusions

Rhinoceros 3D does not provide good tools in reconstructing complicated surfaces, but its open-programming feature allows it to integrate customized tools and scripts to help construct surfaces. Potentially, more powerful tools can be developed in Rhinoceros 3D. Nevertheless, Mimics has many tools for segmentation and 3D model calculating. It also includes options to modify and optimize the models. There are many other tools in Mimics that can be explored in the future, such as meshing based on bone density and exporting meshed models to ABAQUS for finite element analysis. In summary, the models reconstructed from Mimics are suitable for future finite element studies.

References

[1]. Brewer, Earl J. Angel, Kathy, *The Arthritis Sourcebook*, McGraw-Hill Trade, Blacklick, OH, USA, 04/2000, p.p. 18-19.

[2]. Taras Karpachevskyy, “Techniques and Software for Surface Reconstruction from MRI Data” (Department of Mechanical Engineering, University of Calgary, Calgary, Alberta, CANADA, Dec. 2010)

[3]. K. Hollerbach, A.M. Hollister, E. Ashby, “3-D Finite Element Model Development for Biomechanics: A Software Demonstration”, Lawrence Livermore National Laboratory, 7000 East Ave., Livermore, CA, March 1997

[4]. Tina Kapur, Paul A. Beardsley, Sarah F. Gibson, “Model Based Segmentation of Clinical Knee MRI”(Massachusetts Institute of Technology, Artificial Intelligence Laboratory, Cambridge, MA 02139, USA, Mitsubishi Electric Research Laboratory, Cambridge, MA 02139)

Figures

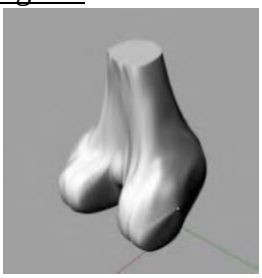

Figure 1

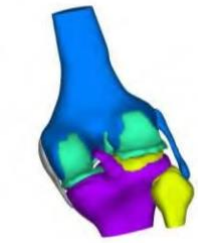

Figure 2

Fabrication and Characterization of 3D Alginate-HA Hydrogel Scaffolds for SCI Repair

M.D. Wang, N. Cao, C.L. Liu, D.J. Schreyer, X.B. Chen.
Division of Biomedical Engineering, University of Saskatchewan, 57 Campus Dr., Saskatoon, SK S7N 5A9, Canada

Introduction

Bioengineered scaffolds with highly interconnected pore networks have shown promise for spinal cord injury (SCI) repair. Alginate, a natural biomaterial, has been used successfully to fabricate scaffolds with reproducible microstructure using the rapid prototyping (RP) technique [1].
Unfortunately, the scaffolds showed limited interaction with mammalian cells due to the absence of receptors required for binding.

Here we report the incorporation of hyaluronic acid (HA), which has been shown to promote robust neurite outgrowth, into sodium alginate. The fabrication and characterization of three dimensional (3D) alginate-HA hydrogel scaffolds for SCI repair are also reported.

Methods

During dispensing, mixtures of 1.5% alginate with 0%, 0.375%, 0.5% and 0.75% of HA were extruded through a dispensing needle into calcium chloride ($CaCl_2$) crosslinking solution for gel formation. As the flow rate of the dispensed mixture is highly dependent on the flow behavior of the fluid, flow behavior of mixtures was examined. Models of the strut diameter and flow rate assuming fully developed laminar Newtonian flow were applied.

$CaCl_2$ concentration affects the crosslinking speed and density of alginate, and thus is important for attachment of scaffold layers to each other and the control of strand diameter. The concentration of $CaCl_2$ was varied from 10 mM to 150 mM for each mixture to examine its influence on the fabrication of scaffolds, which was characterized in terms of strut diameter and connectivity between layers. Axial compression test was also performed on cylindrical plugs of hydrogel to study mechanical properties.

Results

The result shows that 3D scaffolds can be fabricated from mixtures of 1.5% alginate with HA but not 1.5% alginate alone. The initial needle height from the surface of the $CaCl_2$ solution imposes significant effect on the formation of scaffolds as demonstrated in **Fig. 1**. A $CaCl_2$ concentration of 50 mM or 75 mM is preferable for 1.5% alginate/0.375% HA and 100 mM for 1.5% alginate/0.5% HA. Hydrogels crosslinked by 50 mM $CaCl_2$ for 24 hr demonstrate a viscoelastic compressive behavior similar to native spinal cord and have a tangent modulus of 70-80 Kpa (strain rate of 0.083 mm/s) with no significant difference between different hydrogels.

Conclusions

The result indicates the feasibility of fabricating 3D alginate-HA tissue scaffolds with controllable microstructure using the dispensing-based RP system. The influence of the flow behavior, $CaCl_2$ concentration and initial needle height for scaffold fabrication were characterized. Future work will examine the use of alginate/HA scaffolds in *in vitro* and *in vivo* tests for the SCI repair.

References

[1] S. Khalil, J. Nam and W. Sun, Multi-nozzle deposition for construction of 3D biopolymer tissue scaffolds, Rapid Prototyping Journal, 11/1 (2005).

Figures

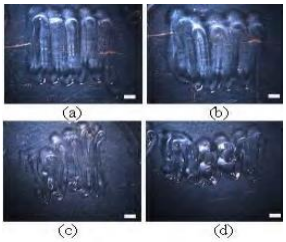

Fig. 1 Fabricated strand geometry using different initial needle heights: (a) 0.35mm, (b) 0.40mm, (c) 0.60mm, (d) 0.65mm.

Effect of Pelvic Orientation on Radiographic Measurements of Acetabular Inclination

Mohsen Akbari Shandiz and Dr. Carolyn Anglin
Biomedical Engineering, University of Calgary

Introduction

Incorrect inclination of the acetabular component in total hip arthroplasty can lead to dislocation, wear and loosening. We propose to create an adjustable mechanical device that can be preset to the correct orientation based on preoperative X-ray images. Since anteversion can be judged intraoperatively, we only need to preset the device for inclination. The desired inclination angle is achieved by setting an offset from the device-landmark angle (DLA), which is formed by reliable landmarks on the anteroposterior (AP) radiograph. However, accurate interpretation of plain pelvic radiographs is complicated by the wide variability in individual pelvic position relative to the X-ray plate [1]. In this study, we evaluated the effect of pelvic tilt and rotation on the DLA and developed a formula using regression analysis to estimate pelvic tilt.

Methods

AP pelvic radiographs were digitally created from a pelvis CT scan using ZIBAmira image analysis software at different pelvic orientations. The pelvis was tilted around two axes (interacetabular axis and longitudinal axis) with 3º increments. The tilt range was -6º to 21º whereas the rotation range was ±9º, based on the variability of pelvic orientation in the literature [2]. We thus obtained a total of 17 digitally reconstructed radiographs (DRR) for the study. DLA was measured using the angle between a line passing from the superolateral edge of the acetabulum to the teardrop of the acetabulum and a line connecting the bottom of the ischial tuberosities. Correlations of pelvic tilt and rotation with DL angle were analyzed using regression analysis. To estimate pelvic tilt from AP radiographs, we used the ratio between the vertical diameter of the pelvic foramen (A) and the average of the vertical diameters of the right and left obturator foramens (B) (Figure 1). Using regression analysis, we developed an equation that defines the correlation of the pelvic tilt with the A/B ratio.

Results

Across the range of pelvic tilts, DLA varied from 31.0º to 34.5º. Across the range of pelvic rotations, DLA only varied from 32.0º to 32.7º. The correlation coefficient of DLA vs. pelvic tilt (PT), using a quadratic regression, was 0.98 ($DLA = -0.0028PT^2 + 0.1853PT + 31.958$); for pelvic tilt vs. the A/B ratio (AB), it was 0.99 ($PT = 0.6634AB^2 + 10.277AB - 19.48$).

Conclusions

We made DRRs from a CT image in different orientations to measure the effect of pelvic tilt and rotation on the DL angle. Our results demonstrate that the pelvic tilt has a significant effect on the DLA measurements on radiographs, but that pelvic rotation has a negligible effect. Additional CT scans need to be analyzed to determine overall regression equations. When used together with our device, we expect this to improve acetabular component alignment during surgery.

References

[1] Anda S. et al. *Acta Radiologica*, vol. 31, no. 4, pp.

389-394, 1990. [2] Tannast M et al. *Clin Orthop Relat Res*, no. 436, pp. 144-150, 2005.

Figures

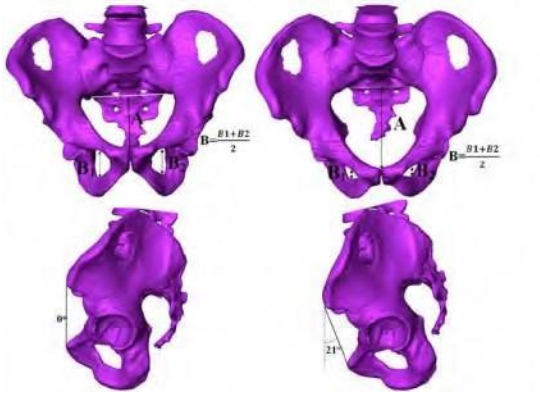

Fig.1. Pelvic tilt: **Left)** Neutral position, **Right)** 21º tilt

dye; the fluorescence signal was recorded with a high speed camera and the data processed offline [4] using the Matlab environment.

Feature points or regions were selected based on the SIFT scale and rotation invariant operator [5]. The detected regions allow the cross correlation algorithm to work in specific sections of the image finding a description for the gross motion artifact for every region. Having the motion information for each region, as a displacement in *x* and *y* coordinates, a transformation function can be calculated in order to align the images and remove the effect of motion artifact.

The gross motion in the set of images is compounded by translation in both axes, rotation, scaling and shearing; in the first stage of this study the detection of motion is restricted to small areas were all motion can be approximated as small translations in the *x* and *y* directions.

Removal of Motion Artifact in Cardiac Optical Mapping for Complete Heart Preparations

Marcela Rodriguez[1], Anders Nygren[1,2]

[2]

Dept. of Electrical & Computer Engineering and Centre for Bioengineering Research & Education

Schulich School of Engineering, University of Calgary

Introduction

Cardiac Optical Mapping has been widely utilized in cardiac tissue and whole hearth preparations to perform electrophysiological studies. The procedure uses voltage sensitive dyes which produce a signal proportional to membrane voltage [1]. The natural cardiac motion due to contractions affects the recording producing motion artifacts that affect the electrophysiological signal that is being measured [2].

Common approaches to reduce gross motion artifacts in fluoresce images involve mechanical restraint of the preparation, the use of chemical inhibitors, ratiometry acquisition and image processing [3]. The chemical motion blockers also affect the physiological response of the biological parameter of interest.

The purpose of this study is to present a preliminary study for the detection of features and gross motion artifact and the application of image registration methods for its removal.

Methods

The study was done in complete rat heart preparations mounted in a Langendorff system. Di-4- ANNEPPS was used as the voltage sensitive

Results

The SIFT algorithm [5] was implemented with an initial sigma of 0.6, this parameter specifies level of smoothness applied to the images, the selection was due to the low contrast nature of the original images. Four octaves were created and the local extrema detection was obtained from the Difference of Gaussian of the images in different scales. The extrema detected were taken as key points to implement the cross correlation algorithm. Specifically, a region was created surrounding each keypoint found by the SIFT algorithm. In order to generate the regions to be tracked a surrounding region dependence method was used, were a measure of contrast was used to grow the region around the keypoints. Any key points that were found outside the heart contour were ignored.

To date, we have only used the cross correlation algorithm to track the motion and to perform image registration. Other algorithms will have to be applied and compared in order to obtain the lowest error measure between the image registered and the original image.

Conclusions

The detection of features was possible with the proposed methods and the tracking of the regions detected was performed. The transformation was calculated to register the images and a measure of Mean Square Error was obtained. Future work will yield the data required to compare algorithms and to reduce the error measure for the registered images.

References

[1] Biol. Res Nurs, Vol. 11 N.2, 195:207, 2009 [2] IEEE EMBS, 3240:3243, 2009.
[3] IEEE T Bio-Med Eng.,Vol. 52, N.2,338:341,2005
[4] Am J Physiol Heart C, 296: H1442–H1450, 2009
[5] Int. J Comput. Vision, Vol. 60 Issue 2,2004

Midsole Hardness, Gender & Age Effects on Lower Extremity Kinematics During Running

Jennifer Baltich[1], Christian Maurer[1], Peter Federolf[1,2], Benno M. Nigg[1] [1]
Human Performance Laboratory, University of Calgary, 2500 University Dr. NW, Calgary, AB, Canada, T2N 1N4
[2] Norwegian School of Sport Sciences, P.O Box 4014 Ulleval Stadion, 0806 Oslo, Norway

Introduction

Despite the evolution of the running shoe in the last decades, there is still no factual basis for the appropriate cushioning to be used for individual running shoe design. Certain groups of individuals may have different needs from a shoe based on their movement patterns and, therefore, may benefit from a customizable shoe design. Such groups might be found in gender or age among others. This study investigated the influence of three different midsole hardness conditions as well as gender and age on the lower extremity kinematics during heel-toe running.

Methods

The lower-extremity kinematic gait variables for 93 runners (male and female) aged 16-75 were combined and analyzed with one functional data interpretation method. Kinematic data was collected using 12 retro-reflective markers skin-mounted on the pelvis and right lower extremity. Participants performed heel-toe running trials at 12 ±0.6 km/h on a 30 m-long runway with soft, medium and hard midsoles. Functional data interpretation was performed with a principal component analysis approach (Ramsay 2005). Group classification of the movement was performed with a support vector machine and a leave-one-out method was used to calculate significance.

Results

A significant classification rate of 99.25% (SD 2.65) was found between the hard and the soft midsole while a significant classification rate of 95.38% (SD 9.39) was found between the hard and the medium midsole and a significant classification rate of 85.95% (SD 16.06) was found between the soft and the medium midsole (Figure 1, only hard and soft condition shown). The principal component vectors showing the greatest effect of the shoes indicated greater ankle and knee movement in the sagital plane with the soft midsole compared to the hard midsole. A classification rate of 86.58% (SD 27.21) was found between the male and female subjects, with indications of greater hip internal rotation for the female subjects. A classification rate of 86.58% (SD 27.22) was found between the youngest group (16-20 years) and the oldest group (61-75 years) with indications of greater knee flexion for the younger individuals.

Conclusions

The combined analysis of lower leg kinematics during running allowed for a discrimination of the movements between midsole hardness, gender, and age. Since gender and age demonstrate a classifiable effect on the biomechanics of an individual, it is possible that shoe design should be customized to the user. Therefore, the development of guidelines for the construction of running shoes that are adapted to different user profiles is warranted.

References

[1] Ramsay, J.O., Silverman B.W. (2005). Functional Data Analysis. Springer Science, New York.

Figures

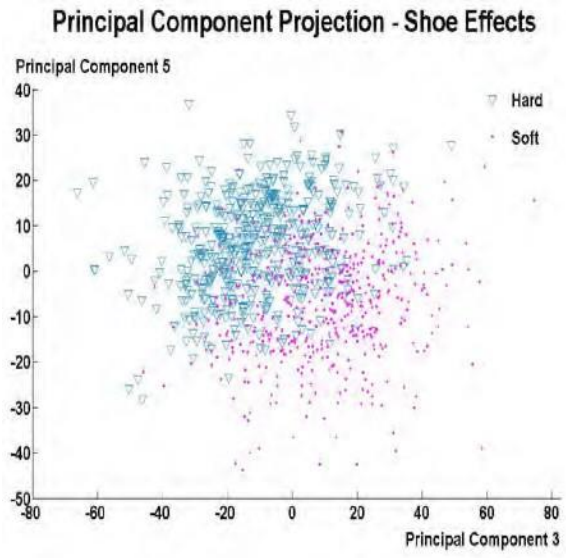

Strain Rate Dependence of Bovine Medial Menisci in Circumferential Tension

Stephen Andrews, Dr. Janet Ronsky
Schulich School of Engineering, University of Calgary, Calgary, AB, Canada

Introduction

A complete understanding of the material properties of the menisci of the knee is integral for the development of accurate computer models, bioengineered materials or synthetic materials appropriate for grafting in orthopaedic procedures. While the material properties of the menisci have been evaluated, most studies are completed at very slow, non-physiological strain rates [1, 2]. Therefore, the goal of this study was to determine strain rate-dependence of bovine medial menisci in tension and develop and mathematical technique to analyze said data.

Methods

Tensile testing was conducted on bovine medial meniscal samples (n=9). Specimens were obtained from the outer edge of the menisci using a series of custom designed cutting jigs. The specimen were dimensions were approximately (10 mm x 5 mm x 2 mm, length x width x thickness). Testing was completed using a Bose Electroforce 3200 apparatus (Bose Corp., Eden Prairie, USA). The specimens' dimensions were first measured using a photogrammetric technique developed with custom Matlab code. Specimens were mounted and a tare load of 0.03 N was applied, then preconditioned (3% strain, 15 cycles @ 1 Hz) and allowed to recover for 120 s. The samples were then tested at four different extension rates (0.005, 0.05, 0.5 and 5 mm/s) to approximately 8% strain, and the resulting force-displacement curves were recorded with 120 s recoveries between each test. Grip-to-grip displacement and the cross-sectional area were used to convert the force-displacement to stress-strain. This data was then fit to a sigmoidal function using Matlab curve fitting function. To calculate the tangent modulus, the analytical function describing the stressstrain curve was then differentiated to obtain the function describing the tangent modulus. T-tests ($\alpha = 0.05$) were used to compare the normalized increase in stiffness (normalized to the lower strain rate). A Bonferroni correction was applied to account for multiple comparisons.

Results

There was a substantial and significant increase in the tangent modulus with increasing strain rate. Modulus at 7% strain was 37% greater at 0.5 mm/s and 20%

Figures

Spectral Clustering of Resting State fMRI Using a Group Similarity Matrix

Alireza Sojoudi[1,2], Seyed Mohammad Shams[1], Bradley Goodyear[2], Martin Walter[3], Gholam-Ali Hossein-Zadeh[1]
[1] Control & Intelligent Centre of Excellence, University of Tehran, Tehran, Iran; [2] Dept of Biomedical Engineering, University of Calgary, Calgary, AB, Canada; [3]Dept of Psychiatry, University of Magdeburg, Magdeburg, Germany

stiffer at 0.05 mm/s than at 0.005 mm/s ($p < 0.001$ and $p < 0.001$, respectively). Modulus was also greater for 0.5 mm/s strain rate compared to 0.05 mm/s ($p < 0.001$). The sigmoidal fit of the stress-strain data was excellent (figure 1), with average R^2 = 0.9999, [0.9994 – 1.000]. The tangent modulus obtained from analytical differentiation (figure 2) was compared to the numerical derivative of the filtered stress-strain curve, and the values were in good agreement.

Conclusions

Bovine medial menisci were sensitive to strain rate in circumferential tension with a 37% increase in modulus from the slowest to fastest strain rate. The sigmoid fit proved to be an excellent approximation of the experimental data.

References

1.Fithian, D.C., M.A. Kelly, and V.C. Mow, *Material properties and structure-function relationships in the menisci.* Clin Orthop Relat Res, 1990(252): p. 19-31.

2.Tissakht, M. and A.M. Ahmed, *Tensile stress-strain characteristics of the human meniscal material.* J Biomech, 1995. **28**(4): p. 411-22.

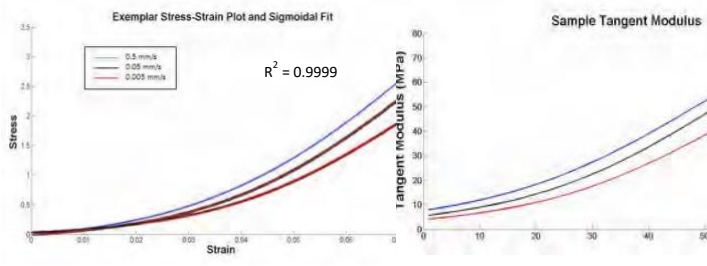

Figure 1. Exemplar stress-strain plot with sigmoid fit.

Figure 2. Sample tangent modulus plot for increasing strain rate

Introduction

The coherence of spontaneous slow fluctuations (0.01 to 0.1 Hz) of Blood Oxygenation Level Dependent (BOLD) fMRI signal between different brain regions is an indicator of a functional connection [1]. The degree of coherence is called functional connectivity, and the identified brain regions form Resting Sate Networks (RSNs). There are two major approaches to the analysis of the resting state: model based and data driven. However, examining RSNs across a group of subjects is still a complex task, and often requires operator input to select networks that are the most meaningful. In this study, we introduce a new group spectral clustering algorithm, which constructs a similarity matrix based on the time series of all subjects. The obtained clusters represent objectively determined functional networks that are consistently present across subjects.

Methods

The similarity matrix is constructed by calculating the projected energy of one region's timecourse onto a basis matrix constructed from the time courses of another region. This similarity matrix is grouped by eigen-decomposition. The similarity of regions A and B is calculated as follows:

Let x_i (i=1,2,...,M) represent the timecourses from region A for M subjects. If $Y=[y_1|y_2|...|y_M]$ is

a basis matrix consisting of the timecourses from region B for all M subjects, then the projection of x_i onto Y is accomplished using $P_Y = Y\,Y\,Y(\,^T)^{-1}Y^T$, i.e.,

$P_Y\,x_i$, and the amount of projected energy of x_i in this space is $E_i = x_i^T\,P_Y\,x_i$. The similarity coefficient of the two regions is calculated as the mean projected energy of all subjects' time courses onto the basis matrix. The similarity matrix is then subjected to a spectral clustering algorithm [2] to identify brain regions constituting RSNs.

Results

Figure 1 shows the RSNs identified using our algorithm. These networks are consistent with those identified in previous studies [3], such as the default mode network (DMN), which includes ventromedial prefrontal cortex as well as posterior cingulate and parietal regions.

Conclusions

We have proposed a method to identify RSNs in the human brain. Our method is more robust and specific compared to a previously proposed algorithm, which performs normalized cut clustering on the similarity matrix constructed for each subject [4]. Our method is also less sensitive to outliers.

References

[1] M. Fox et al, "Spontaneous fluctuations in brain activity observed with functional magnetic resonance imaging," *Nature*, vol. 8, pp. 700–711, 2007. [2] U. von Luxburg, "A tutorial on spectral clustering," Tech. Rep. TR-149, Max Planck Institute for Biological Cybernetics, 2006.

[3] M. DeLuca et al, "fMRI resting state networks define distinct modes of long-distance interactions in the human brain," Neuroimage, vol. 29, pp. 13591367, 2006.

[4] M.Heuvel et al., "Normalized cut group clustering of resting-state fmri data," *PloS One*, vol. 3(4), 2008.

Figures

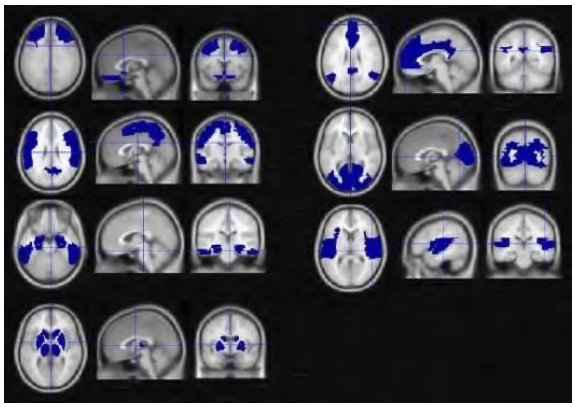

Figure 1: Brain networks identified using our proposed algotihm.

A 3-D HYDROGEL CELL SCAFFOLD FOR ASSESSING THE BIOCOMPATIBILITY OF INTRASPINAL MICROSTIMULATION ELECTRODES

Alexandra Chow[1,4], Kamaldeep S. Dhami[2], Kathryn G. Todd[2,3,4], Anastasia Elias[1,4] Faculty of Engineering[1], Faculty of Medicine & Dentistry, Department of Psychiatry[2] & Center of Neuroscience[3], University of Alberta, Edmonton, AB, Canada. AIHS Interdisciplinary Team in Smart Neural Prostheses[4]

Introduction

Intraspinal microstimulation (ISMS) is a method of functional electrical stimulation for restoring lower limb function after spinal cord injury. The technique takes advantage of the fact that neural networks below the site of lesion are often still intact after injury and can be electrically stimulated using an external source. ISMS involves the longterm implantation of microwire electrodes directly into the spine to target motor pools that control the movement of legs.

Previous studies to evaluate the response of a rat spinal cord to electrode implantation and chronic ISMS revealed a persistent inflammatory response

and reactive gliosis around the devices after 30 days [1]. Performing such experiments in living animals is costly and time intensive.

As such, a biological surrogate model of spinal cord tissue is desirable to provide a high-throughput means of testing the biocompatibility of new electrode designs. A three-dimensional cell scaffold capable of *in vitro* culture would be able to capture the biological, spatial, and mechanical interactions of the spinal cord with an ISMS electrode inserted long-term.

Results

Hyaluronic acid (HA), the candidate scaffold material chosen, is prevalent in connective and neural tissues. HA sodium salt was modified with photocrosslinkable methacrylate functional groups with a degree of modification of 75 to 100% as determined using ^{1}H-NMR spectroscopy. An optimum 3-component visible light photoinitiating system was developed which was tested to be biocompatible with the growth of mixed glia from rats in monolayer culture. The system was photoactivated by exposure to a high-intensity green LED (300 mW/cm^2 flux at a 30 s duration) and employed the following photoiniators and corresponding concentrations: 0.01 mM eosin Y, 0.1% (w/v) triethanolamine, and 0.1% (w/v) 1-vinyl-2-pyrrolidinone. Clear, solid, soft, flexible HA hydrogels were formed consistently in various geometries. Mixed glia from rats was suspended at < 10^5 cells/mL in a precursor solution containing 0.5% (w/v) modified HA and the tested optimum photoinitiating system. Cells were encapsulated throughout the HA hydrogel as individual cells or aggregated clusters after photopolymerization. The cell morphology and distribution observed within the hydrogel closely resembled that of mixed glia cultured in the monolayer control. Hydrogels containing photoencapsulated mixed glia saw a marked increase in cell density within 7 days of culture.

Conclusions

A 3-D cell scaffold for the long-term *in vitro* culture of mixed glia from rats was successfully developed that met the requirements of production efficiency and biocompatibility. Photoencapsulated cells remained viable and proliferative, showing HA hydrogels to be a promising biological surrogate model of spinal cord tissue.

References

[1] Bamford JA, Todd KG, Mushahwar VK. The effects of intraspinal microstimulation on spinal cord tissue in the rat. Biomaterials 2010;31:5552–5563.

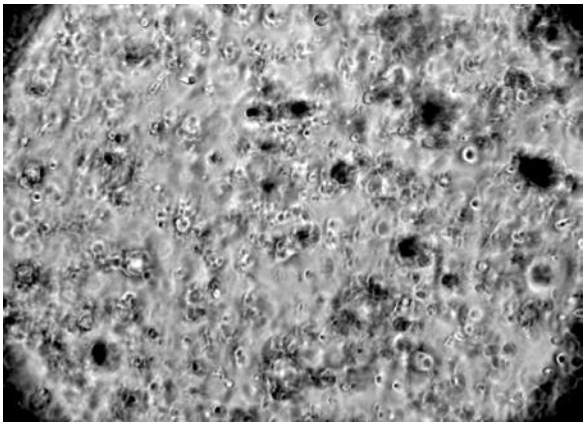

Figure: Mixed glia photoencapsulated within HA hydrogel after 7 days of culture

Notes

Notes

Notes: